University of Illinois at Urbana-Champaign

ACRC

Air Conditioning and Refrigeration Center A National Science Foundation/University Cooperative Research Center

Exploratory Research on MEMS Technology for Air Conditioning and Heat Pumps

T. M. Leicht, P. S. Hrnjak, and M. A. Shannon

ACRC CR-44 January 2002

For additional information:

Air Conditioning and Refrigeration Center
University of Illinois
Mechanical & Industrial Engineering Dept.
1206 West Green Street
Urbana, IL 61801

(217) 333-3115

The Air Conditioning and Refrigeration Center was founded in 1988 with a grant from the estate of Richard W. Kritzer, the founder of Peerless of America Inc. A State of Illinois Technology Challenge Grant helped build the laboratory facilities. The ACRC receives continuing support from the Richard W. Kritzer Endowment and the National Science Foundation. The following organizations have also become sponsors of the Center.

Alcan Aluminum Corporation
Amana Refrigeration, Inc.
Arçelik A. S.
Brazeway, Inc.
Carrier Corporation
Copeland Corporation
Dacor
Daikin Industries, Ltd.
Delphi Harrison Thermal Systems
General Motors Corporation
Hill PHOENIX
Honeywell, Inc.
Hydro Aluminum Adrian, Inc.
Ingersoll-Rand Company
Kelon Electrical Holdings Co., Ltd.
Lennox International, Inc.
LG Electronics, Inc.
Modine Manufacturing Co.
Parker Hannifin Corporation
Peerless of America, Inc.
Samsung Electronics Co., Ltd.
Tecumseh Products Company
The Trane Company
Valeo, Inc.
Visteon Automotive Systems
Wolverine Tube, Inc.
York International, Inc.

For additional information:

Air Conditioning & Refrigeration Center
Mechanical & Industrial Engineering Dept.
University of Illinois
1206 West Green Street
Urbana, IL 61801

217 333 3115

Abstract

This report presents an experimental investigation of refrigerant liquid mass fraction (LMF) in the exit flows of plate evaporators. The objective is to identify a sensor that is capable of measuring small amounts of refrigerant liquid in the superheated vapor at evaporator exits. This sensor should have the potential to be combined with an active control scheme that increases the fill factor of the evaporator while simultaneously reducing superheat temperature at the evaporator exit. Four methods were used to detect refrigerant droplets in the superheated vapor stream exiting a plate evaporator: (1) an energy balance calculation, (2) a microfabricated thin-film resistance sensor developed specifically for this project, (3) an exposed beaded thermocouple, and (4) photodiodes that detected laser light scattered by droplets. The design, fabrication, calibration procedures, and theory of operation of the MEMS thin-film resistance sensor are also presented in this report. Experimental results indicate that a MEMS thin-film resistance sensor is more sensitive than a beaded thermocouple to LMF of non-equilibrium evaporator exit flows. The MEMS sensor accurately detected refrigerant LMF as low as 1.5% in superheated evaporator exit flows.

Table of Contents

List of Figures

Page

List of Tables

Page

Nomenclature

Roman Symbols:

a	maximum serpentine resistor size
A_{cs}	cross-sectional area
A_s	surface area of MEMS sensor
C_o	MEMS sensor calibration constant
g	gap between serpentines in MEMS sensor
i_s	MEMS sensor current
l	active length of serpentine resistor
m_1	initial slope of $V_1(i_s)$
m_2	initial slope of $V_2(i_s)$
n	number of serpentines in MEMS sensor
LMF	liquid mass fraction
$\dot{q}''$	MEMS sensor surface heat flux
R_{design}	design resistance of MEMS sensor
R_o	reference resistance at temperature $T_o = 0°C$
R_s	resistance of MEMS sensor
t	thickness of serpentine in MEMS sensor
T	Temperature
$T_{in\text{-}situ}$	sensor temperature using in-situ calibration technique
T_o	reference temperature
T_s	MEMS sensor temperature
$T_{s,1}$	MEMS sensor temperature, large
$T_{s,2}$	MEMS sensor temperature, medium
$T_{s,3}$	MEMS sensor temperature, small
$T_{e,out}$	refrigerant temperature at main evaporator outlet
T_{mix}	temperature at the static mixer outlet
T_{sat}	saturation temperature
T_{TC}	temperature measured by thermocouple in the glass tube
$T_{4\text{-}wire}$	sensor temperature using 4-wire calibration technique
$T_{\infty,1}$	vapor temperature during sensor calibration
$T_{\infty,2}$	vapor temperature during sensor calibration
ΔT_{sup}	superheat temperature
V_s	voltage drop across MEMS sensor
V_1	sensor voltage at $T_{\infty,1}$
V_2	sensor voltage at $T_{\infty,2}$
w	width of serpentine in MEMS sensor

Greek Symbols:

α	temperature coefficient of resistivity $\{°C^{-1}\}$
χ	resistivity $\{\mu\Omega\text{-cm}\}$

Chapter 1: Introduction

Large heat pumps, refrigeration, and air conditioning systems often use plate heat exchangers (PHE) as evaporators. Plate evaporators consist of multiple refrigerant channels, or plates, in which the refrigerant evaporates vertically up each channel. Typically, the channels are connected in parallel, but they can also be circuited in a serpentine fashion to achieve a desired performance level. In direct expansion (DX) systems, refrigerant is expanded through a single throttling device such as a thermostatic expansion valve (TXV). TXV's operate by limiting the refrigerant flow so that the superheat temperature at the exit is high enough to ensure stable operation. In horizontal tube evaporators, a superheat temperature of 5°C is usually enough for stability over a large range of evaporator loads, but plate evaporators typically require superheats above 8°C for stable operation. A high superheat degrades evaporator performance because it results in a large superheated zone in the evaporator where heat transfer coefficients are lower than in the two-phase evaporating zone. Ideally, the evaporator should run with zero superheat, for all evaporator loads, to maximize the two-phase heat transfer area of the evaporator. This is impossible with DX systems using plate evaporators because distribution of the two-phase refrigerant is complicated, and current distribution schemes using orifice tubes are unreliable. Multi-channel evaporators also suffer from refrigerant side maldistribution caused by uneven loads within the evaporator. Flow maldistribution can result in one or several channels being completely filled with two-phase refrigerant, while neighboring channels are dry at the exit. Therefore, in plate evaporators, a high superheat is maintained to assure dry exit conditions and to prevent large quantities of liquid from carrying over and damaging the compressor.

Since high exit superheat temperatures degrade evaporator performance and capacity, any refrigerant flow control scheme that reduces the superheat required for stable operation will improve evaporator performance. A good control strategy would include sensors that can detect a small liquid fraction in a superheated vapor stream, and can be easily incorporated into a feedback loop with the throttling device. A further improvement to DX systems using plate evaporators would be to incorporate these sensors with a multi-valve, active feedback flow control strategy where refrigerant expansion can be independently controlled. Such a strategy could be realized by using MEMS (microelectromechanical systems) flow control valves as the throttling device for each channel. MEMS is an enabling technology that merges the capability to sense, actuate, and control the macro environment with micro-scale systems. The technology has emerged from the fabrication processes of semiconductor devices, and it is finding applications in the areas of 1) fluid sensing; 2) mass data storage; 3) optics and imaging; 4) miniature analytical instruments; 5) biomedical sensors and many other areas. MEMS has the potential to provide a small size, low power consumption, low mass, low cost, and highly functional solution to the problem of refrigerant flow distribution within multi-channel evaporators. Of course, the same feedback control strategies could be accomplished with normal scale valves, and the attendant sensors, circuitry, and controllers. These systems would prove too bulky, expensive, and complex for controlling individual evaporator channels, and thus would not be adopted by industry.

The purpose of this investigation was to measure the time-varying signals of several sensors at the exit of a plate evaporator as superheat is decreased, and correlate those signals with a time-averaged liquid mass fraction (LMF) in the superheated vapor stream. By investigating the sensor signals, it was possible to understand the nature

of the non-equilibrium two-phase flow exiting the plate evaporator. The time-averaged LMF of the evaporator exit flow stream was measured by using a passive flow mixer to agitate the two-phase refrigerant mixture and evaporate any entrained liquid droplets with heat supplied by the surrounding vapor. An energy balance of the inlet and outlet flows through the mixer provides the time-averaged LMF.

The exit flows of three evaporator configurations were measured with a newly developed MEMS thin-film resistance sensor, with a laser and photodiodes for measuring light scattered by entrained droplets, and with an exposed beaded thermocouple. The evaporator configurations include 1) a plate evaporator fed by a thermostatic expansion valve, 2) a plate evaporator fed by a manual valve, and 3) a two-evaporator configuration used to simulate maldistribution between parallel channels. The MEMS sensor, scattered laser light, and thermocouple signals were recorded at both slow and fast rates in order to characterize the unsteady flow exiting the evaporator. Results are presented in the time and frequency domain, and indicate that as superheat is reduced, entrained droplet mists emerge in regular intervals at the evaporator exit.

Three MEMS thin-film resistance sensors were designed, fabricated, and calibrated against known liquid mass fractions for the purposes of this investigation. This report documents the general theory of operation of the heated sensors, the methodology for designing thin-film serpentine resistors with minimum surface area, the fabrication of the sensors on a thin silicon wafer, and the calibration of the sensors. The three MEMS sensors varied in size, but all had the same surface heat flux. They were driven with a small constant DC current to provide self-heating in order to boil liquid droplets that would impact the sensor. A comparison of the three sensor signals in the frequency domain reveals that the sensor size does not influence its ability to detect a small liquid mass fraction in a superheated vapor stream.

The performance of the MEMS sensor and the beaded thermocouple when exposed to small liquid mass fractions in a superheated vapor stream were compared. This was done to assess the feasibility of using each instrument to control refrigerant flow to the evaporator by detecting and controlling LMF instead of controlling superheat, as is the case of thermostatic expansion valves. A unique comparison of the DC and AC signals as a function of LMF and superheat is presented for both instruments. Results show that the MEMS sensor is more sensitive to LMF than the thermocouple. Both instruments exhibit a saturation point beyond which they can no longer detect increases in LMF.

Chapter 2: Experimental Facility

2.1. Parallel plate evaporator test facility

A new refrigeration system was built for the purposes of this study in the Laboratory for Plate Heat Exchangers at the University of Illinois in Urbana-Champaign. A photo of the test rig appears in Figure 2-1. It was designed to simulate operating conditions typical of water chillers of less than 60 tons (210 kW) capacity using plate heat exchangers for evaporation. The facility consists of three main parts: 1) the refrigerant loop, 2) the water loop, 3) and the evaporator exit test section. All of which will be discussed in this section. Later, in section 3.2 the facility instrumentation is discussed. The data acquisition system is described in section 3.3.

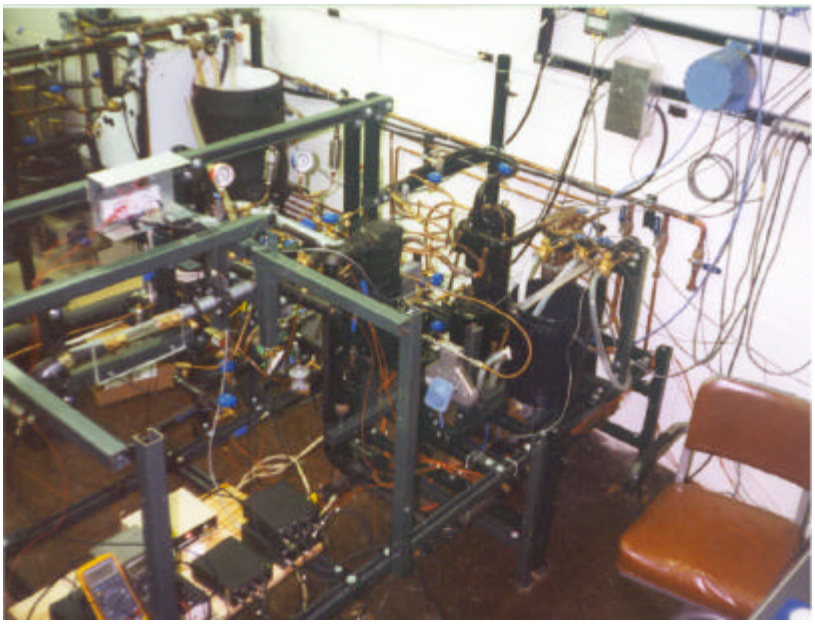

Figure 2-1. Photo of experimental facility

2.1.1 Refrigeration flow loop

The refrigeration loop contained the four necessary elements of a vapor-compression cycle refrigeration system: compressor, condenser, expansion device, and evaporator. In addition, there was a receiving tank for collecting high pressure liquid from the condenser, a liquid subcooler, and instrumentation for monitoring process conditions. The system schematic is shown in Figure 2-2, where solid lines represent refrigerant piping, and dashed lines represent water piping. The compressor was a Copeland model ZR61K2 hermetically sealed scroll compressor. The refrigerant was R22. Mineral oil circulated through the entire flow loop, including the test section, and was necessary to lubricate the compressor. A common problem in these types of systems is oil accumulation in the evaporator when operating at high superheats. This reduces evaporator capacity, and could influence refrigerant side maldistribution.

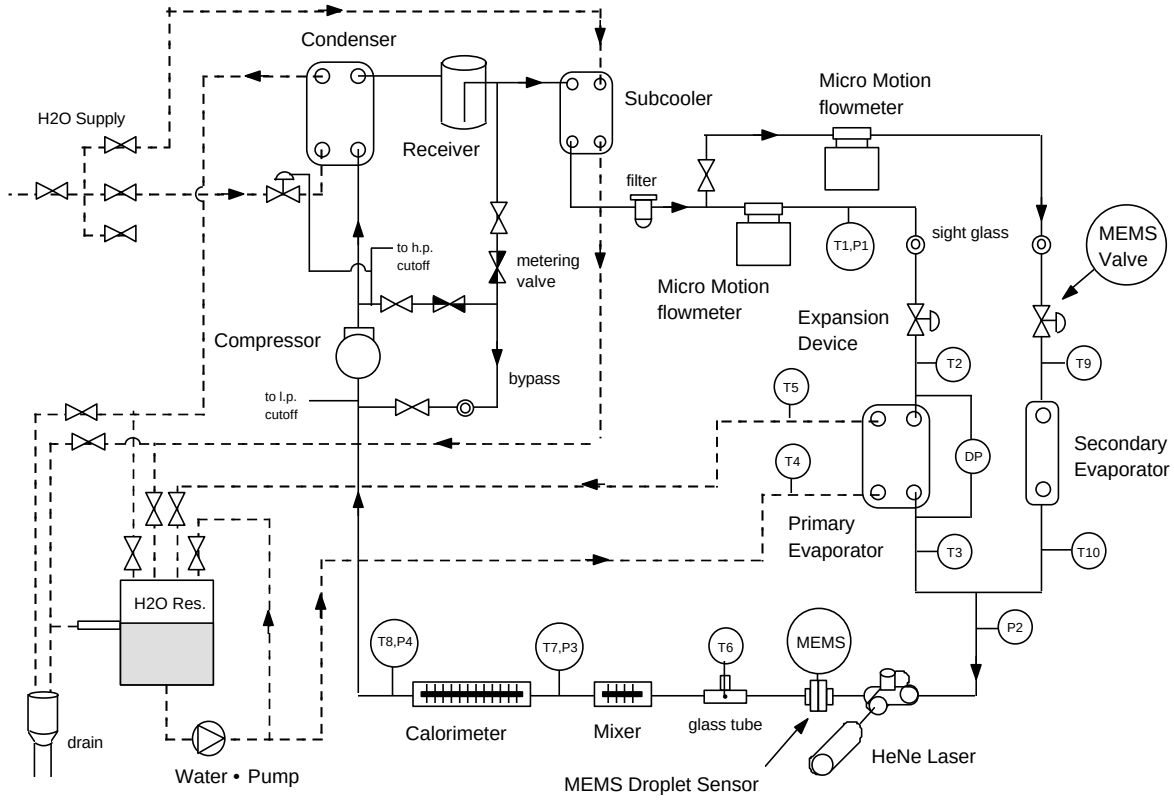

Figure 2-2. Flow schematic of experimental facility showing refrigerant lines (solid) and water lines (dashed)

Immediately on the discharge side of the compressor was a SWEP model B15×60 parallel plate condenser. Condensers like this one are often used in unitary A/C systems. Building cold water supply was used as the cold fluid in the condenser, which operated in a counter flow arrangement. A manually set water flow control valve adjusted condensing pressure. A receiver was installed downstream of the condenser to collect the high pressure liquid before entering the liquid subcooler. The subcooler was also a SWEP design plate heat exchanger model B8×20. A flexible, albeit complicated, water flow loop allowed for a wide range of achievable subcooled temperatures. The water flow loop is discussed in more detail in section 3.1.2. Typically, building cold water supply was circulated through the subcooler to provide a subcooled refrigerant temperature of 16°C before the expansion device. Circulating cold water from the evaporator through the subcooler could attain colder subcooled temperatures.

Subcooled refrigerant then divided into two branches, the main evaporator and the secondary evaporator. This combination of the main and secondary evaporators constituted a parallel-pass evaporator in which maldistribution could be induced by the user. Manual expansion valves fed both evaporators. Manual control allowed the flow through each expansion valve to be precisely controlled such that the main evaporator operated with high exit superheat, while the exit of the secondary evaporator was in the quality region. The exit streams reunited prior to the test section such that the combined flows, superheated vapor from the main evaporator and high quality refrigerant from the secondary evaporator, closely simulated the unsteady exit conditions of a plate

evaporator. The unsteady exit conditions of a TXV-controlled plate evaporator were first explored in a series of tests using only the main evaporator.

The main evaporator, shown in Figure 2-3, was fed by an ALCO series TCL thermostatic expansion valve that was modified for manual operation. The temperature sensing bulb and diaphragm assembly were replaced with a micrometer handle attached directly to the valve stem cage assembly. The micrometer handle allowed for precise control of evaporator feeding, and eliminated hunting problems associated with conventional TXV's that add an additional layer of complexity to multi-pass evaporator systems. Operating at a fixed expansion valve position also permitted the investigation of evaporator dynamics, independent of TXV dynamics, over a wide range of superheat. The main evaporator was a SWEP model B15×40 3-ton (10.5 kW) capacity parallel plate heat exchanger. It consisted of 19 refrigerant passages and 20 water passages operating in a counter-flow configuration. The plates had chevron style contours to enhance heat transfer. Two-phase refrigerant entered at the bottom of the evaporator, evaporated vertically through the plates, and exited as superheated vapor at the top of the evaporator. The heat load to the evaporator was supplied by water from the water reservoir. Thermocouples located immediately at the entrance and exit of the refrigerant and water streams monitored process conditions. Care was taken to position the exposed bead of the refrigerant exit thermocouple at the center of the exit pipe cross section.

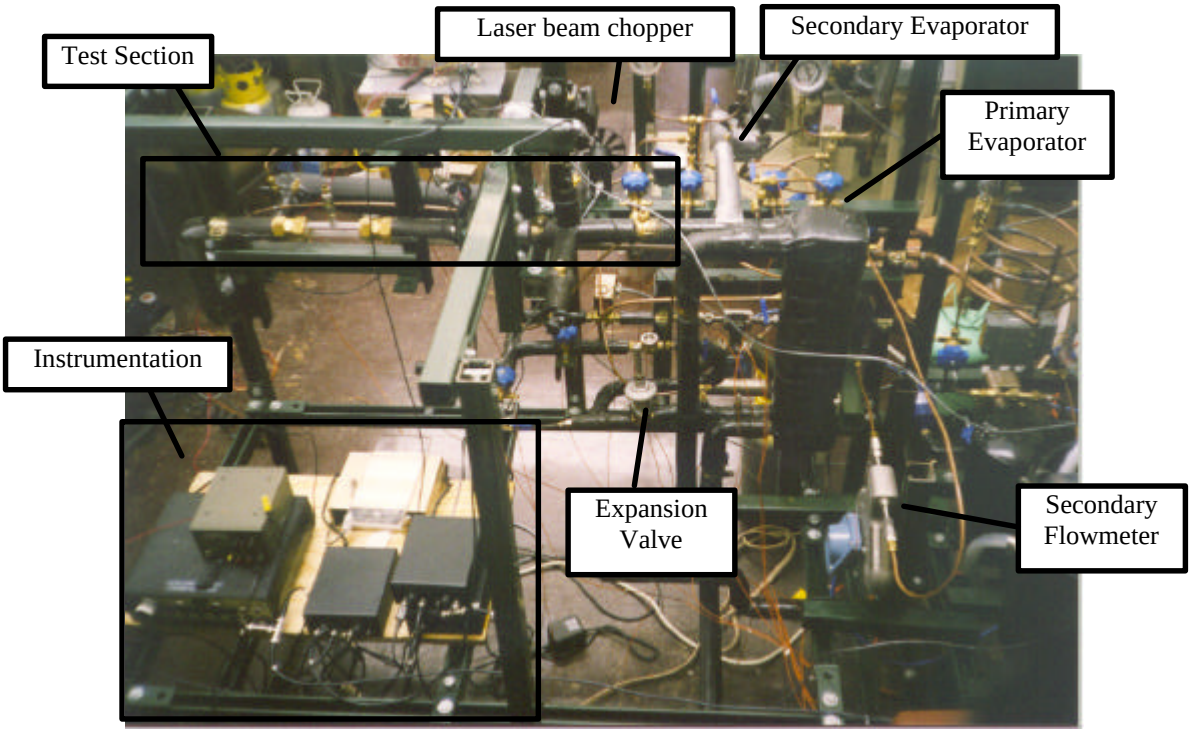

Figure 2-3. Photo of evaporators, test section, and instrumentation

The secondary evaporator, shown in Figure 2-3, was somewhat unconventional because it was designed to add only small amounts of high quality refrigerant to the test section. Flow rates through the secondary evaporator from 0 to 1.5 grams/sec provided entrained liquid mass fractions (LMF) in the test section from 0 to 3%, depending on main evaporator exit conditions. Since the flow rate was so low, and complete evaporation was not desired, the secondary evaporator required a very small heat load. Sufficient heat could be generated, if and when needed, by

the ambient air such that a hot fluid (heat source) was not needed. The evaporator was simply a 12 inch long by ¼ inch diameter copper tube that had been brazed shut at one end. Then several small holes were drilled in that end such that a uniform spray of high quality refrigerant could be injected into the test section along the streamwise direction. A small needle valve with a micrometer handle served as the expansion device for the secondary evaporator. Two thermocouples monitored the expansion process. One measured the subcooled liquid temperature just upstream of the valve, and the other measured the saturation temperature within the evaporator tube.

2.1.2. Water flow loop

At the heart of the water loop, shown in dashed lines in Figure 2-2, was the 15 Liter (4 gallon) water mixing tank. A Teel ½ hp centrifugal water pump pulled water from the bottom of the mixing tank, and pumped it through the evaporator. Chilled water from the evaporator then recirculated back to the mixing tank. At the same time, some of the hot condensing water was diverted into the mixing tank. The hot condensing water and chilled water from the evaporator mixed in the tank to provide the appropriate inlet water temperature for the evaporator. Water flow rate was controlled via a bypass line and throttling valve connected between the pump discharge and the mixing tank. A drain hose located 20 cm above the bottom of the tank kept the water level in the mixing tank constant.

The water flow loop was flexible enough to provide a wide range of subcooled refrigerant temperatures from 4 to 25°C. There were two ways the water loop could be configured in order to achieve this range. First, building cold water supply could be routed directly through the subcooler and on into the drain. This provided a functional range of 12 to 25°C. Second, a small percentage of chilled water from the evaporator could be routed through the subcooler to reach the lower end of the range from 4 to 12°C. For all of the runs conducted in this study the target subcooled temperature was 16°C, so building water was always used in the subcooler.

2.1.3. Test section

The test section consisted of a laser section, the MEMS resistance sensor, a glass tube for flow visualization, a static flow mixer, a calorimeter, and several thermocouples and pressure transducers for monitoring flow conditions. The unsteady mixture of superheated vapor and entrained liquid droplets from the evaporators first passed through the laser section. It consisted of a 2.0 mW Helium-Neon laser, a light chopper, and two photodiodes. The light chopper and other related laser instrumentation are discussed in section 3.3. The laser, shown in Figure 2-6, was aimed through an optical window perpendicular to the flow. Some of the beam was scattered by refrigerant droplets, and the rest passed through the flow stream unaffected. The unaffected laser light was collected by a photodiode positioned directly across the flow stream along the laser axis. A portion of the scattered beam was collected by a second photodiode located above the flow centerline, as seen in Figure 2-4. The entrained refrigerant droplet volume can be measured from these two photodiode signals

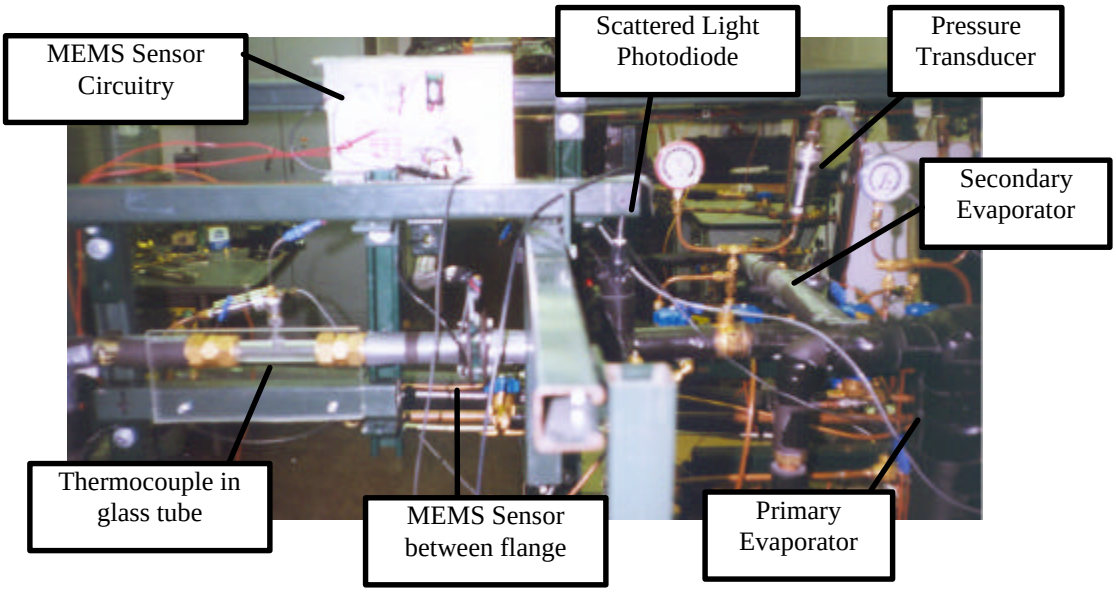

Figure 2-4. Photo of the test section

After the laser section, the flow encountered the MEMS resistance sensor. The sensor was mounted between two glass plates and then installed into a flange in the test section piping. A detailed discussion of the sensor design, fabrication techniques, and theory of operation is left for Chapter 4.

After passing the MEMS sensor, the flow entered a 5" long x 1" OD glass tube. The glass tube allowed for evaporator exit flow visualization. A thermocouple (beaded type) was inserted into the tube through a ¼ inch diameter glass tube (forming a tee). The thermocouple was secured with a compression fitting using Teflon ferrules, allowing the position of the thermocouple to be adjusted. This was desirable because under certain flow conditions having a high liquid mass fraction, splashing liquid would submerse the thermocouple causing drastic drops in the sensed evaporator exit temperature.

Next was the static mixer. It is shown in Figure 2-6, along with the calorimeter. The mixer was designed to stir the flow such that all of the entrained liquid was completely evaporated by the surrounding superheated vapor. Provided liquid was present, conditions at the exit of the mixer would be uniformly superheated at a temperature less than the original superheat temperature. Pressure drop in the mixer was marginal, and has been measured at no more than 3 kPa during conditions of interest. The static mixer consisted of a 6 inch long by 2¼-inch diameter copper tube with a helical copper sheet inside. The helix provided enough mixing to allow LMF measurements as much as 5%.

To directly measure the quality of the evaporator exit fluid, a calorimeter for measuring refrigerant entrained mass fraction completed the test section. It should be noted that the calorimeter was not used in this capacity for the majority of test conditions performed in this study. The calorimeter consisted of a 3,450 Watt Chromalox finned tubular heater inserted into 1-3/8 inch OD copper tube. The heater was 48 inches long with 4½ fins per inch. The calorimeter was well insulated, and was instrumented with thermocouples and pressure transducers at the entrance and exit. Heater power could be conveniently adjusted by a variac, and the power output was measured directly with a watt transducer. The thermocouples, pressure transducers, and watt transducer are

detailed in the next section. The calorimeter served two purposes. First, when the system was running with relatively little liquid at the evaporator exit the heater was used to ensure that all of the liquid had been evaporated before entering the compressor. Second, the calorimeter could be used when the evaporator is fully wetted to measure exit quality.

2.2. Instrumentation

The refrigeration flow loop has been instrumented to measure refrigerant mass flow, pressure, temperature, calorimeter heater power, laser light intensity for Mie scattering experiments, and MEMS sensor voltages. Each type of measurement is discussed separately in this section. This includes the particular equipment used, any calibration procedures performed, and an assessment of measurement uncertainty.

2.2.1. Pressure measurement

Three absolute pressure transducers, one differential pressure transmitter, and one gage pressure transmitter were used to monitor refrigerant flow conditions. The location of these sensors is indicated in Figure 2-6. A Sensotec 0 to 500 psia (0 to 3,450 kPa) absolute pressure transducer was located in the subcooled refrigerant line before the expansion valve of the main evaporator. The evaporating pressure and the static mixer exit pressure were measured by two Sensotec 0 to 200 psia (0 to 1,380 kPa) absolute pressure transducers. All three Sensotec transducers had a 0 to 5 VDC output and a reported accuracy of ±0.1% of the full scale reading. Since these transducers were newly purchased, the factory calibration factors were used during data collection. The main evaporator differential pressure was measured by a Setra 0 to 2 psid (0 to 13.8 kPa) differential pressure transmitter. It had a 4 to 20 mA output, so a 250 Ohm resistor was used at the backplane of the multiplexer to convert the current output to the standard 0 to 5 VDC. A Setra 0 to 250 psig (0 to 1,720 kPa) gage pressure transmitter measured the calorimeter exit pressure. It had a reported accuracy of ±0.13% of the full scale reading at constant temperature. Since this transmitter measured gage pressure, it was necessary to record the barometric pressure during each day of data collection. The barometric pressure was measured with a Princo Instruments 20 to 32 inHg (67.7 to 108 kPa) mercurial barometer. It should be noted that the differential pressure transmitter and the gage pressure transmitter were both calibrated in-situ against the Sensotec pressure transducers.

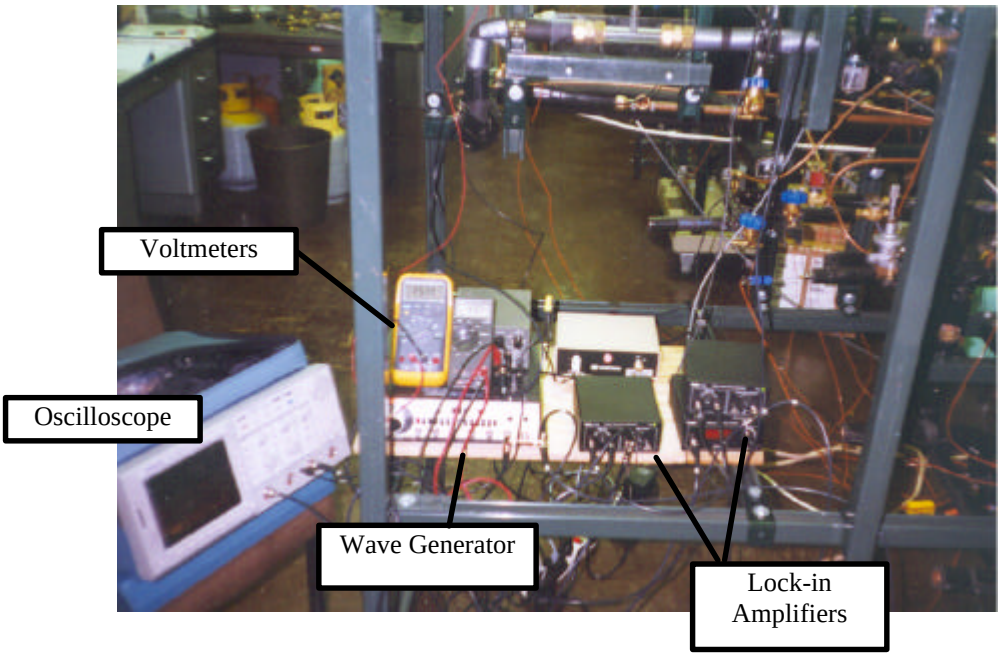

Figure 2-5. Photo of instrumentation

2.2.2. Temperature measurement

All of the temperatures throughout the refrigerant and water flow loops were measured with Omega type T ungrounded beaded thermocouple probes. The beaded thermocouples were chosen, as opposed to the shielded type, so that the thermocouple junction would be directly exposed to the flow conditions and a faster response time could be attained. This was especially important in the test section where fast, unsteady processes occurred. The thermocouples were calibrated, along with the measuring system, over a range of 0 to 30 °C in an isothermal bath against NIST traceable thermometers. The estimated uncertainty of the thermocouples is ±0.1°C.

2.2.3. Refrigerant mass flow measurement

Two Micro Motion ELITE™ coriolis effect mass flow sensors were used to measure refrigerant mass flow rates. The main evaporator flow was measured by a model CMF025 sensor with a 0 to 40 lb/min (0 to 300 g/sec) range, while the secondary evaporator flow was measured by a model CMF010 sensor with a 0 to 3 lb/min (0 to 23 g/sec) range. Both flowmeters, shown in Figure 2-3, were used in conjunction with their own model RTF9793 Field-Mount Transmitter, which outputs both flowrate and fluid density. The transmitters can be seen in Figure 2-6. The flowmeters were factory calibrated and had a reported accuracy of ±0.10% of F.S. ±[zero stability ÷ flowrate ×100]% of the measured rate. The zero stability of the CMF025 sensor was 0.001 lb/min and for the CMF010 it was 0.00015 lb/min.

2.2.4. Power measurement

The calorimeter heater power was measured with an Ohio Semitronics 0 to 4 kW (0 to 13,600 Btu/hr) watt transducer, shown in Figure 2-6. It was calibrated in situ against two Fluke 4.5 digit multimeters; one measuring voltage across the heater and the other wired as an ammeter measuring heater current. The watt transducer has a reported accuracy of ±0.04% of the full scale reading.

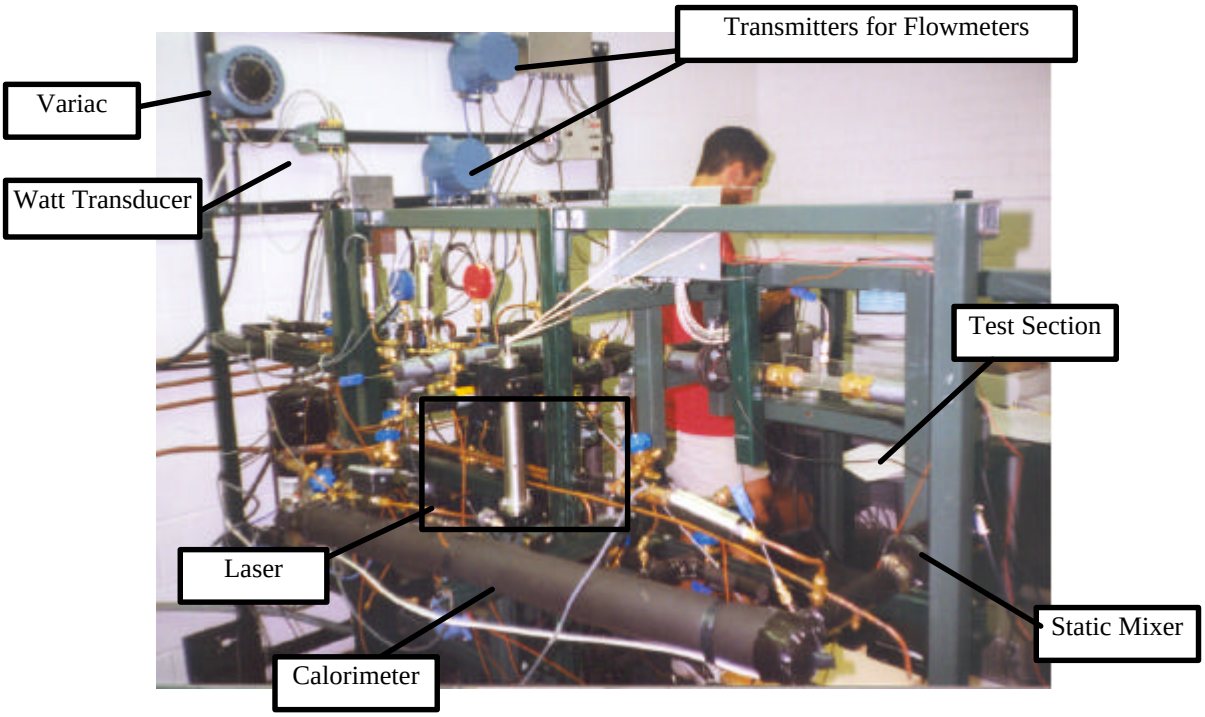

Figure 2-6. Photo of the test rig, highlighting the calorimeter, laser, and static mixer

2.3. Laser Equipment

Figure 2-5 and Figure 2-6 show the laser and related instrumentation used in the test section to identify the presence of entrained liquid droplets. The hardware included a 2.0 mW Helium-Neon laser and power supply, a light chopper, two photodiodes, and two ThorLabs lock-in amplifiers. The light chopper was a 4 inch diameter windmill-shaped disk having 10 blades that "chopped" the beam at a user specified frequency. The laser beam was directed through the test section pipe, perpendicular to the flow direction. A portion of the laser beam was scattered by entrained liquid droplets. Some of the scattered light was collected by the photodiode located 3 inches above the flow centerline. The unscattered portion of the laser beam was either absorbed by the refrigerant, or passed through unaffected to the second photodiode located across from the laser. The photodiodes output a voltage signal proportional to the collected light intensity, and these signals were routed through coaxial cable to a pair of lock-in amplifiers. The lock-ins can either output the unamplified photodiode signal through their monitor outputs, or they can throw out unwanted frequencies, and noise, by comparing the photodiode signal to a reference signal. If a reference signal is used, which for our case was the chopper frequency, then the lock-in will filter out all frequencies in the input signal except that of the reference signal. In this way, the lock-in is an extremely powerful tool for filtering noise from the photodiode signal.

2.4. Data Acquisition Hardware and Software

The data acquisition hardware included a Gateway Pentium P5-133 MHz personal computer (PC) connected via standard HP-IB interface to a Hewlett-Packard (HP) 1300A B-size VXI Mainframe. The mainframe housed a HP E1326B 5 ½ digit multimeter, a HP E1345A 16 channel relay multiplexer, a HP E1347A 16 channel

thermocouple relay multiplexer, and a HP1353A 16 channel thermocouple FET multiplexer. The multimeter and the three multiplexer boards were arranged in a scanning digital multimeter configuration. The HP equipment was purchased because it provided

1. High measurement accuracy down to the micro-volt range, in particular for unamplified thermocouple voltages,
2. High speed temperature measurements up to 100 K switches per second with the FET multiplexer, and
3. Convenient measurement of DC voltage, RMS AC voltage, 2-wire resistance, 4-wire resistance, and temperature (thermistors, RTD's, thermocouples).

All data acquisition programming was done using the HP-VEE™ (Visual Engineering Environment) version 3.21 software program. HP-VEE™ is a general purpose, high level, iconic programming environment similar to National Instruments LabView™. The software provides features for instrument control, data acquisition, data processing data analysis, and file management.

Chapter 3: MEMS Resistance Sensors

3.1. Overview

This chapter describes the efforts of this study to design, manufacture, calibrate, and test a MEMS resistance sensor to be used in conjunction with micro-valves for controlling parallel plate evaporators in refrigerators and heat pumps. The MEMS sensor is actually three sensors in one. It consists of three separate serpentine nickel (Ni) resistors that are evaporated on a silicon wafer 250 μm thick. The serpentine resistors, shown Figure 3-1, are very thin (~1000 Angstroms) and measure 0.0625 mm^2, 0.25 mm^2, and 1.0 mm^2 in total surface area. Since this will be the first generation of MEMS sensors, it is advantageous to have three sensors on the same substrate in order to compare the effect of sensor size (surface area) on sensitivity to liquid droplets. A constant DC current, in the milli-amp range, passing through the sensors provides i^2R self-heating, so that a droplet will evaporate when it strikes the sensor. The evaporation of droplets on the sensor surface causes the sensor temperature, and resistance to decrease. It is important that the thermal mass of the resistors is extremely small to give a very fast time response to refrigerant droplets impinging on the surface. Experiments were conducted to measure the time-varying voltage signal of each sensor while exposing the sensors to known liquid fractions in a superheated vapor. The sensor output signal can be correlated in both time and frequency domains with thermocouple signals, laser light intensity scattered by the entrained liquid droplets, and the time averaged liquid mass fraction.

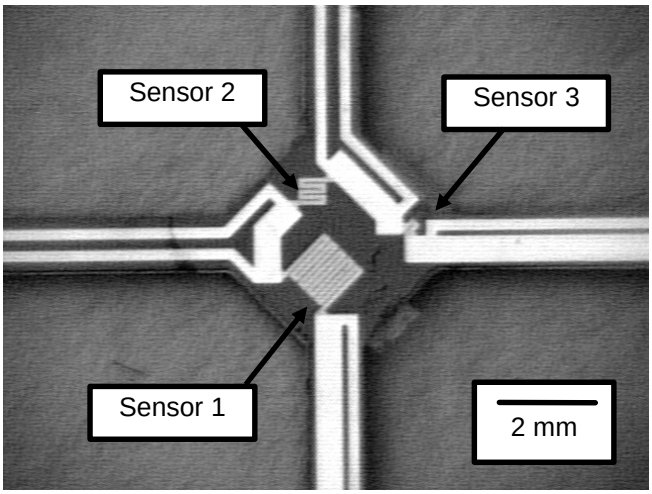

Figure 3-1. MEMS serpentine resistance sensors

3.2. Theory of Operation

At high superheats, or evenly distributed evaporator flows, the sensor will work much like a hot wire anemometer, where the self-heating will cause the actual sensor temperature to be elevated above the free stream temperature. The extent to which the sensor temperature is higher will depend on the sensor current, the temperature coefficient of the sensor, α [$°C^{-1}$], the convective heat transfer coefficient between the sensor and the free stream, and the free stream temperature. With the presence of liquid droplets the story becomes a little more

complicated. Initially, as small amounts of droplets strike the sensor they will be evaporated by the i^2R sensor heat. As more and more liquid coats the sensor, the sensor temperature is driven lower, until the sensor is completely saturated and can no longer evaporate droplets before the next one strikes. When the sensor is completely wetted there is a thin film of boiling liquid covering the surface, so the sensor temperature will approach T_e, the excess temperature above the saturation temperature of the boiling liquid required to drive the boiling process. Thus, at any given time the sensor temperature can vary from an upper limit above the free stream vapor temperature to a lower limit of T_e, which is slightly greater than T_{sat} determined at the evaporator exit pressure. What this means from a control viewpoint is that one sensor alone, located in the evaporator outlet pipe, can not provide an accurate measure of superheat, especially when liquid is present due to maldistribution. In which case it might be advantageous to use a second sensor in a location where it would be sheltered from droplet impingement in order to measure the vapor temperature, and determine superheat.

3.3. Minimum Gap Serpentine RTD Design Equations

The smaller we can make the sensor, while maintaining a high degree of functionality with regard to temperature accuracy and liquid detection capability, the more economically viable the technology becomes. It is important to remember that ultimately these sensors are to be ganged together so that the outlet state of each refrigerant channel can be measured. In plate heat exchangers the refrigerant passes are typically not more than a few millimeters wide. This puts a constraint on the allowable physical size of the sensor. The RTD sensors designed and built for this study are a thin metal film that serpentines back and forth within a square outline. The idea is to design the sensor with a minimum gap between serpentine lengths so that a long resistor can be compacted into the smallest possible surface area. Figure 3-2 shows the general shape of the sensors used in this study, with the important dimensions labeled symbolically. There are six parameters (shown in Figure 3-2) that define the sensor geometry, and only four of those six are necessary to complete a design (we choose g, n, t, and w). A further constraint is that the number of serpentine lengths, n, must be an integer. Therefore, it is common practice for the designer to select n as one of the four necessary parameters, based upon the desired final size and active length of the sensor. The sensors used in this study are the minimum gap type, so the gap, g, is the second necessary parameter in the design. The minimum gap is a function of the resolution attainable during the photolithography process. Masks made by the University of Illinois' Office of Printing Services produced, at best, a 15 μm gap. These masks were made on transparencies from postscript files generated from original AutoCAD drawings of the sensors.

What is important to the designer is the overall size of the sensor. This will influence the active sensor length, the sensor's ability to detect small liquid droplets, and the feasibility of packaging multiple sensors within plate heat exchangers. The maximum serpentine RTD size is

$$a = n(w + g) - g = nw + (n-1)g \tag{3.1}$$

Another key parameter in the sensor design is the active length, *l*. The active length is defined as the total centerline length of the serpentine resistor. For long RTD's with many serpentine passes (n > 10), or RTD's with a large aspect ratio (*l*/w > 100), the centerline approximation gives a reasonably accurate estimation of the true active

length. However, for RTD's with few serpentine passes (in the case of our smallest sensor, n = 2), or small aspect ratios, this approximation breaks down because electric current always flows in the path of least resistance. In other words, a larger percentage of the current will flow along the inner corners of the serpentine, rather than along the centerline and the outer corners. Keeping with the centerline approximation, the active sensor length can be written as

$$l = n(a - w) + w + (n-1)g + (n-1)w \tag{3.2}$$

$$l = na + (n-1)g \tag{3.3}$$

Combining this result with eq. (3.1) and simplifying gives the active length in terms of the design variables g, n, and w

$$l = n^2(w + g) - g \tag{3.4}$$

3.4. Design of Serpentine Resistors for Constant Heat Flux

For simplicity, and to aid in comparing the effect that sensor size has on its ability to detect entrained liquid, the three serpentine resistors were designed to have equal surface heat flux. The resistance of the serpentine, assuming constant temperature throughout the active sensor length, is

$$R_s = \frac{\chi l}{A_{cs}} \tag{3.5}$$

where A_{cs} = wt is the cross-sectional area of the serpentine, and χ is the resistivity of the metal film. The bulk value of resistivity for nickel given in the literature χ = 6.84 μΩ-cm has been used in this design [1]. The heat flux per unit surface area of the sensor is

$$\dot{q}'' = \frac{i_s^2 R_s^2}{A_s} \tag{3.6}$$

where i_s is the sensor current, and A_s is the surface area which can be expressed in terms of the design variables g, w, and n

$$A_s = wl = w\{n^2(w + g) - g\} \tag{3.7}$$

The concept of the sensor is to be able to evaporate, and detect individual liquid droplets. Barnhart has employed P/DPA laser diagnostics to measure average droplet diameters of 50 microns after the dryout point of horizontal tube evaporators [2]. This serves as a good starting point for designing the MEMS sensors. The power required to evaporate a 50 μm diameter droplet of refrigerant R-22 is 0.017 mW. As an upper bound, assume the maximum droplet diameter is 500 μm, an order of magnitude larger. The maximum power for evaporation would be 17 mW. This assumes that a droplet will fully wet the sensor surface, and be fully evaporated before the arrival of another droplet.

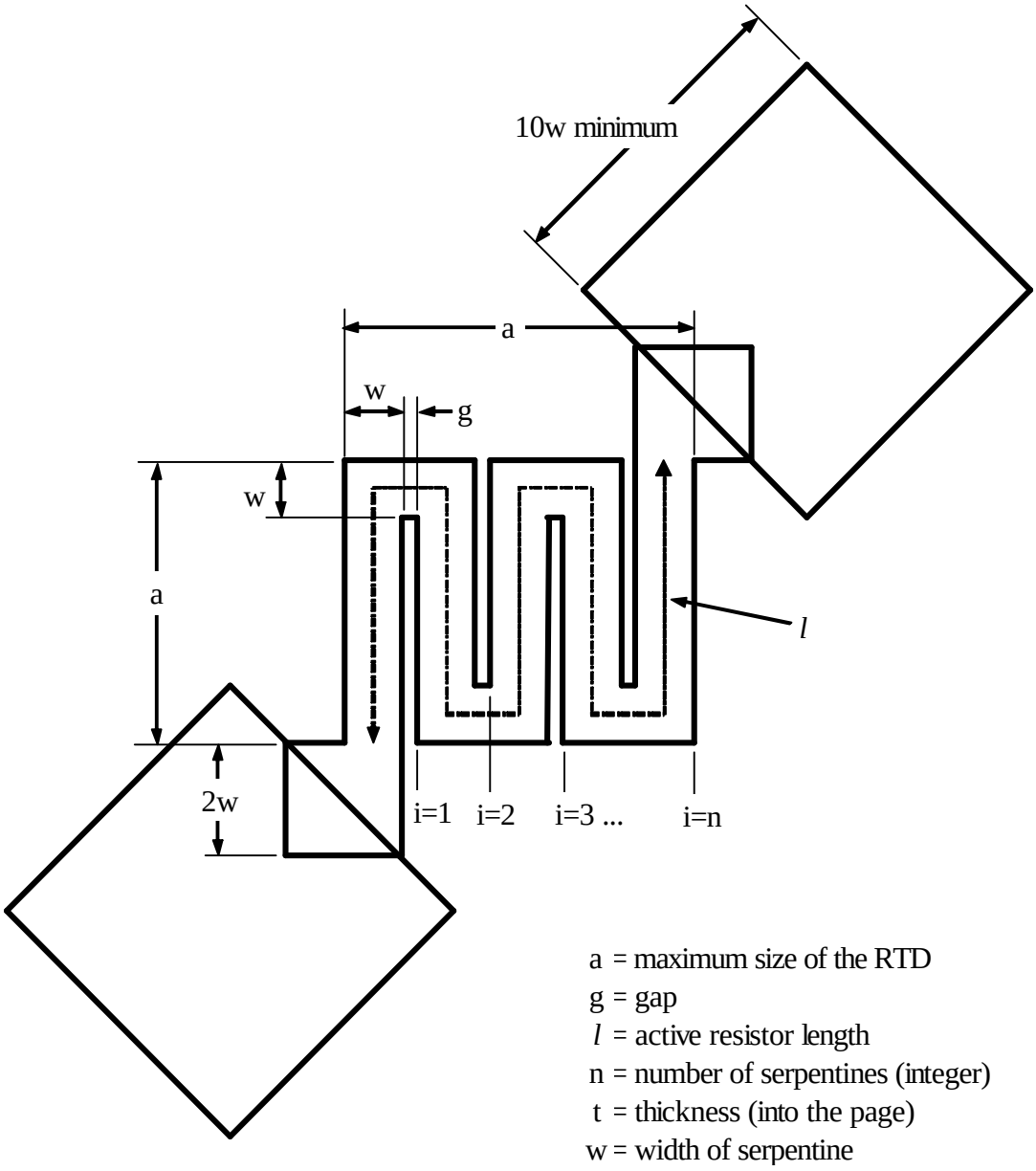

Figure 3-2. Dimensions of minimum gap serpentine resistors

The allowable size of the sensor is dictated by plate evaporator geometry and the mechanisms of droplet evaporation. Plate geometry provides an upper limit to the sensor size of around 1 mm^2. If the sensor were any larger, it would be impossible to install within the plate outlet. Droplet evaporation provides the lower bound on size. It is probably safe to assume that entrained droplets indeed have a characteristic dimension of 50 μm. A sensor that is smaller than the smallest characteristic dimension of a droplet would be unable to distinguish between small and large droplets, because every droplet in the flow stream would be capable of fully wetting the sensor surface. Thus, the characteristic sensor dimension, a, of the three sensors was selected to span the range of 50 microns to 1 millimeter. Specifically, we tried to target 1, 0.5, and 0.15 mm for the characteristic size of the three

sensors. Two of the other key sensor dimensions, g and t, were determined by microfabrication constraints. The gap, g, should be as small as possible to keep the sensor size small. Our microfabrication process yielded a 25 μm minimum gap. Thickness, t, also needs to be small to reduce the sensor thermal mass. A thin layer of nickel, 1000 Å thick, was placed on the silicon substrate to form the serpentine resistors.

With g, and t fixed by microfabrication constraints, and the approximate size, a, given for each sensor, we only need to determine the serpentine width, w, of the serpentine. In order to do this, the nominal sensor resistance must be set such that when a small DC current is applied to the sensor, the voltage drop is in the range of 1 to 5 VDC. A majority of instruments and transmitters have outputs in this range, so signal amplification would not be necessary, and the signal could be read directly with a multimeter. To keep power requirements of the sensor to a minimum, the design current should be in the range of 1 to 25 mA. Using Ohm's Law with a 25 mA current and 5 VDC voltage drop gives a sensor resistance of 100 Ω. Assuming this will be the design resistance for the largest resistor (a = 1 mm), then the heat flux per unit area will be $\dot{q}'' = 62.5$ kW/m^2 when the current is 25 mA. Given the target dimensions, surface heat flux, and design current, the designer can apply eq. (3.2) to (3.7) and iterate to determine the final values of the four key parameters g, n, t, and w. Table 3-1 summarizes the final design parameters of the three serpentine resistors that were made for this project. It should be noted that the values in the table are design values only, and should not be taken as exact quantities. The actual size of the sensors is determined by the resolution of the microfabrication process, so each sensor needs to be calibrated to determine precisely the reference resistance. However, in future calculations requiring sensor dimensions, the values in the table will be used because they are within reasonable accuracy for our purposes.

Table 3-1. Design parameters for the serpentine RTD's

sensor	a [μm]	n	g [μm]	w [μm]	*l* [μm]	A_s [mm^2]	R_{design} [Ω]	$\dot{q}''$ [W/m^2]
1	975	10	25	75	9975	.748	91.0	122 - 76k
2	483	5	25	76.5	2513	.192	22.9	119 - 74.6k
3	189	2	25	82	403	.033	3.67	111 - 69.5k

3.5. Sensor Fabrication

3.5.1. General description

A thin rectangular silicon wafer is the foundation of the MEMS sensor. On it are the three serpentine Ni resistors, two thick gold current leads, and 6 thin gold voltage leads. Two of the voltage leads are unused, and were added solely to provide redundancy in case a problem arose during fabrication. The sensors are suspended in the middle of the flow stream by four narrow silicon bridges that have the full thickness of the wafer. The bridges in earlier sensor generations were as thin as 40 μm, but that proved disastrous as the thin bridges were not strong enough to withstand the flow in the test section pipe. These features are highlighted Figure 3-3, which shows the complete MEMS sensor after microfabrication. Immediately behind the sensors, the silicon has been etched back to a thickness of only 40 μm. This helps minimize heat conduction losses through the substrate, and assures that most of the self-heating is dissipated by convection to the surrounding vapor and conduction to liquid droplets boiling at the surface.

3.5.2. Microfabrication

For a detailed description of the microfabrication techniques used to produce the sensors, the reader is directed to the work of Shannon et al. [3]. The specifics of microfabrication are relevant to this project only with regard to the constraints that fabrication techniques placed on the sensor design. This study is not concerned with the impact and contribution that the sensor fabrication techniques have to the world of MEMS. Rather, this study views the MEMS sensor as a potential tool with which to measure and control maldistribution in multi-channel evaporators. It is the intent of this project to assess the feasibility of using these devices to realize a sensing, and actuation strategy for multi-valve flow control.

3.5.3. Packaging and installation in refrigerant piping

The prototype MEMS sensor is very large, at least with respect to the typical scale of most MEMS devices. It is also flat, brittle, and much too delicate to be directly inserted into the refrigeration piping. In an effort to protect the sensor from catastrophic fracture during service, it has been mounted in a "sandwich" between two pieces of ¼" thick plate glass. A thin sheet metal plate having the same rectangular shape as the wafer is placed within the sandwich to help support the silicon bridges exposed to the refrigerant flow. First, a two-part epoxy is spread evenly, and extremely thin, across one of the pieces of glass using a razor blade. The sheet metal is placed on this piece of glass and allowed to dry. Then another thin layer of epoxy is spread over the sheet metal and glass. The sensor is carefully placed in exact alignment over the sheet metal support plate. At the same time a thin layer of epoxy is laid over the second piece of glass, and then placed in contact with the sensor. The sandwich is clamped in a specially designed fixture and left to harden for 24 hours. Once the epoxy has set, the sensor is mounted within the test section in a copper pipe flange. Two o-rings in the flange provide a pressure tight seal against the glass. Certainly, other less fragile materials besides glass plate could have been used to create the sandwich. However, glass was selected because it is transparent which allows the entire wafer to be inspected after the epoxy has hardened. This proved to be very useful, since several sensors were rendered useless after uneven clamping in the flange caused complete cracking of the silicon wafer.

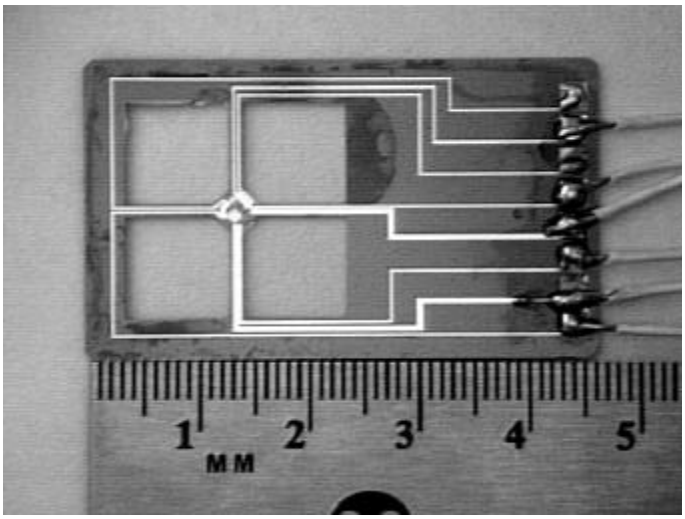

Figure 3-3. Microfabricated sensor with 3 serpentine RTD's

3.6. Sensor Calibration

3.6.1. 4-wire resistance technique

The principle of operation of a serpentine resistor is the fact that the resistance to the flow of electricity is a function of the cooling due to the surrounding vapor stream (and possibly entrained liquid). The resistance as a function of sensor temperature, T_s, can be expressed as

$$R_s = R_o\left(1+\alpha\left(T_s - T_o\right)\right) \tag{3.8}$$

where R_o is the resistance at the reference temperature, T_o = 0°C, and α [°C^{-1}] is the temperature coefficient of resistivity. Since α is a constant material property in the range of temperatures of interest to refrigeration, eq. (3.8) reduces to the following linear relationship for $R_s(T)$

$$R_s(T) = R_o + \alpha R_o T \tag{3.9}$$

The above equation provides a basis for calibrating the sensor. The reference resistance R_o is simply the y-intercept of $R_s(T)$, and αR_o is the slope. The calibration is complete when α and R_o have been determined for each of the three serpentine resistors.

An experiment for calibrating α and R_o for each serpentine resistor was carefully performed over several days. The complete MEMS sensor and a calibrated type-T beaded thermocouple were exposed to 3 different temperatures in order to develop the R_s vs. T_s data. The 3 temperatures were achieved by placing the sensor and thermocouple in (1) ambient conditions, (2) a 3 cubic-ft refrigerator, and (3) the freezer compartment of the refrigerator. The sensor was exposed to each temperature for a period of 24 hours to ensure equilibrium conditions were reached. Sensor resistances were measured with the HP 5 ½ digital multimeter using a 4-wire technique. To minimize any self-heating of the resistors during the 4-wire measurements it is necessary to keep the source current to a minimum. The effect of self-heating can be minimized by selecting a higher resistance range on the multimeter since less current is applied. However, higher ranges yield lower resolution. It was determined that the default setting of the multimeter (16384 Ω range, and 61 μA) was adequate to prevent self-heating and still provide ± 15mΩ resolution (see p.87 in [4]). The results of the calibration are presented in Table 3-2.

Table 3-2. Summary of MEMS serpentine resistor calibration by 4-wire resistance method

MEMS sensor	nominal surface area, A [mm2]	reference resistance at To = 0°C, Ro [Ω]	temperature coefficient of resistivity, α [°C-1]
Rs1	1.0	107.03	.0045
Rs2	0.25	27.51	.0044
Rs3	0.0625	5.01	.0043
average			.0044

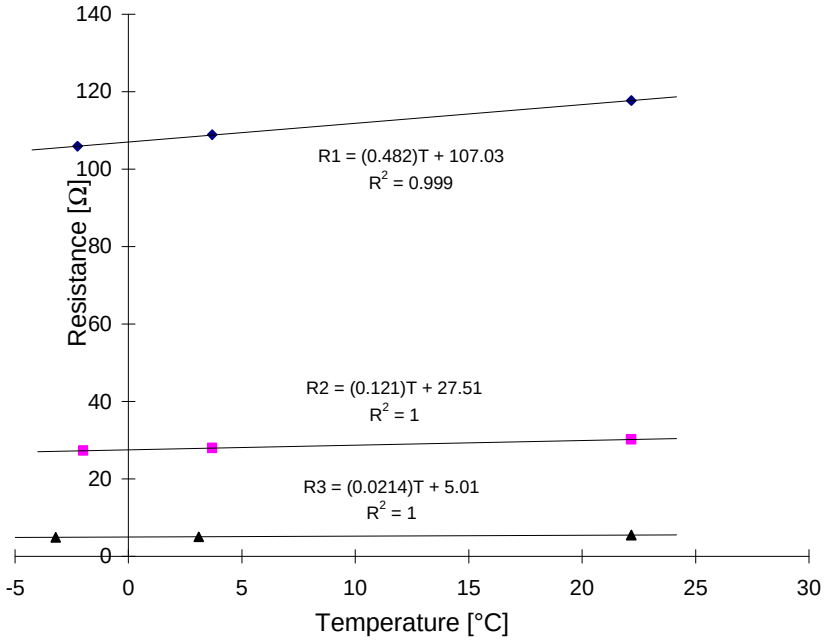

Figure 3-4. MEMS serpentine resistor calibration by 4-wire resistance method

The average temperature coefficient of resistivity for the three resistors was found to be 0.0044 $°C^{-1}$. Since α is a constant material property, this average value will be used for all three resistors in future calculations. Bruun reports a typical value of $\alpha_{20} = 0.0038\ °C^{-1}$ for platinum hot-wire elements at room temperature (20°C) [5]. Our thin-film serpentine resistors show a 16% improvement in temperature sensitivity compared to platinum hot-wire anemometers.

3.6.2. In-situ calibration technique

An in-situ calibration of the sensors was also performed. The in-situ method has the advantage of accounting for any errors in the sensor temperature measurement that might be introduced by the data acquisition system. This method provides a means of determining sensor temperature, T_s, directly from voltage and current measurements, without relying upon explicit knowledge of α, R_o, and T_o. To perform this calibration, the sensor was installed in its mounting flange in the test section exactly as it was during normal operation. This means using the same wiring to the current source, the ammeter, and the HP multimeter backplane. The sensor was exposed to two different vapor temperatures by running the refrigeration system with the main evaporator at a high superheat (ΔTsup > 9°C) to ensure no droplets were present. Flow through the secondary evaporator was valved off during the calibration procedures.

For a sensor exposed to two different vapor temperatures, $T_{\infty,1}$ and $T_{\infty,2}$, assuming the vapor velocity remains constant, the sensor voltage, V_s, as a function of current, i_s, will be as shown in Figure 3-5. The deviation of $V_s(i_s)$ from linearity is due to the self-heating of the sensor as the current is increased. In order to approximate the initial slope of $V_s(i_s)$ at $i_s = 0$, the current source was varied from ±2 mA, while the voltage drop across each sensor was measured. In this range, the sensors do not exhibit any significant self-heating. So for very low current, the

sensor temperature, T_s, will be equal to the vapor temperature, T_∞. The initial slopes, m_1 and m_2, at the two calibration temperatures can be written

$$m_1 = \left.\frac{dV_1}{di_s}\right|_{i=0} \quad \text{at } T_{\infty,1} \tag{3.10}$$

$$m_2 = \left.\frac{dV_2}{di_s}\right|_{i=0} \quad \text{at } T_{\infty,2} \tag{3.11}$$

From Ohm's Law, $V = i_s R_s$, we can write

$$\frac{dV}{di_s} = R_s + i_s \frac{dR_s}{di_s} \tag{3.12}$$

In the limit as i_s goes to zero, $\frac{dV}{di_s}$ goes to R_s. Combining this result with eq. (3.8) gives

$$\left.\frac{dV}{di_s}\right|_{i=0} = R_o\left(1+\alpha\left(T_s - T_o\right)\right) \tag{3.13}$$

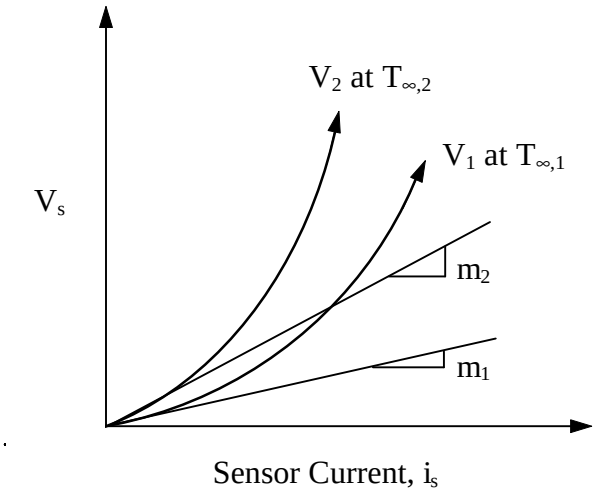

Figure 3-5. Sensor voltage vs. current at two different vapor temperatures, $T_{\infty,1}$ and $T_{\infty,2}$

Then for the two calibration vapor temperatures, $T_{\infty,1}$ and $T_{\infty,2}$, the initial slopes are

$$m_1 = R_o\left(1+\alpha\left(T_1 - T_o\right)\right) \tag{3.14}$$

$$m_2 = R_o\left(1+\alpha\left(T_2 - T_o\right)\right) \tag{3.15}$$

where $T_1 \to T_{\infty,1}$ and $T_2 \to T_{\infty,2}$ as $i_s \to 0$. Subtracting m_2 from m_1,

$$m_1 - m_2 = R_o + R_o\alpha\left(T_{\infty,1} - T_o\right) - \left\{R_o + R_o\alpha\left(T_{\infty,2} - T_o\right)\right\} \tag{3.16}$$

$$m_1 - m_2 = R_o\alpha\left(T_{\infty,1} - T_{\infty,2}\right) \tag{3.17}$$

$$\therefore R_o\alpha = \frac{m_1 - m_2}{T_{\infty,1} - T_{\infty,2}} \tag{3.18}$$

To find the reference temperature, T_o, we can combine eq. (3.14) and (3.15).

$$R_o = \frac{m_1}{1+\alpha\left(T_{\infty,1} - T_o\right)} = \frac{m_2}{1+\alpha\left(T_{\infty,2} - T_o\right)} \tag{3.19}$$

$$m_1 - m_2 = \alpha\left\{m_2T_{\infty,1} - m_2T_o - m_1T_{\infty,2} + m_1T_o\right\} \tag{3.20}$$

$$\frac{m_1 - m_2}{\alpha} = m_2T_{\infty,1} - m_1T_{\infty,2} + \left(m_1 - m_2\right)T_o \tag{3.21}$$

$$T_o = \frac{1}{\alpha} - \frac{m_2T_{\infty,1} - m_1T_{\infty,2}}{m_1 - m_2} \tag{3.22}$$

or,

$$T_o = \frac{1}{\alpha} - C_o \tag{3.23}$$

where

$$C_o = \frac{m_2T_{\infty,1} - m_1T_{\infty,2}}{m_1 - m_2} \tag{3.24}$$

Finally, the fundamental serpentine resistor equation, eq. (3.7), can be combined with eq. (3.18) and eq. (3.23) to solve for the sensor temperature as a function of the measured current and voltage as follows,

$$R_s = R_o\left(1+\alpha\left(T_s - T_o\right)\right) \tag{3.25}$$

$$\frac{R_s}{R_o} - 1 = \alpha\left(T_s - T_o\right) \tag{3.26}$$

$$T_s = \frac{R_s}{R_o\alpha} - C_o \tag{3.27}$$

$$T_s\left(V_s, i_s\right) = \frac{1}{m_1 - m_2}\left\{\left(T_{\infty,1} - T_{\infty,2}\right)\frac{V_s}{i_s} + m_1T_{\infty,2} - m_2T_{\infty,1}\right\} \tag{3.28}$$

The sensor temperature can be determined, using eq. (3.28), directly from the measured current, i_s, and voltage, V_s. The calibration provides the other four parameters (m_1, m_2, $T_{\infty,1}$, and $T_{\infty,2}$) in the equation. Figure 3-6 shows the calibration of all three sensors at the two temperatures $T_{\infty,1}$ = 9.0°C, and $T_{\infty,2}$ = 14.3 °C. As expected, self-heating is negligible and the sensor voltage is proportional to current when the current is low (less than 2 mA). Linear least squares curve fits are shown for each sensor, and the correlation coefficient is greater than 0.99 for all but one sensor, indicating a strong linearity in the data.

3.6.3. Comparison of results

Sections 3.6.1 and 3.6.2 have outlined two independent calibration techniques for the MEMS sensors. As a means of comparison, the reader is referred to Figure 3-7. In the figure, the calibration of each sensor is compared using both the 4-wire resistance method and the in-situ method. A line representing $T_{4\text{-wire}} = T_{\text{in-situ}}$ is plotted. The symbols on the graph indicate temperatures calculated using eq. (3.1) with the 4-wire resistance calibration data in Table 3-2 , and using eq. (3.21) with the in-situ calibration data in Table 3-3. The graph indicates a good agreement between the two calibrations in the temperature regions of interest to this study, specifically 0 to 15°C. This is in part due to the fact that the calibration temperatures used in the in-situ method were 9.0 and 14.3°C. Extrapolation of the resulting curve fits would naturally lead to higher deviations between the two calibration methods.

Table 3-3. Summary of MEMS serpentine resistance sensor by the in-situ method. ($T_{\infty,1}$ = 9.0°C, and $T_{\infty,2}$ = 14.3 C)

MEMS sensor	$m_1 = \left.\frac{dV_1}{di_s}\right\|_{i=0}$ [Ω]	$m_2 = \left.\frac{dV_2}{di_s}\right\|_{i=0}$ [Ω]	$R_o\alpha$ [Ω/°C]	C_o [°C]
R_{s1}	111.3	113.9	0.491	217.9
R_{s2}	28.6	29.2	0.113	243.6
R_{s3}	5.18	5.30	0.023	219.8

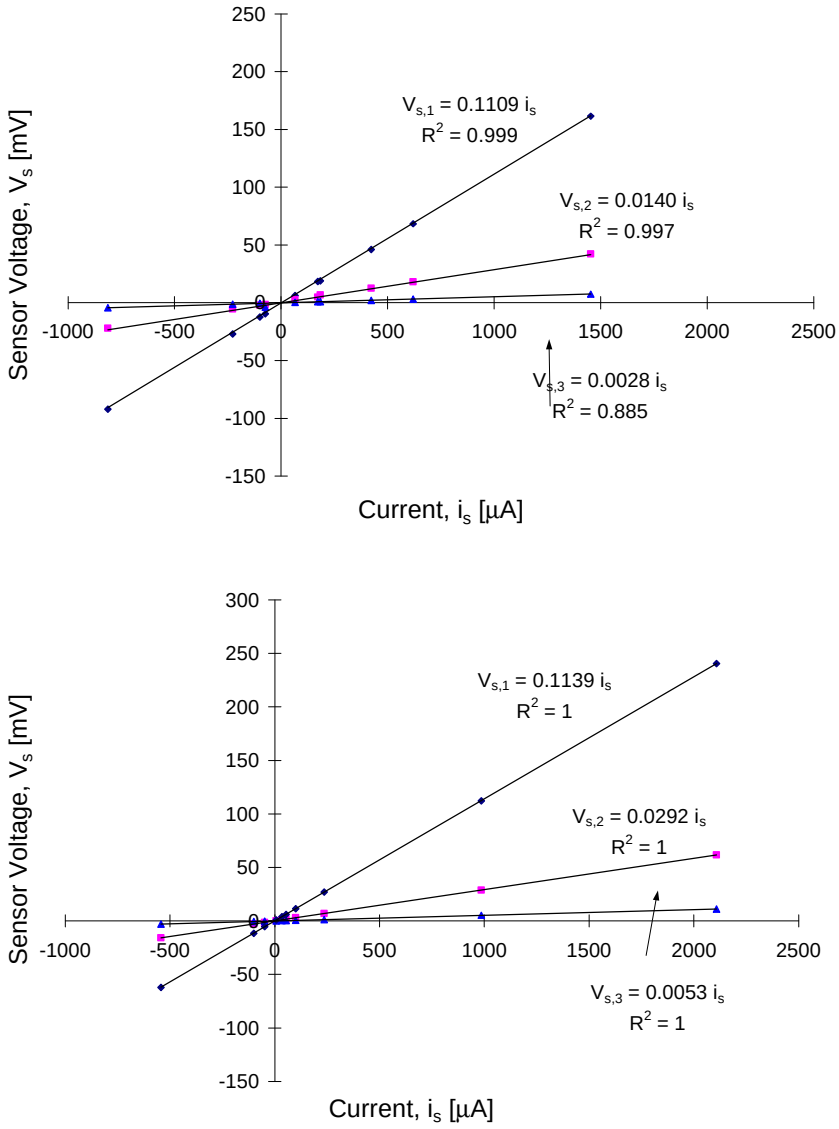

Figure 3-6 In-situ calibration of MEMS sensors at two temperatures, $T_{\infty,1}$ = 9.0°C (top), and $T_{\infty,2}$ = 14.3°C (bottom)

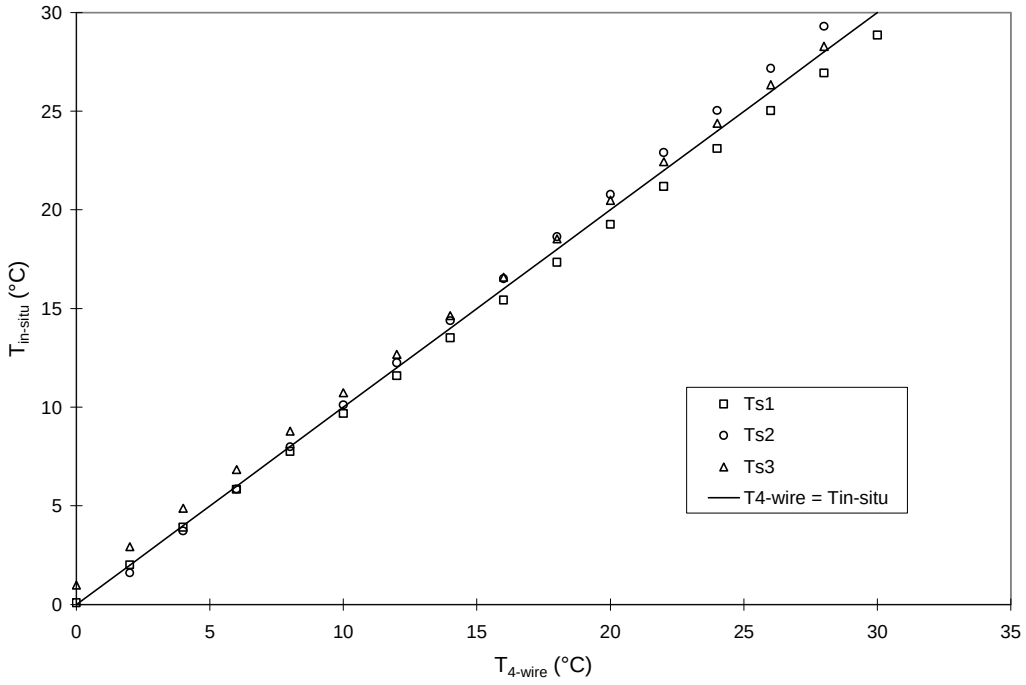

Figure 3-7. Comparison of MEMS sensor calibration techniques

Chapter 4: Experimental Procedures

4.1. Experimental Scope

This chapter will familiarize the reader with the procedures for each experiment and the methods used to collect and process the data. The following list describes the objectives of each experiment.

1. *Methods of Calculating LMF* – Develop a consistent method for quantifying the time averaged liquid mass fraction (LMF) at the exit of a plate evaporator.
2. *Correlating Instrument Signals to LMF* – Compare the signals of a thermocouple, MEMS thin-film resistance sensor, and scattered laser light during the presence of small quantities of entrained liquid droplets.
3. *Characterizing Exit Flows of Plate Evaporators* – Measure the exit conditions of a 3-ton plate evaporator at various superheats to demonstrate when and how liquid mass fraction (LMF) is manifested at the evaporator exit.
4. *Comparing Thermocouples and MEMS Sensors* – Investigate, using time-domain and frequency-domain analysis techniques, the feasibility of using either a thermocouple or the MEMS sensor to detect and control LMF.
5. *MEMS Sensor Size vs. Sensitivity to LMF* – Investigate how the surface area of a MEMS thin-film resistance sensor affects its ability to detect LMF.

4.2. System Start-up and Operation

The reader is directed to Appendix B for the daily start-up procedures of system. These procedures were followed until a stable operating point was reached close to the test conditions.

Operating the refrigeration loop was sometimes difficult, especially when using the thermostatic expansion valve, because small perturbations of flowrates, or temperatures would take up to 30 minutes to return to steady conditions. However, the expansion device (TXV or MXV) was typically set close to the desired superheat from the previous days operation. When starting the system each day the inlet and outlet water temperatures were set first. This was done by adjusting the hot water makeup flow from the condenser, and by adjusting the water flowrate with the water pump bypass. Then the desired refrigerant setpoints were achieved by making incremental adjustments to the refrigerant flowrate with the compressor bypass needle valves, or by adjusting the TXV superheat setpoint, or by adjusting the evaporator load (water temperatures and flowrate). This was a delicate and time consuming process, and often required several hours to reach the desired conditions.

During start-up it was important to monitor all of the flowrates, pressures, and temperatures on the data acquisition monitor in order to avoid any problems. For example, the evaporator inlet water temperature could not drop below 0°C, because the plate evaporator could have been seriously damaged if the water froze inside. Another parameter that required special attention was the compressor suction temperature. There was no thermocouple in the loop to monitor this temperature, so instead it was checked by hand to make sure the pipe was neither cold nor hot. An adequate temperature was around room temperature. The compressor suction pipe was fed from the calorimeter and the compressor bypass lines. The calorimeter heater power was adjusted so that all liquid droplets have been evaporated, and the vapor stream to the compressor was around room temperature. Both of the needle valves on the bypass lines were also adjusted to provide a mixed compressor suction stream at room temperature.

4.3. Procedures for *Methods of Calculating LMF*

4.3.1. Procedures and data collection

Two methods of calculating LMF were tested: 1) by an energy balance and 2) by direct flowrate measurements. The two methods are compared in section 5.1 to determine which method most accurately measures LMF. For this experiment the main and secondary evaporators were operating in parallel as shown in Figure 6-1. The main evaporator was set to a high superheat temperature while the secondary evaporator injected a small amount of saturated liquid into the test section. There were a total of 14 test runs for this experiment.

4.3.2. Test envelope

For this experiment the main evaporator superheat was held constant at ΔT_{sup} = 12°C. The main evaporator flowrate was also held constant at m_r = 40 g/s while the secondary evaporator flowrate m_2 vaired from 0 to 1.5 g/s. Data collection consisted of only low-speed sampling. A total of 150 data sets of the 20 instrument channels were sampled and recorded for a total of 200 seconds.

Table 4-1. Test envelope for *methods of calculating LMF*

m_r	40 g/s
m_2	0 to 1.5 g/s
$T_{e,in}$	2°C ±0.2°C
ΔT_{sup}	12°C
LMF	0 to 3.5%
$T_{w,in}$ and $T_{w,out}$	adjust to maintain ΔT_{sup} = 12°C

4.4. Procedures for *Correlating Instrument Signals to LMF*

4.4.1. Procedures and data collection

To correlate the thermocouple, MEMS sensor, and scattered light signals to the presence of droplets, a known amount of liquid was injected into the test section. Both qualitative and quantitative comparisons of the signals are made in section 5.2. The main evaporator was run at a high degree of superheat (12°C) to ensure that no liquid was present at the evaporator exit, and a small amount of liquid was added to the test section using the secondary evaporator. The same seven test section instruments listed in section 4.3 were again scanned at high-speeds. In addition, the largest MEMS sensor voltage, and the scattered laser light photodiode voltage were measured using the lock-in amplifiers.

4.4.2. Test envelope

The test envelope for correlating the thermocouple, MEMS sensor, and scattered light signals to liquid mass fraction is quite simple. The refrigeration system was run so that the main evaporator sustained a stable 12°C superheat. This was done to ensure that the evaporator exit contained no liquid. The MEMS sensor current, is, was set at 25 mA for the duration of the experiments. Lastly, the secondary evaporator was used to induce liquid into the test section in the range of 0% < LMF < 4%. It will be shown in section 6.2 that liquid mass fractions greater than 4% are well into the unstable region of plate evaporator operation, and so they were not investigated.

4.5. Procedures for *Characterizing Evaporator Exit Flows*

4.5.1. Procedures and data collection

The goal of these experiments was to record the nature of multi-channel evaporator exit flows over a range of superheats. For these experiments the system was configured for three different cases: 1) TXV control of the main evaporator, 2) MXV control of the main evaporator, and 3) MXV control of the main and secondary evaporators. In cases 1 and 2 there was no flow through the secondary evaporator. The refrigeration loop was run at normal operating conditions (ie: high superheat), and then the evaporator superheat was decreased in each successive run. The reduction of superheat was achieved by maintaining a constant inlet evaporator temperature, $T_{e,in}$, while at the same time lowering the water inlet temperature, $T_{w,in}$. The outlet evaporator temperature, $T_{e,out}$, can never be higher than the water inlet temperature because the evaporator is a counterflow heat exchanger. Therefore, it is possible to control superheat by simultaneously raising or lowering the water inlet temperature, $T_{w,in}$, and by adjusting the superheat setpoint of the TXV.

Data collection consisted of both low-speed sampling of all instrumentation, and high-speed sampling of the test section instrumentation only. The low-speed data was used to measure system behavior over long periods of time, and to calculate energy balances. The high-speed data was used to investigate the transient, non-equilibrium, two-phase flow conditions at the evaporator exit. A total of 150 data sets of the 20 instrument channels were sampled and recorded at low speeds for a total of 200 seconds. The HPVee data acquisition software determines the low-speed data-sampling rate, which was a function of how many channels were multiplexed and how much data was updated on the computer screen. HPVee could have been programmed to sample at a user-defined rate, however that was not necessary for the slow data collection. The computer run time was recorded before each scan so that the exact time between multiplexer scans was known. The majority of low-speed data collection was at an average of 0.6 Hz.

High-speed sampling of the test section instrumentation was taken at a user-set 40 Hz. Seven channels were sampled at this speed to measure

1. Evaporator exit pressure,
2. Static mixer exit pressure,
3. Evaporator exit temperature,
4. Temperature of thermocouple in glass tube,
5. Vs1, the largest MEMS sensor voltage,
6. Vs2, the middle MEMS sensor voltage, and
7. Vs3, the smallest MEMS sensor voltage.

Each channel was scanned a total of 500 times, at 40 Hz, for a total of 12.5 seconds of data collection. The HP multimeter was configured to advance on the external trigger connected to a wave generator putting out a square wave TTL signal. The wave generator output frequency was dialed to exactly 40 Hz using a Fluke digital multimeter. All high-speed data collection was performed immediately after the 3 minutes of low-speed data collection. It can be reasonably assumed that process conditions did not vary significantly during the 60 seconds, or so, it took to switch to high-speed data collection.

4.5.2. Test envelope

The test envelope for *characterizing evaporator exit flows* is shown in Table 4-2. For all cases the mass flowrate, evaporator inlet temperature, and subcooled refrigerant temperature were held constant. Only the superheat temperature, ΔT_{sup}, was varied from high to low superheat in order to describe how conditions at the evaporator outlet become unstable.

Table 4-2. Test envelope for *characterizing evaporator exit flows*

m_r	40 g/s
$T_{e,in}$	2°C ±0.2°C
ΔT_{sup}	12°C, 10°C, 8°C, ... unstable
T_{sub}	15°C ±0.5°C
$T_{w,in}$ and $T_{w,out}$	adjust for desired evaporator load
i_s	25 mA

4.6. Procedures for *Comparing Thermocouples and MEMS Sensors*

4.6.1. Procedures and data collection

An important task of this project is to characterize the output signals of a beaded thermocouple and the MEMS resistance sensors over a range of superheats and LMF. To accomplish this the main evaporator was outfitted with the manual expansion valve described in section 2.2. The manual valve allows the main evaporator to run at a fairly constant superheat, without the transients induced by a thermostatic expansion valve. The main evaporator exit superheat was kept high (12°C) to ensure no entrained liquid was present. A small amount of liquid was added to the test section inlet via the secondary evaporator, and the LMF was calculated using the procedure outlined in section 5.2.

Data collection for these experiments consisted of both low-speed and high-speed data sampling. The same 20 channels measured in section 4.3 were again sampled at low frequency. The same holds true for the 7 channels sampled at high frequency (40 Hz) for 12.5 seconds. During the high-speed data sampling, the MEMS sensor current was set at 25 and 40 mA so that different heating values could be compared.

4.6.2. Test envelope

The test envelope for these experiments is outlined in Table 4-3. Notice that the conditions are very similar to those in Table 4-2, and for good reason. It is important to investigate the behavior of the thermocouple and MEMS sensors over know liquid fractions and superheat conditions would be expected in a real system with TXV control. The superheat was varied from 12°C to 8°C. Anything lower than 8°C superheat caused the main evaporator to spill liquid into the test section which would have biased our measurements of liquid mass fraction.

Table 4-3. Test envelope for *comparing thermocouples and MEMS sensors*

m_r	40 g/s
$T_{e,in}$	2°C ±0.2°C
ΔT_{sup}	12°C, 10°C, 8°C
LMF	0 to 2%
$T_{w,in}$ and $T_{w,out}$	adjust for desired evaporator load
i_s	25 and 40 mA

Chapter 5: Experimental Results

5.1. Methods of Calculating LMF

Maldistribution in plate evaporators is evident when liquid droplets are entrained in the superheated vapor stream exiting the evaporator. One objective of this work is to develop a consistent method for measuring the liquid mass fraction (LMF) of entrained liquid. Two methods for measuring LMF are compared, they are: 1) e*nergy balance method*, and 2) *direct measurement method*. The *energy balance method* is based on the reduction of vapor temperature at the static mixer due to the evaporation of droplets. The *direct measurement method* calculates LMF by independently measuring the mass flowrate of superheated vapor and entrained liquid droplets.

LMF is defined here as the ratio of the mass flow rate of entrained liquid and the total mass flow rate. LMF should not be confused with quality, which describes vapor that is saturated. Assuming liquid droplets and vapor have the same velocity at a given pipe cross-section LMF can be formulated as

$$\text{LMF}\,[\%] = \frac{\dot{m}_{\text{liquid}}}{\dot{m}_{\text{liquid}} + \dot{m}_{\text{vapor}}} \times 100 \tag{5.1}$$

Figure 5-1 shows a schematic of the main evaporator, secondary evaporator, test section with the static mixer, and associated instrumentation. Stream 1 is superheated vapor exiting the main evaporator with a mass flowrate $\dot{m}_r$, temperature $T_{e,out}$, and pressure P_e. For all test conditions the main evaporator was run with 12°C superheat, so it can be assumed with good accuracy that stream 1 is comprised solely of superheated vapor. Stream 2, on the other hand, is a low quality mixture at pressure P_e with mass flow rate $\dot{m}_2$. The two streams mix in the static mixer and exit as a single-phase superheated vapor at temperature T_{mix}. It is assumed that heat loss to the environment is negligible and that all liquid droplets are evaporated before exiting the static mixer.

For the *direct measurement method* the definition of LMF, eq. (5.1), must be modified to give the LMF directly from knowledge of the flow rates $\dot{m}_r$ and $\dot{m}_2$, and stream 2 inlet quality.

$$\text{LMF}\,[\%] = \frac{\dot{m}_2\left(1 - x_2\right)}{\dot{m}_r + \dot{m}_2} \times 100 \tag{5.2}$$

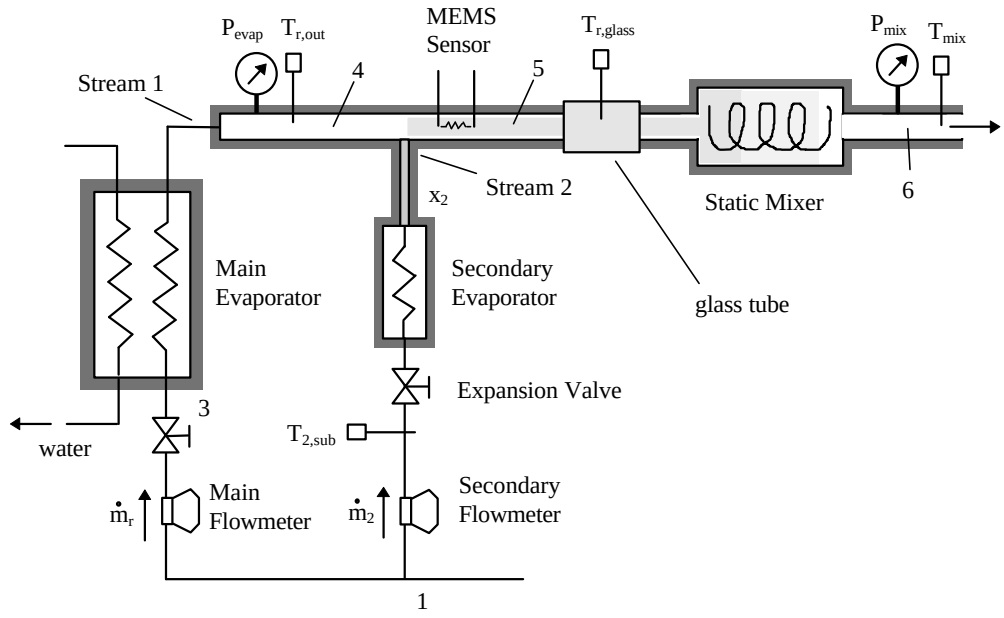

Figure 5-1. Schematic of evaporators, static mixer, and test section instrumentation used to determine LMF

Both mass flow rates are measured by the Micro Motion flowmeters. However, the quality x_2 must be determined from the subcooled liquid temperature before expansion $T_{2,sub}$ (state **1** in Figure 5-2), and the pressure at the exit of the secondary evaporator P_e. It is assumed that stream 2 undergoes a constant enthalpy expansion from $T_{2,sub}$ to a low quality mixture at the exit pressure P_e. The quality x_2 is thereby determined by P_e and the enthalpy of the subcooled liquid before expansion. Figure 5-2 outlines this process on a P-h diagram.

The LMF entering the test section can also be calculated by the *energy balance method*. For this method it is assumed that states **4** and **6** in Figure 5-2 are completely defined by the independent measurements of temperature and pressure. Also, it is assumed that the two streams are completely mixed before exiting the static mixer with no heat loss to the surroundings. State **2** is still at pressure P_e, but this time the quality is assumed to be unknown. An energy balance of the adiabatic mixing of superheated vapor and unknown quality gives

$$\dot{m}_r\left(h_r - h_{mix}\right) = \dot{m}_2\left(1 - x_2\right)h_{fg} + \dot{m}_2\left(h_{mix} - h_{sat}\right) \qquad (5.3)$$

The left hand side of the equation is the energy lost from the superheated vapor stream during the mixing process. The right hand side accounts for the energy gained by the low-quality mixture of stream 2 during evaporation and mixing. The first term is the heat of vaporization required to boil liquid droplets to the saturation temperature, and the second term is the energy necessary to heat saturated vapor to the final state at the static mixer exit. The mass flowrates $\dot{m}_r$ and $\dot{m}_2$ are measured, and all of the enthalpies can be determined from pressure and temperature measurements. The exit quality of the secondary evaporator can now be solved for directly. Once x_2 is evaluated using eq. (5.3) the LMF can be calculated using eq. (5.2).

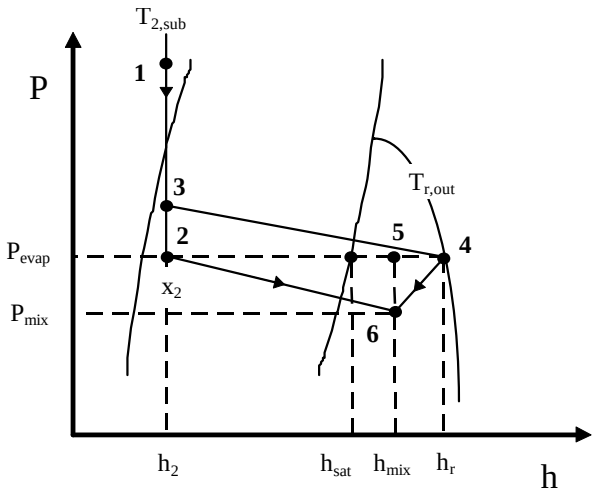

Figure 5-2. P-h diagram of entrained liquid evaporating in a superheated vapor stream

A comparison of both methods of calculating LMF is shown in Figure 5-3. Both sets of data show a linear relationship of LMF to $\dot{m}_2$, the mass flow rate of stream 2. Error bars for each data point indicate the uncertainty in LMF due to instrument errors only. The instrument error was calculated using the methods developed by Moffat [6]. The true LMF at the inlet to the test section is most accurately represented by the *direct measurement method* of eq. (5.2). This statement is based not just on the fact that the *direct measurement method* has less instrument error (smaller error bars), but because the *energy balance method* is based upon several simplifying assumptions. First, the *energy balance method* assumes no interaction between refrigerant and oil. The oil present in the suction line (measured to be 0.2 to 0.3%) will absorb liquid droplets, thereby preventing them from evaporating [7]. This causes a negative departure of the calculated LMF from the true LMF. Second, the energy balance method assumes complete evaporation and mixing of the two streams before the static mixer outlet. Third, it assumes that the walls of the mixer are adiabatic.

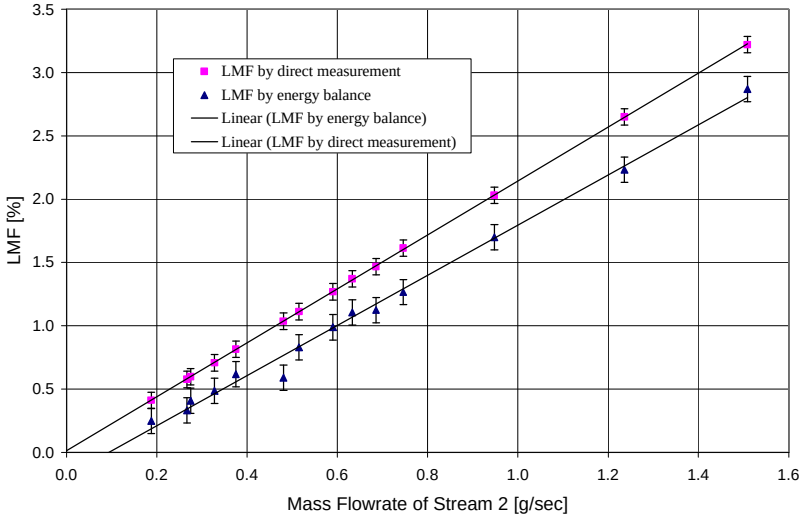

Figure 5-3. Comparison of LMF calculated from (1) *direct measurement method*, and (2) *energy balance method*

Figure 5-3 also provides a calibration for estimating the systematic error in using the *energy balance method* for determining the time-averaged liquid mass fraction. The LMF as a function of $\dot{m}_2$ for both methods can be described by the following two linear relationships

$$LMF_{DIRECT} = 2.145\,\dot{m}_2 \tag{5.4}$$

$$LMF_{ENERGY} = 2.145\,\dot{m}_2 - 0.186 \tag{5.5}$$

Writing these two equations in terms of $\dot{m}_2$ and setting them equal will give the following equation for the actual LMF from the LMF determined by the *energy balance method*

$$LMF = LMF_{DIRECT} = \frac{LMF_{ENERGY} + 0.186}{0.924} \tag{5.6}$$

Eq. (5.6) will be used in section 5.3 to calculate the liquid mass fraction present at the evaporator outlet for the *characterizing evaporator exit flows* experiment.

Now that the systematic error in the *energy balance method* for calculating LMF can be accounted for by using eq. (5.6), it is possible to accurately measure the time averaged LMF present in a multi-channel evaporator system. In section 5.2 the outlet conditions of a multi-channel evaporator fed by either a thermostatic expansion valve, or a manual expansion valve, are studied. For these tests only the main evaporator in Figure 5-1 was used. Consequently, we could only measure the total refrigerant mass flow rate $\dot{m}_r$, which in this case is equal to the mass flow rate of liquid $\dot{m}_{liq}$ plus the mass flow rate of superheated vapor $\dot{m}_{vapor}$ at the evaporator outlet. The total energy lost from the superheated vapor during evaporation of the entrained liquid in the static mixer is

$$Q_{evap} = \dot{m}_{vapor}\left(h_r - h_{mix}\right) \tag{5.7}$$

This is the same as the left hand side of eq. (5.3) with $\dot{m}_r$ replaced with $\dot{m}_{vapor}$. The enthalpy at the exit of the static mixer h_{mix} can easily be found from pressure and temperature measurements, but the superheated vapor enthalpy h_r is a little more complicated because the superheated vapor temperature could not be directly measured by a thermocouple when liquid was present at the evaporator outlet. In order to measure the vapor temperature the thermocouple was shielded from droplet impacts. The experimental technique used to measure the vapor temperature is described in Appendix A. The energy lost by the vapor is equal to the energy gained by the liquid during evaporation and mixing, and can be written as

$$Q_{evap} = \dot{m}_{liq} h_{fg} + \dot{m}_{liq}\left(h_{mix} - h_{sat}\right) \tag{5.8}$$

Eq. (5.7) and eq. (5.8) can be combined to solve for the liquid mass flow rate $\dot{m}_{liq}$, which can then be substituted into eq. (5.1) to solve for LMF. Finally, this LMF is substituted into eq. (5.6), which corrects for the systematic error in the energy balance method.

5.2. Correlating instrument signals to LMF

Experiments were performed to correlate the output signals of a beaded thermocouple, the MEMS resistance sensors, and scattered laser light with the presence of liquid mass fraction. For these experiments, the secondary evaporator was used to inject liquid into the test section while the main evaporator was running at high superheat (ΔT_{sup} = 11.9°C). These tests were conducted to ensure that temperature oscillations of the beaded thermocouple and MEMS sensor were caused by LMF, as opposed to some other phenomenon like evaporator pressure fluctuations.

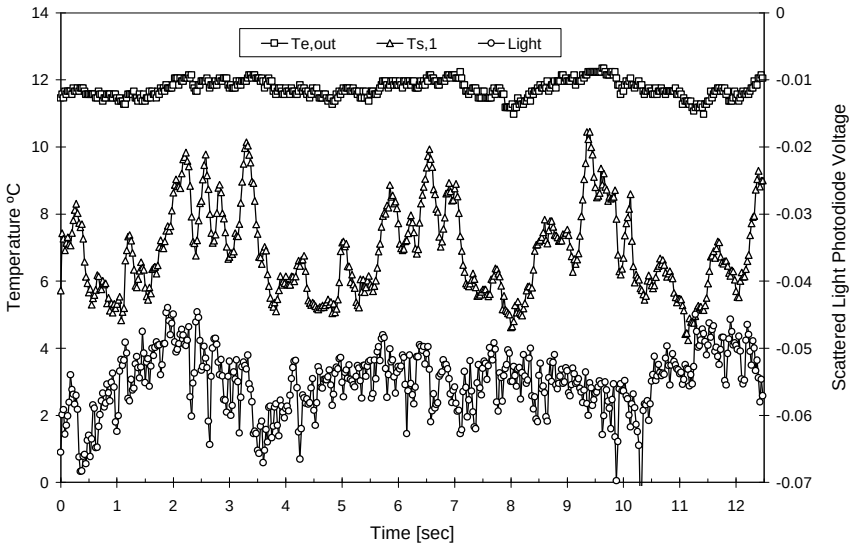

Figure 5-4. Evaporator outlet thermocouple temperature $T_{e,out}$, MEMS sensor temperature $T_{s,1}$, and scattered laser light photodiode voltage in the presence of small quantities of liquid (LMF=0.41%)

For these tests, an exposed beaded thermocouple, the largest MEMS sensor R_1, and the scattered laser light signals were sampled at 40 Hz for 12.5 seconds. The thermocouple was located in the glass tube (see schematic in Figure 5-1) such that the exposed bead was in the center of the pipe cross section. In this way, the thermocouple could be impacted by entrained refrigerant droplets while measuring $T_{e,out}$, the evaporator outlet temperature. Figure 5-4 shows the time traces of these three signals for very small amounts of liquid (LMF = 0.41%) with high superheat, ΔT_{sup} = 11.9°C. The sensor was driven with a 25 mA DC current.

The scattered laser light signal is important, because it directly correlates with the quantity of droplets present in the test section. The photodiode voltage signal decreases as more droplets are present to scatter the beam. Notice that the signal amplitudes of both the thermocouple and the MEMS sensor relate to the scattered light (and thus droplets). There is a slight time lag between the two temperatures and the laser signal of about 1 second. This is because the laser gives an instantaneous measure of the liquid fraction, whereas the thermocouple and sensor have thermal capacitance which delays their response to liquid. Additionally, the laser was located 6 inches upstream of the MEMS sensor, and 14 inches upstream of the thermocouple, so a further time delay can be expected for droplets to travel the distance between the laser and the other instruments.

The MEMS sensor and scattered light signals were also measured with lock-in amplifiers for liquid fractions up to 4%. The lock-in output is based upon the autocorrelation of the input signal to a reference signal. For the scattered light signal, the laser beam chopper frequency was used as the reference signal. The chopper frequency was tuned to 40 Hz, so the lock-in output was proportional only to that portion of the photodiode signal having components at 40 Hz. The MEMS sensor was driven by a square-wave current, also at 40 Hz, with a maximum amplitude of 20 mA supplied by a wave generator. It is important to set the driving current frequency much higher than the sensor time constant, so that the sensor "sees" the oscillating current as if it were constant. Figure 5-5 shows these results. The lock-in output of each signal has been normalized their respective maximal value (at the highest LMF). What this figure indicates quite clearly is the sensitivity of each instrument to the amount of liquid in the test section. The scattered laser light is proportional to LMF, and is usable over a broad range of LMF. The MEMS sensor, however, is extremely sensitive for liquid mass fractions less than 0.7%, and then almost immediately becomes insensitive to additional liquid. The results are encouraging, because the high sensitivity of the MEMS sensor to LMF below 0.7% indicates that the sensor could potentially be very useful in detecting the onset of unstable superheat, such as in cases (1) and (2) in. In Figure 5-4, the smaller thermocouple temperature fluctuations indicate that it is much less sensitive to low LMF than the MEMS sensor. An estimated initial slope of the thermocouple response to LMF has been added to Figure 5-5, showing less sensitivity at low LMF, but an increase in useable range. The MEMS sensor has an added degree of flexibility over a thermocouple, because simply increasing the driving current can extend its useable range.

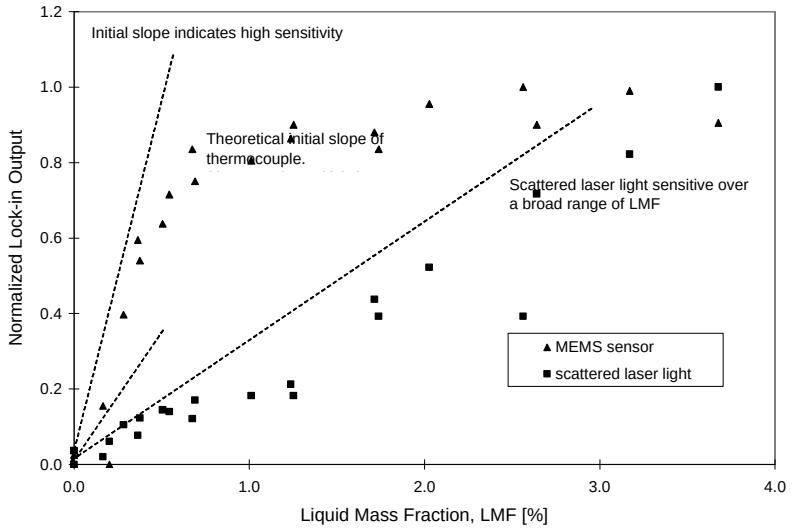

Figure 5-5. Normalized lock-in amplifier output of MEMS sensor and scattered laser light showing sensitivity to droplets

5.3. Characterizing Evaporator Exit Flows

5.3.1. Introduction to experiments

One goal of this study was to characterize the exit conditions of a plate evaporator over a range of superheat temperatures. Normal superheat temperatures are high enough to ensure that no liquid leaves the

evaporator. Reducing exit superheat too much can lead to maldistribution of the refrigerant amongst parallel channels in the evaporator causing entrained liquid droplets to be present in the exit flow. This section describes the results of a series of experiments that were conducted using a 3-ton capacity PHE as an evaporator. Three configurations were tested: 1) PHE fed by a thermostatic expansion valve (TXV), 2) PHE fed by a manual expansion valve (MXV), and 3) a two-evaporator arrangement in which LMF is manually controlled. Case (1) will show the performance of a real evaporator/TXV system, case (2) eliminates the influence of TXV dynamics, and case (3) allows for comparison of instrument signals under controlled LMF conditions.

The graphs in Figure 5-6, Figure 5-7, and Figure 5-8 are representative of the conditions witnessed at the evaporator outlet for the three cases. The figures depict typical evaporator behavior, for each case, as the outlet superheat temperature is reduced. For practical operation, it is always best to operate at the lowest possible superheat that allows only vapor to exit the evaporator. There comes a point where further reductions in superheat, for a given evaporator load, leads to incomplete evaporation within the channels, and entrained liquid appears at the outlet. The liquid mass fraction (LMF) present during each test run, therefore, is a convenient basis for comparing the three cases. Runs with relatively similar LMF, for each case, are grouped together in the figures. Initially, in Figure 5-6, the superheat is relatively high, and not much liquid is present at the evaporator outlet. For the purpose of comparison, this is what will be called *low* LMF. As superheat is reduced in Figure 5-7, and again in Figure 5-8, the amount of entrained liquid increases. These two figures represent *medium* LMF, and *high* LMF, respectively.

Case (3) in Figure 5-6 represents the case of high superheat and almost no liquid at the exit. During this test the main evaporator was operating with enough superheat, $\Delta T_{sup} = 8.6°C$, to ensure that no liquid was present at the outlet, and the secondary evaporator flow was shut off. As expected, the three thermocouples located in the test section, $T_{e,out}$, T_{vapor}, and T_{mix}, all indicate the same temperature. This is because there is no liquid present in the exiting vapor stream. The MEMS sensor temperature, however, is more than 2°C higher than the surrounding vapor. This makes sense since there are no droplets present. The heated sensor will always be hotter than the surrounding vapor unless colder liquid droplets at the saturation temperature, T_{sat}, strike and cool the sensor.

5.3.2. Case (1) - TXV control of a plate evaporator

Case (1) in Figure 5-6, Figure 5-7, and Figure 5-8 shows the exit conditions of the main evaporator fed by a pressure equalized TXV. In each figure the superheat is progressively reduced causing the LMF to increase. Starting with Figure 5-6, the evaporator superheat is relatively stable at 8.9°C, but there is already an indication of liquid at the outlet. Notice that there is a measurable difference between the vapor temperature, T_{vapor}, and the static mixer outlet temperature, T_{mix}. Since the pressure drop in the mixer was negligible, this temperature difference can only be explained by the evaporation of entrained liquid by the surrounding vapor within the mixer. Thus, the magnitude of the temperature difference ($T_{vapor} - T_{mix}$) gives an indication of the relative amount of entrained liquid. The thermocouple located directly at the evaporator outlet, $T_{e,out}$, is also lower than the vapor temperature. This thermocouple was suspended in the middle of the outlet pipe cross section, and could easily be impacted by any liquid droplets that might be present in the flow stream. The fact that $T_{e,out}$ is lower than T_{vapor} is another indication that liquid droplets were present during this run, because the droplets, at temperature T_{sat}, strike and cool the thermocouple below the temperature of the surrounding vapor. In Figure 5-7 the superheat setpoint is reduced by

only a few tenths of a degree, but the measured LMF almost doubles, and the evaporator outlet temperature, $T_{e,out}$, begins to fluctuate by more than 2°C. This condition can be seen in Figure 5-7. Consider for a moment graph (a) for this case, which shows the outlet temperatures during the entire test run. The $T_{e,out}$ temperature oscillations seem to be superimposed over a longer time scale fluctuation on the order of 3 minutes. This slow periodic fluctuation could be a consequence of the TXV responding to the high superheat in the outlet pipe by gradually opening, and increasing the refrigerant flow to the evaporator. The difference between case (1) and case (2) in Figure 5-8 indicates the temperature sensing bulb strapped to the outside of the outlet pipe can not react fast enough to the liquid rapidly emerging at the outlet, and the valve opening eventually decreases to reduce refrigerant flow to the evaporator, and increase superheat.

It is interesting to examine the behavior of the evaporator outlet thermocouple temperature, $T_{e,out}$, and the MEMS sensor temperature, $T_{s,1}$, at high sampling rates. Graphs (b) show these temperatures sampled at 40 Hz. These data were taken immediately after the slow speed data in graph (a) had been collected. At low LMF (Figure 5-6) $T_{e,out}$ and $T_{s,1}$ appear constant, but as LMF increases there appears to be a definite temperature oscillation with a period nearly equal to 7 seconds. This is supported by graphs (a) and (b) at medium LMF (Figure 5-7), and high LMF (Figure 5-8). The pattern of the MEMS sensor temperature is similar to a sawtooth curve. The sawtooth pattern is a result of liquid impacting the sensor in bursts, or clouds. Initially, a quantity of liquid strikes and rapidly cools the sensor. Then the internal heat generation of the sensor causes the temperature to rise slowly, until the next burst of liquid appears 7 seconds later. This is, of course, an simplified view of the process. Any amount of liquid occurring in between these droplet clouds will disturb the rise of the sensor temperature, and this can be seen in graph (b) of Figure 5-8. Notice how the sawtooth pattern of $T_{s,1}$ is quite jagged, which is most likely due to smaller bunches of droplets distributed between the larger clouds that come every 7 seconds. It is important to mention that the temperature oscillations of both the thermocouple, $T_{e,out}$, and the sensor, $T_{s,1}$, correlate identically to clouds of liquid that were large enough to be seen by the naked eye through the glass tube in the test section.

5.3.3. Case (2) - MXV control of a plate evaporator

Case (2) is similar to case (1), except that this time a manual expansion valve was used instead of the TXV. The results of case (2) are presented in Figure 5-6, Figure 5-7, and Figure 5-8 in order of increasing LMF. The purpose of the manual expansion valve was to study the outlet conditions of a multi-channel evaporator as superheat is reduced, without the effects of TXV valve dynamics. By using a MXV, any phenomena witnessed at the evaporator outlet will only be a consequence of the physical mechanisms of evaporation among the parallel channels. For all case (2) test runs the valve position was fixed, and the system was allowed to come to a pseudo-steady condition. What this means is that the amplitude of the temperature oscillations of $T_{e,out}$ and $T_{s,1}$ remained fairly constant, and T_{vapor}, T_{mix}, and T_{sat} remained constant over the entire run. The most important comparison between the TXV and MXV runs is that the sawtooth pattern of the MEMS sensor temperature occurs in both cases. Again, the period of these temperature oscillations is on the order of 7 seconds. It can be inferred from the MXV runs that entrained liquid, probably resulting from maldistribution between evaporator channels, emerges at the outlet piping in organized clouds every 7 seconds. This is a significant finding, because it indicates that mists of entrained liquid droplets will appear at regular and predictable intervals as a result of maldistribution within a multi-

channel evaporator. Furthermore, it seems that this regular pattern remains constant even with increasing amounts of maldistribution, or measured liquid mass fraction.

5.3.4. Case (3) – Controlled LMF with a two-evaporator arrangement

Case (3) in Figure 5-6, Figure 5-7, and Figure 5-8 show what can occur at the evaporator outlet when there is maldistribution between two parallel channels. The two-evaporator arrangement, shown schematically in Figure 5-1, was adjusted such that the 3-ton main evaporator was running with high superheat at the outlet, to ensure no droplets, and the smaller secondary evaporator added a low quality mixture into the test section. Manual expansion valves that were left at a fixed position during the test runs fed both evaporators. This simulated a two-channel evaporator in which maldistribution can be manually adjusted between the channels. It should be noted that the test runs shown for case (3) in the figures were selected such that the average LMF, and superheat during the run closely matched those of case (1) and (2) for comparison. Specifically, the low LMF data is from run 19, the medium LMF data is from run 11, and the high LMF data is from run 20 in Appendix B.

The first thing to notice between cases (1), (2), and (3) is the similarity of the thermocouple time traces sampled at low speed (0.5 Hz), shown in graphs (a) in the figures. As LMF increases, the magnitude of the evaporator outlet temperature fluctuations, $T_{e,out}$, continues to increase. In Figure 5-7 and Figure 5-8, these fluctuations are about the same amplitude for the TXV control, MXV control, and controlled LMF tests. The time scale of the $T_{e,out}$ temperature fluctuations also seems to be relatively constant between the three cases. There is one noticeable difference between case (3), and the behavior of a real evaporator in cases (1) and (2). When LMF is added via the secondary evaporator, the evaporator outlet temperature, $T_{e,out}$, is as much as 2°C lower than was measured during the TXV and MXV tests. One possible explanation for this might be that there was more entrained liquid present during the case (3) tests, but examination of the high speed (40 Hz) data in graph (b) tells us something different. Suppose that instead of the entrained liquid coming in discrete mists every 7 seconds, the droplets are more evenly distributed. If this were true, the time trace of the MEMS sensor temperature, $T_{s,1}$, would not appear as a regular sawtooth pattern, but would appear more random due to smaller droplet mists impinging on the sensor more frequently. This is exactly what case (3) in Figure 5-7 and Figure 5-8 indicates. The sensor and the exposed thermocouple are cooled more frequently by droplet mists, and are prevented from warming back up to the superheated vapor temperature.

Also notice that the $T_{e,out}$ and $T_{s,1}$ temperature fluctuations, on a slower scale, directly correlate with the saturation temperature fluctuations. It seems that there are higher frequency temperature oscillations, due to frequent cooling by droplet mists, superimposed over a slower average temperature change related to the saturation temperature. The frequency spectra in graphs (c) tell this story, perhaps a little more clearly. Consider the frequency spectrum for the three cases in Figure 5-8. A large spike at 0.16 Hz in all three cases dominates the thermocouple and MEMS sensor signals. In other words, the signals have a characteristic period of 6.25 seconds. Recall that the temperature-time data indicated that temperature oscillations had a period of about 7 seconds, and that these oscillations coincided with droplet clouds witnessed in the glass tube. The TXV control, and MXV control cases only have significant frequencies below 2 Hz, but the thermocouple and MEMS sensor signals contain higher frequencies during the controlled LMF tests. These frequencies above 2 Hz indicate that indeed the

distribution of droplets was more uniform in case (3) than in case (1) or (2), which are dominated by discrete droplet clouds at 7 second intervals.

5.3.5. Performance of the MEMS sensor

Although the performance of the sensor will be discussed in greater detail in section 5.5 and 5.6, it is interesting to notice in Figure 5-6, Figure 5-7, and Figure 5-8 that the MEMS sensor is consistently more sensitive to LMF than the exposed beaded thermocouple. This is encouraging, because with a first prototype sensor we have a working device that is simple, yet gives us enough information to measure LMF in a multi-channel evaporator.

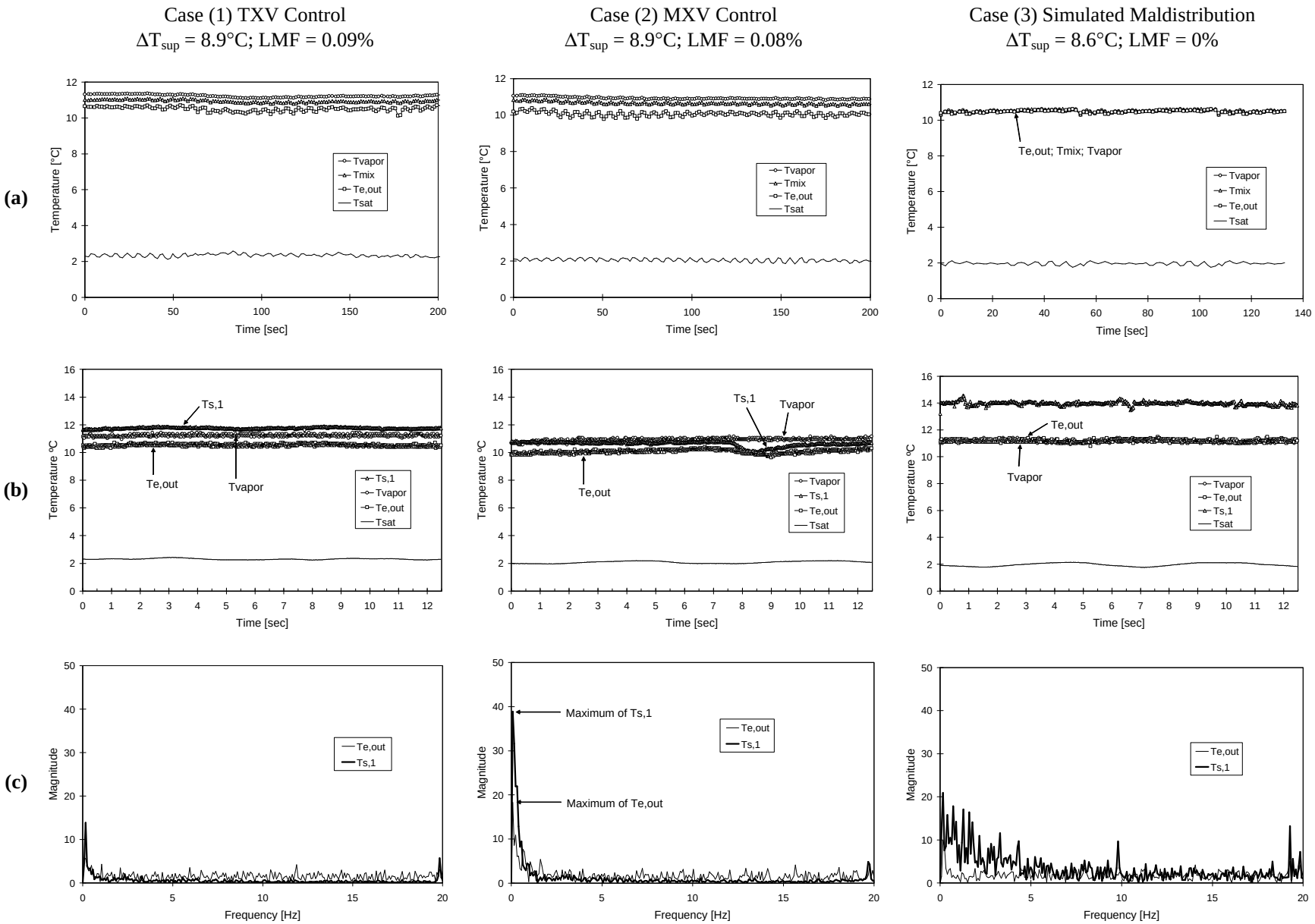

Figure 5-6. Evaporator outlet temperature signal comparison at low LMF during TXV control, MXV control, and simulated maldistribution (a) during the entire run, (b) at 40Hz sampling rate, and (c) in the frequency domain

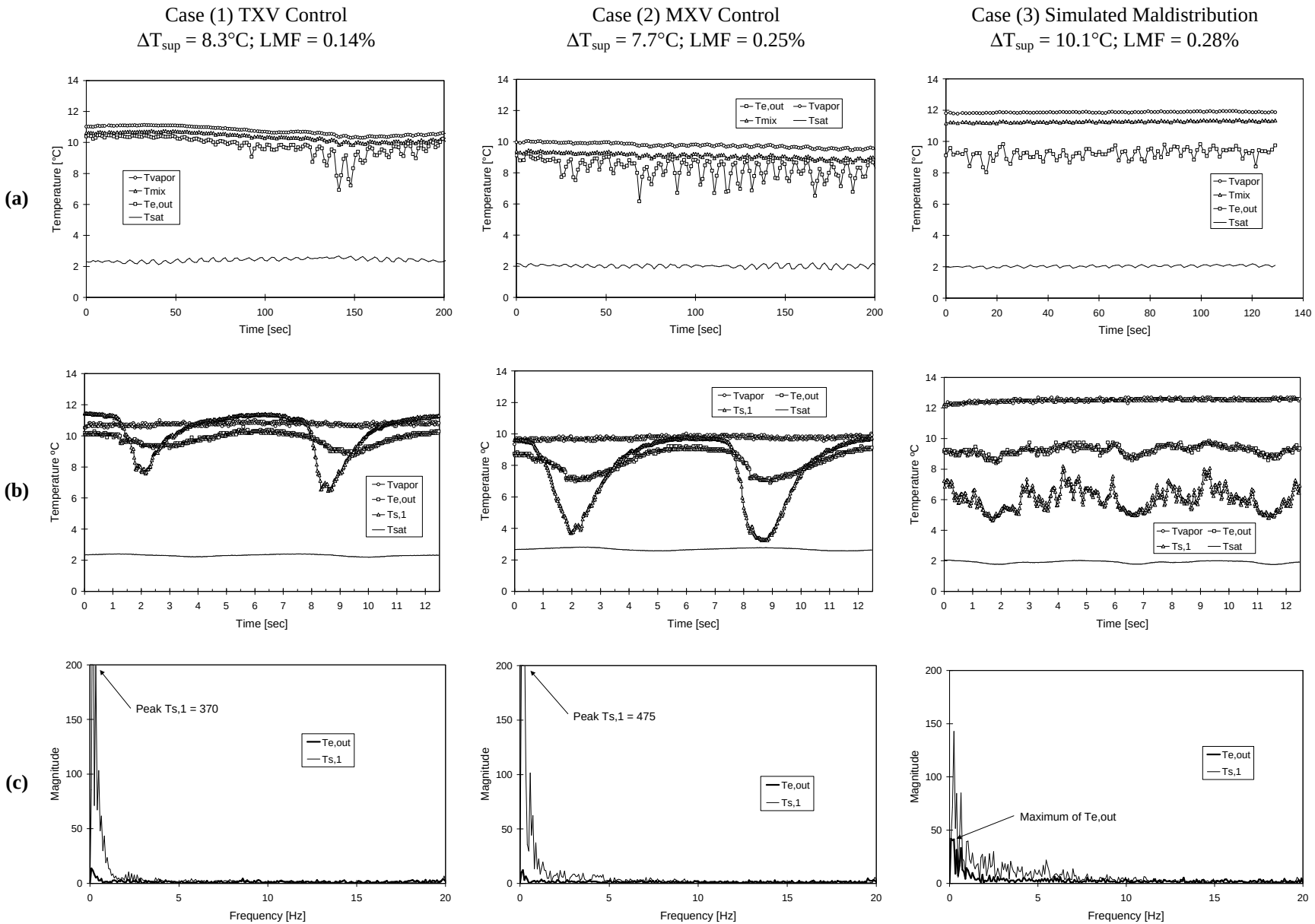

Figure 5-7. Evaporator outlet temperature signal comparison at medium LMF during TXV control, MXV control, and simulated maldistribution (a) during the entire run, (b) at 40Hz sampling rate, and (c) in the frequency domain

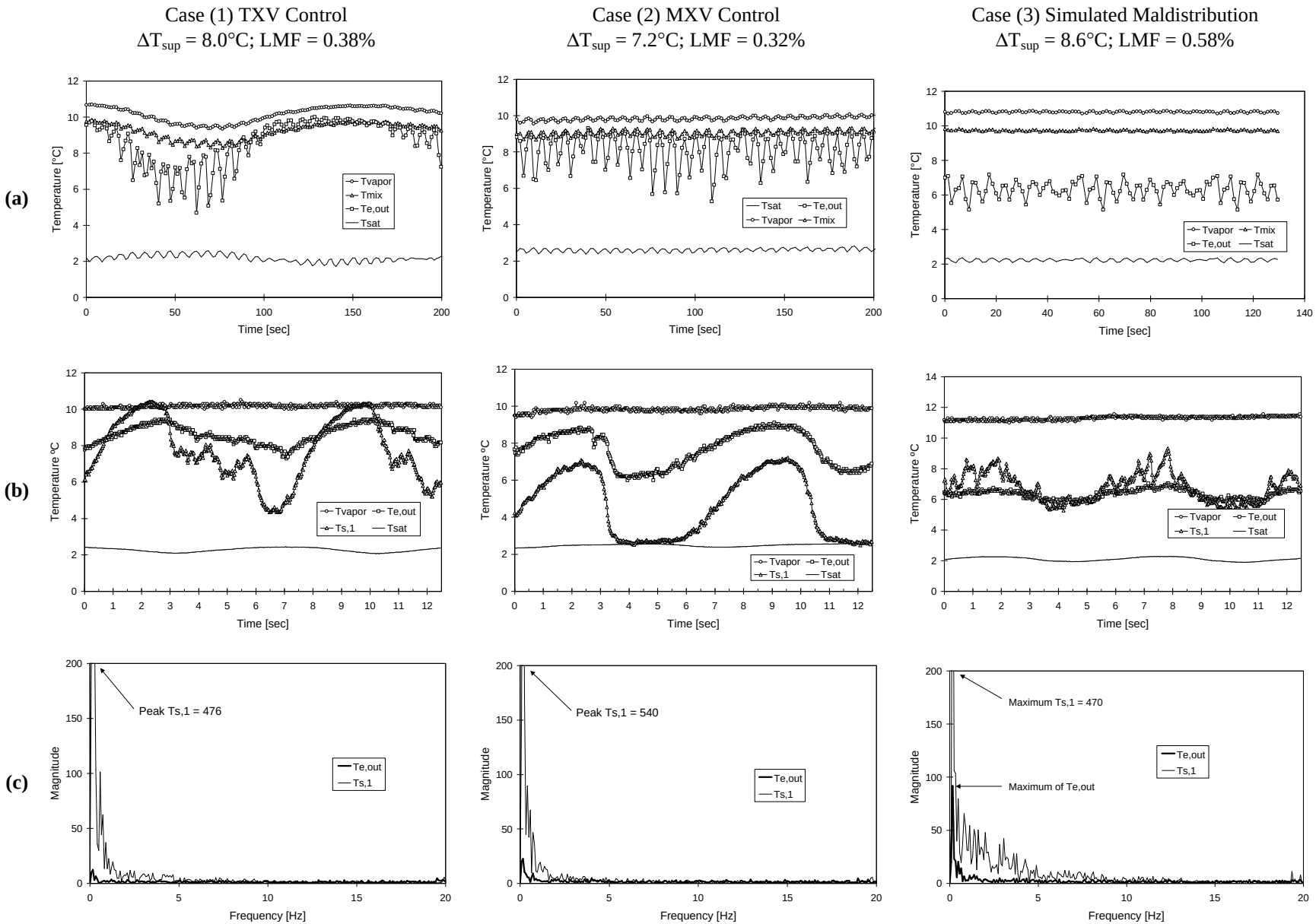

Figure 5-8. Evaporator outlet temperature signal comparison at high LMF during TXV control, MXV control, and simulated maldistribution (a) during the entire run, (b) at 40Hz sampling rate, and (c) in the frequency domain

5.4. Comparison of thermocouple and MEMS sensor signals

5.4.1. Introduction to experiments

The response of a beaded thermocouple and three MEMS sensors were formally compared in the time and frequency domains, at various superheats and LMF, in order to determine their potential feasibility for controlling plate evaporators. These tests were conducted using the secondary evaporator to inject controlled amounts of LMF into the test section. The main evaporator was operated in the superheated range with a mass flow rate of 40 g/s nominally. In total, 25 separate runs were conducted over 3 different superheats (12°C, 10°C, and 8.5°C), and LMF from 0 to 3.5%. A summary of each run, including time histories and frequency spectra of test section temperatures can be found in Appendix B. Data collected during each run consisted of

1. Global system parameters
   These measurements included flow rates, pressures, and temperatures necessary for energy balance calculations. The data was collected at 0.5 Hz for 200 seconds.
2. Fast sampling of test section instrumentation
   The raw scattered light photodiode voltage, evaporator pressure, MEMS sensor voltages, and all test section thermocouples were recorded at 40 Hz for 12.5 seconds.

A sampling frequency of 40 Hz was selected because it provided the best opportunity to capture all significant frequencies present in the thermocouple, MEMS sensor, and scattered light signals. During the facility shake-down process, Fourier analysis of the raw output of each instrument (thermocouple, MEMS sensors, and scattered light) revealed that any frequencies above 10 Hz did not make a significant contribution to the frequency spectra. Therefore, the sampling rate was selected as close as possible to the maximum expected frequency, while still being above twice the Nyquist frequency. The Fourier analysis was performed on a 4-channel digital oscilloscope capable of detecting frequencies to the GHz range.

The graphs in Figure 5-9 highlight the behavior of the test section temperatures, over three different superheats, as LMF was incresed. These graphs show the superheat temperature ($\Delta T_{sup} = T_{vapor} - T_{sat}$), the temperature of the thermocouple located in the glass tube, $T_{e,out}$, and the largest sensor temperature, $T_{s,1}$, all as a function of LMF. A nice feature of the graphs is that they clearly indicate the sensitivity of the thermocouple and MEMS sensor to increasing amounts of liquid. The bars on the thermocouple and sensor temperatures indicate the range of temperatures measured during the entire 12.5 seconds of data collection time. The larger the error bars, the more sensitive the instrument is to the presence of liquid droplets. In all three graphs the MEMS sensor is most sensitive at LMF's below 1%, which is exactly what the lock-in data (see section 5.2) revealed during the early stages of experimentation. The thermocouple, however, is sensitive at higher LMF around 1.25%.

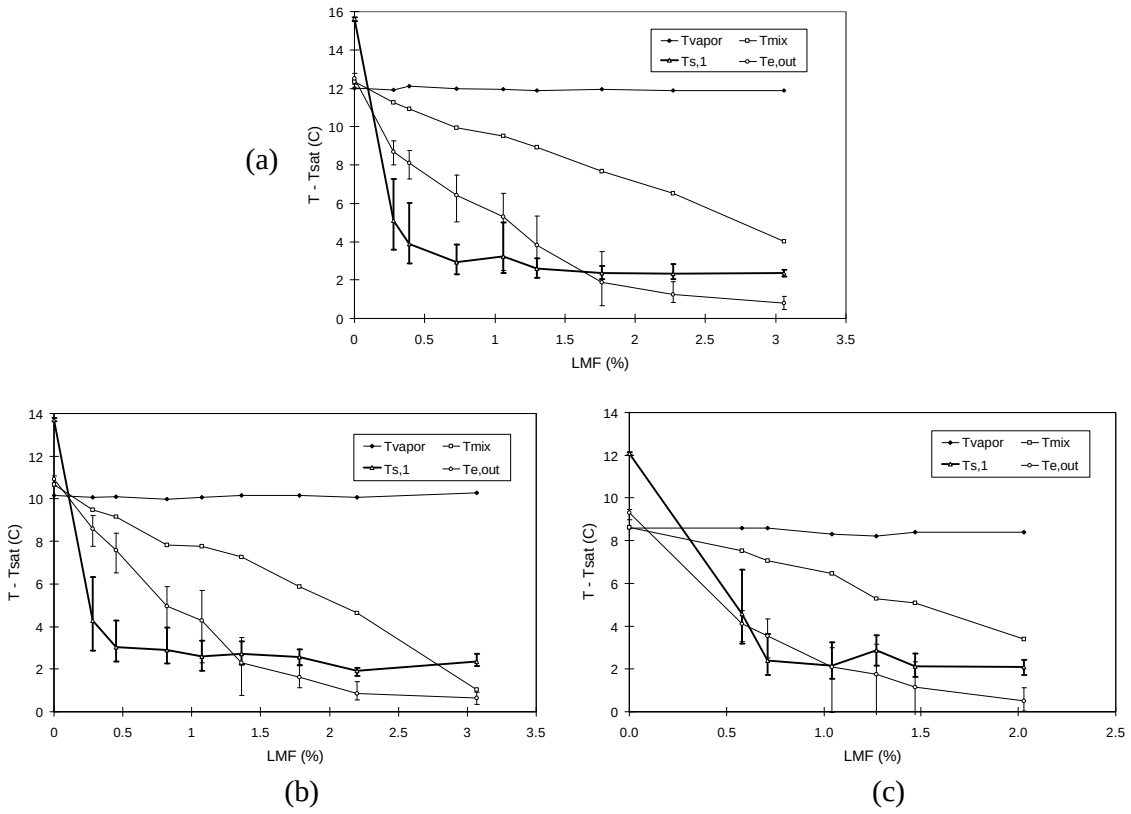

Figure 5-9. (T - T_{sat}) vs. liquid mass fraction behavior of thermocouples (T_{mix}, $T_{e,out}$, T_{vapor}), and MEMS sensor temperature ($T_{s,1}$) at three superheats 12°C (a), 10°C (b), and 8.6°C (c)

Another interesting feature of the graphs is that the heated sensor temperature is often lower than the thermocouple. At first this seems counterintuitive. One would think that a heated resistor would always be hotter than a thermocouple simply because the self-heating would promote evaporation of liquid droplets. A possible explanation for the lower sensor temperature could be that the sensor surface was covered completely by a thin film of liquid (or possibly oil). If this were the case, then the thin liquid film would boil on the surface of the sensor. The sensor temperature would be driven down very close to the saturation temperature of the liquid, because only a slight excess temperature is required for boiling. In all three graphs, the excess sensor temperature rapidly approaches $T_{s,1}$ - T_{sat} = 2°C. In addition, the surface area to mass ratio of the sensor is much larger than the thermocouple, so a droplet has a greater cooling effect on the MEMS sensor than the thermocouple. Therefore, the sensor temperature is lower than the thermocouple when sufficient droplets are present.

5.4.2. Time domain analysis

Other comparisons between the beaded thermocouple and the MEMS sensors can be made from Figure 5-10. This figure shows the thermocouple temperature, MEMS sensor temperature (for the largest sensor, R_1), saturation temperature, and scattered laser light photodiode voltage in the time domain at low liquid mass fraction (LMF = 0.28%), and high liquid mass fraction (LMF = 1.76%). At low LMF, the MEMS sensor is most sensitive to the presence of droplets. This is evident by the large amplitude temperature fluctuations of the sensor, compared to

relatively little temperature fluctuation by the thermocouple. When large amounts of liquid are present the MEMS sensor is unable to detect the increasing amount of liquid, but the thermocouple now is becoming more sensitive to liquid. At the higher LMF, the temperature fluctuations of the thermocouple increase, and those of the MEMS sensor decrease.

It is important to notice that there are both slow and fast frequency components in the thermocouple and the MEMS sensor temperature traces. The slow frequency component in both temperatures is exactly in phase with the saturation temperature displayed on the bottom of the figures. Saturation temperature varies with evaporation pressure, which oscillates due to the nature of the two-phase evaporating flow in the evaporator. Superimposed on top of the slow fluctuation is the high frequency content. It is the high frequency oscillation that is a result of droplets impinging on the surface of the sensor (and thermocouple).

The trace of the scattered laser light photodiode voltage in both figures gives a relative indication of the amount of liquid present during the run. When LMF is only 0.28%, the scattered light signal amplitude fluctuation is about 0.01 Volts, but when LMF = 1.76%, amplitude variation is slightly higher. There are also several large amplitude spikes on the order of 0.5 Volts. These larger spikes are related to large clouds of droplets that were visually observed through the glass tube mounted in the test section. Notice that during high LMF the thermocouple temperature drops rapidly after the passage of a droplet cloud, but the MEMS sensor is unable to respond to the additional liquid.

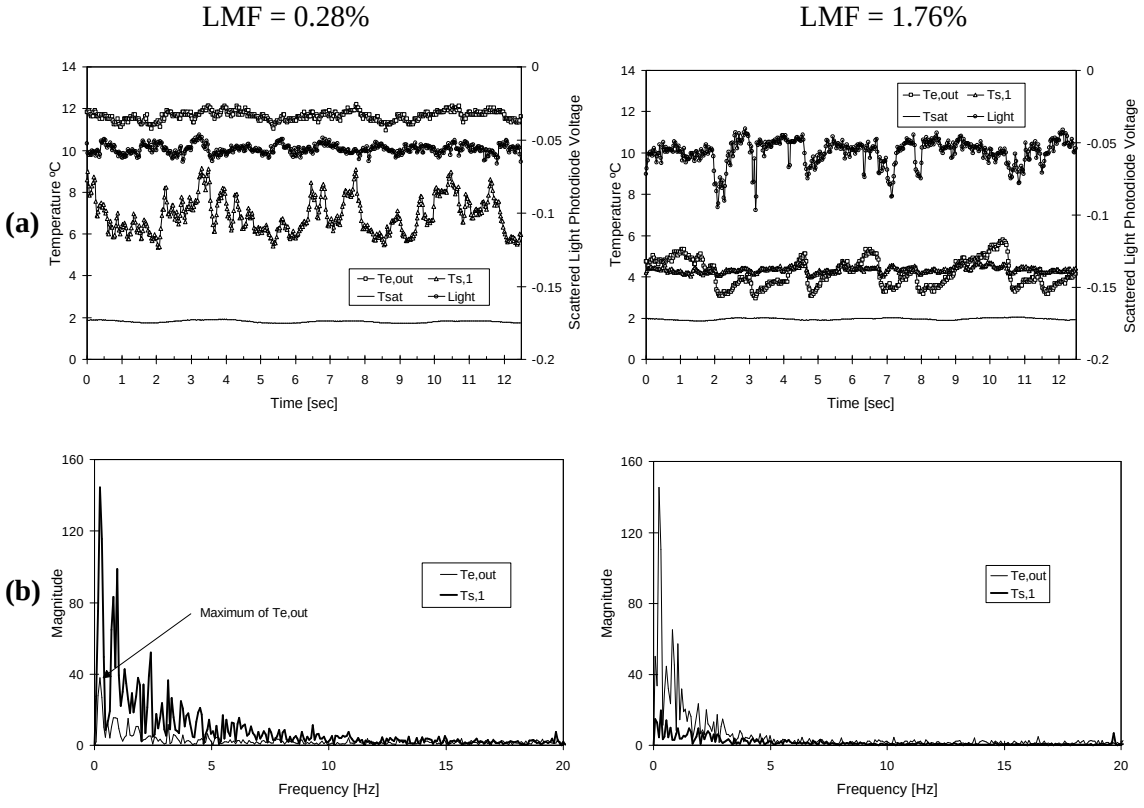

Figure 5-10 Thermocouple ($T_{e,out}$), MEMS sensor ($T_{s,1}$), and scattered laser light signals in the time domain (a), and frequency domain (b), for LMF = 0.28% (left), and LMF = 1.76% (right)

5.4.3. Frequency domain analysis

Additional information about the performance of the thermocouple and MEMS sensor can be obtained by examining the frequency content of the signals. The power spectra of both signals is shown in graphs (b) Figure 5-10 for both low and high LMF. Fast Fourier Transform analysis was performed on the discrete temperature signals using the HP-VEE™ software, by first subtracting the mean of each signal from the original data set. This was done to remove the DC component of the each signal, thereby leaving only the oscillating portion of the temperature caused by both impingement of liquid droplets, and saturation temperature fluctuation. The first large spike at 0.16 Hz in both figures is due to the saturation temperature fluctuation. All of the other frequencies can be attributed to the presence of liquid droplets. In both figures, the significant frequencies die out around 5 Hz. Initially, it was thought that the MEMS sensor would be able to detect individual droplet impacts at frequencies above 100 Hz. This is clearly not the case, especially at the higher LMF's when droplet clouds are observed visually in the glass tube.

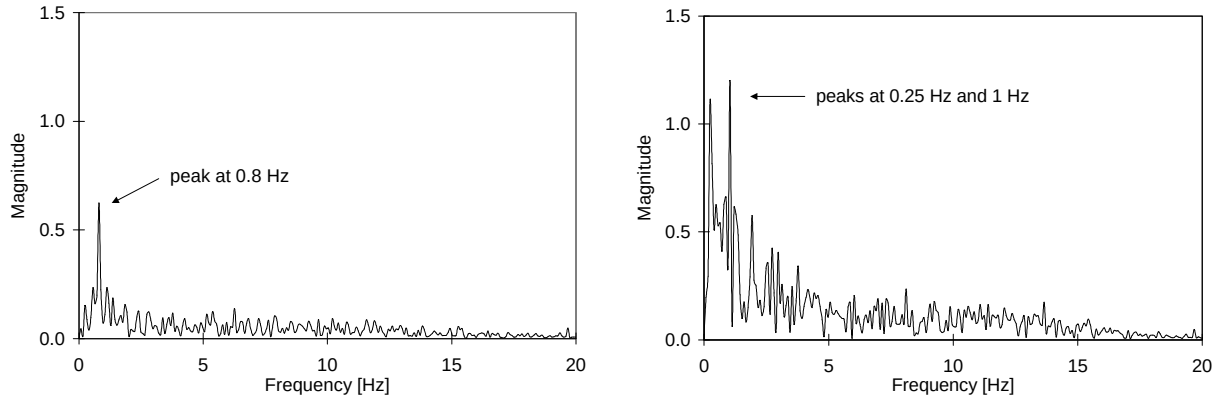

Figure 5-11. Frequency spectra of the scattered laser light signal at low LMF (a), and high LMF (b). (low LMF = 0.28%, high LMF = 1.76%)

Even the scattered laser light can not detect the passing of individual droplets. The power spectra of the scattered laser light photodiode voltage are shown in Figure 5-11, for LMF = 0.28% and 1.76%. At higher LMF there is clearly a stronger signal, indicating more scattering due to liquid droplets. There are more sophisticated techniques for measuring droplet size, velocity, and distribution, such as phase/Doppler particle analysis (P/DPA) and laser-Doppler velocimetry (LDV). These laser diagnostics techniques have seen widespread use in combustion research and aerosol sprays. They require very expensive laser equipment that is extremely difficult to calibrate, which is why those techniques were not used in this investigation.

5.4.4. Effect of MEMS sensor surface area on sensitivity to droplets

Entrained liquid droplets smaller than 50 μm in diameter traveling at 10 m/s have been measured in horizontal tube evaporators [2]. It was suspected that the size of the sensor would directly affect its ability to detect such small droplets in the flow stream. For example, if a droplet is large enough to completely coat the small sensor upon impact, it is sure to drop the sensor temperature very close to the liquid temperature. However, the same droplet impacting the large sensor would only cover about 7% of the total surface area, and could not bring possibly lower the sensor temperature completely to the liquid temperature. If the sensors are indeed sensitive enough to be

affected individual droplets, then the larger sensor should prove less sensitive at lower LMF's than the smallest sensor. By placing three MEMS sensors of varying size on the same substrate, a direct comparison of the size effects can be made at identical flow conditions.

Figure 5-12 shows a comparison of the normalized frequency spectra of the time-varying voltage signal from each sensor during conditions of high superheat, ΔT_{sup} = 10°C, and low liquid fraction, LMF = 0.32%. These conditions allow a good comparison between the three sensors because they are most sensitive at lower liquid mass fractions. Clearly, the frequency content of each sensor is almost identical. In some ways this is encouraging because it tells designers that an extremely small sensor requiring a minimum of current can detect the dynamics of the evaporator exit flow, however, it casts some doubt on the sensor's ability to detect individual droplets. If the distribution of droplets through the pipe cross section can be assumed to be uniform, then the larger sensor should naturally be impacted by more droplets than a smaller sensor. The sensors were designed to have the same heat flux per unit area, so a higher impact frequency was expected from the largest sensor. The data does not show a higher impact frequency associated with increased sensor surface area.

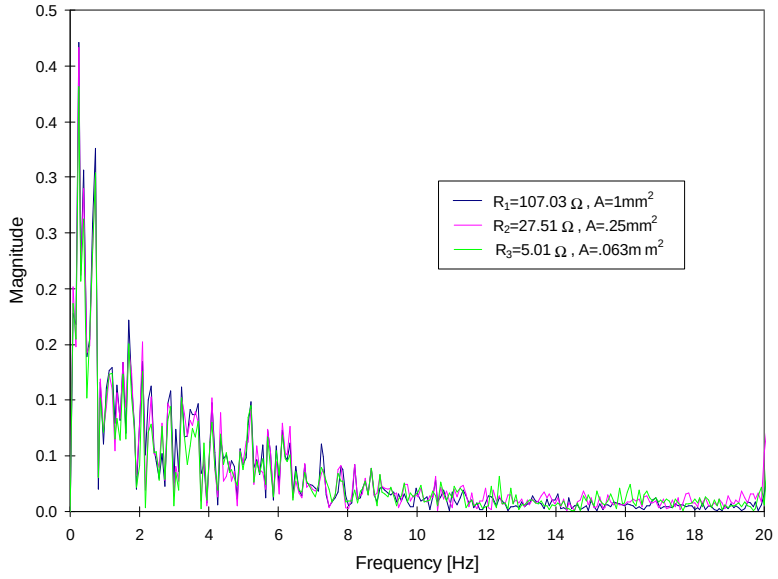

Figure 5-12. Effect of MEMS sensor surface area on signal frequency content for run 10; superheat = 10.0°C; LMF = 0.32%

Chapter 6: Conclusions and Recommendations

6.1. Conclusions

The outlet flow of a 15 kW plate evaporator fed by a TXV was studied over a range of superheats from 12°C to 7°C, in order to investigate how decreasing superheat affects droplet generation at the evaporator exit. It was discovered that entrained refrigerant droplets appeared in the exiting superheated vapor stream at superheat temperatures as high as 9°C. The liquid droplets seemed to come in discrete mists, or clouds, at regular intervals. These droplet mists caused fluctuations in the thermocouple and MEMS sensor signals that resembled a sawtooth pattern with a period of about 7 seconds. The presence of these droplet mists was also confirmed by measurements of scattered laser light intensity, and by visual inspection through the glass tube in the test section.

Reducing superheat below 8°C caused the thermostatic expansion valve to go unstable, otherwise known as hunting. At the onset of unstable operation, the time-averaged LMF of entrained refrigerant droplets was measured to be 0.4%. Droplet mist generation still occurred every 7 seconds during TXV hunting, but the characteristic sawtooth temperature signal was superimposed over a slower mean temperature fluctuation with a period of nearly 3 minutes.

We have successfully fabricated and tested a prototype MEMS thin-film resistance sensor that can detect entrained liquid droplets in a superheated vapor stream. Performance of the sensor was investigated over a range of liquid mass fraction up to 4%, and superheat temperatures from 8°C to 12°C. Data collected over these conditions indicates that the sensor is best used when liquid fractions are below 1%. Greater amounts of liquid tend to saturate the sensor, and prevent it from boiling off the excess liquid. The ability of the MEMS sensor to detect a small entrained LMF was compared to that of an exposed beaded thermocouple, with encouraging results. Although the thermocouple can indicate the presence of droplets over a wider range of LMF, the heated MEMS sensor has a much greater sensitivity than the thermocouple. Experiments using a plate evaporator with TXV control revealed that by the time TXV operation goes unstable, entrained liquid mass fractions are typically 0.4%. The sensor is most sensitive from 0 to 1% LMF, and would therefore be a more attractive choice than a thermocouple for detecting entrained liquid as superheat is reduced.

The case of maldistribution between two parallel evaporator channels was investigated to see if outlet conditions would be similar to those seen in the 19 channel plate evaporator. A two-evaporator arrangement was used to simulate having a plate evaporator with only two refrigerant passes. Maldistribution was created between the two evaporators by running one evaporator (the 15 kW main evaporator) at high superheat, and running the other (secondary evaporator) with quality at the outlet. These tests did not result in discrete droplet mist generation. The droplet distribution appeared to be more uniform in time. This was reflected in both the temperature histories and frequency spectra of the thermocouple and MEMS sensor signals. Picking a representative test run, say LMF = 0.58%, shows that there are significant frequencies in the MEMS sensor signal up to 6 Hz for the case of simulated maldistribution, compared to significant frequencies only up to 2 Hz for the multi-channel evaporator with TXV control. The higher frequencies experienced during simulated maldistribution tests is indicative of more frequent

droplet impacts on the sensor. The more frequently the sensor is impacted by droplets, then the more the droplet mist will appear uniformly distributed in time.

Some remarks must also be made about the sensor design itself. Actually, three MEMS thin-film resistance sensors of different size were made in the same silicon wafer. The sensors ranged from 0.0625 mm^2 to 1 mm^2 in total surface area, and were designed to have equal heat flux. The best way to compare their performance is by their frequency spectra. It has been shown that the frequency content of each sensor is nearly identical, indicating that even the smallest sensor could be used to detect maldistribution in plate evaporators. This is especially encouraging because it implies that a very small device could be manufactured, and even ganged together with several other sensors, to measure the outlet conditions of each channel in a plate evaporator.

6.2. Recommendations

Probably the most successful outcome of this project is the production of a prototype MEMS thin-film resistance sensor that can detect entrained liquid droplets in a superheated vapor stream. Results from this study show that the sensor has the potential to detect the liquid mists entrained in the superheated vapor exiting plate evaporators. A logical course of action would be to use the sensor to develop actuation and control strategies for multi-valve operation. The experimental facility is already equipped with two parallel evaporators, and it would not be too difficult to install normal scale expansion valves and actuators that can be linked through control circuitry to the sensor. Although the ultimate goal of this project is to match newly developed MEMS sensors with microfabricated valves, actuators, and control circuitry, it would first be useful to validate the concept of multi-valve control with normal scale components. If multi-valve operation on a macro scale can control refrigerant distribution in plate evaporators in a way that reduces superheat, which it surely can, then the focus should naturally shift towards developing and incorporating microtechnology into refrigeration systems.

We recognize the fact that the simulated maldistribution tests employed two evaporators, which does not exactly replicate the process of refrigerant distribution at the inlet of a real plate evaporator fed by a TXV. A more realistic approach would be to use a single expansion valve and a plate evaporator with only 2 refrigerant channels. Maldistribution could be induced in the evaporator by unevenly heating one side with an external tape heater. However, the tests that were performed with the two-evaporator arrangement give some insight into the type of outlet conditions that one could expect from a multi-channel evaporator operating with multi-valve control.

REFERENCES

[1] *CRC Handbook of Chemistry and Physics*, Cleveland, OH: CRC Press, 58th ed. (1977).

[2] Barnhart, J.S. and J.E. Peters, "An experimental investigation of flow patterns in a horizontal-tube evaporator," ACRC TR-28, Air Conditioning and Refrigeration Center, University of Illinois at Urbana-Champaign, (1992).

[3] Shannon, M.A., T.M. Leicht, P.S. Hrnjak, N.R. Miller, and F.A. Khan, "Thin-film resistance sensor for measuring liquid mass fraction in super-heated refrigerant," *International Journal of Sensors and Actuators*, 164-177, (2001).

[4] Hewlett-Packard Company, HP E1326B/E1411B 5 ½-Digit Multimeter User's Manual, (1996).

[5] Bruun, H.H., Hot Wire Anemometry: Principles and Signal Analysis, Oxford: New York, (1995).

[6] Moffat, R.J., "Describing the uncertainties in experimental results," *Experimental Thermal and Fluid Science*, v.1, 3-17, (1988).

[7] Martz, W.L., C.M. Burton, and A.J. Jacobi, "Vapor-liquid equilibria for R-22, R-134a, R-125, and R-32/125 with a polyol ester lubricant: measurements and departure from ideality," *ASHRAE Transactions*, v.102, 367-374, (1996).

Appendix A. Calibrating the Thermocouple in the Glass Tube to Measure Vapor Temperature

In order to calculate the liquid mass fraction present at the evaporator outlet using the energy balance method described in section 5.1, it is necessary to know the vapor enthalpy, state **4** in Figure 5.2. The vapor enthalpy is found using thermodynamic property relations with the evaporator outlet pressure and the vapor temperature. In a real system, refrigerant side maldistribution results in a non-equilibrium mixture of entrained liquid within a superheated vapor, making it difficult to determine the vapor temperature with a high degree of certainty. A thermocouple inserted directly into the outlet pipe would be impacted by liquid droplets, causing the thermocouple to indicate a temperature somewhere between the actual vapor temperature, T_{vapor}, and the liquid saturation temperature. It was hypothesized that shielding the thermocouple from impacting droplets, while still exposing it to the exiting vapor, could give a reasonably accurate measure of the superheated vapor temperature.

Referring to the schematic of the evaporators and test section, Figure 5.1, there are three thermocouples downstream of the main evaporator. They are located at the main evaporator outlet, the glass tube, and the static mixer outlet. The thermocouple in the glass tube was used to measure the actual vapor temperature, T_{vapor}, during the test runs of case (1) and (2) in section 5.2. To do so, it was positioned such that the thermocouple bead was in the recessed part of the glass tee, and out of direct contact from droplet impacts. Placing the thermocouple bead in the relatively stagnant gas volume, instead of directly in the vapor flow, does introduce some error which was calibrated in a simple experiment. In order to quantify this error, the system was run until a high degree of superheat (ΔT_{sup} = 10.5°C) remained stable with no indication of droplets. The thermocouple in the glass tee was initially sheltered from the approaching vapor flow, and was then placed in the center of the pipe cross section in direct contact with the approaching vapor flow. The temperature of the glass tube thermocouple, T_{glass}, and the static mixer outlet thermocouple, T_{mix}, were recorded for 100 seconds while the glass thermocouple position was adjusted, and the resulting time traces are shown in Figure A-1. The figure indicates that when the thermocouple is sheltered from the approaching flow, T_{glass} will read 1.1°C higher than the true vapor temperature, T_{mix}, and when the thermocouple is placed at the center of the pipe cross section, T_{glass} and T_{mix} are in agreement to within 0.1°C. For all of the test conditions reported in section 5.2, the T_{glass} thermocouple was placed in the sheltered position so that the vapor temperature could be measured, and the resulting temperature was corrected by 1.1°C to account for the thermocouple position.

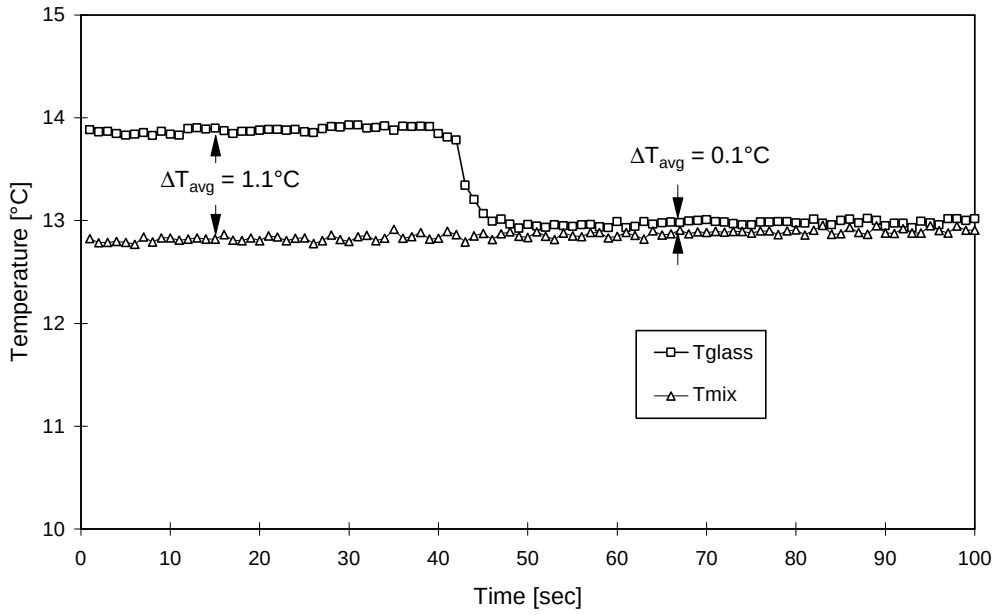

Figure A-1. Calibration of the thermocouple in the glass tube to measure vapor temperature

Appendix B. Procedures for Refrigeration System Startup

Power ON Sequence

1. turn on desktop PC
2. turn on HP Mainframe
3. turn on DC power supply
4. turn on power strip mounted on the wall

DAQ Software Instructions

1. run **HP Vee** from shortcut on the desktop
2. open file " C:\HP VeePrograms\JulyDAQ"
3. press the RUN arrow to begin data sampling
4. data collection procedures:
   a) run Microsoft Excel and open file "C:\MSOffice\Templates\hpveetemplate"
   b) enter number of data points desired in IF/THEN/ELSE box on the JulyDAQ screen (sampling rate is about 1.5 Hz)
   c) make sure the "To Excel" block will write the correct number of data points (ie: rows and columns) to the Excel spreadsheet
   d) click on Collect Data checkbox to begin data collection
   e) DO NOT interrupt DAQ software during data collection!
   f) save the Excel worksheet under a new filename where ever you like
   g) repeat (b) - (e) for new runs
5. High Speed data collection
   a) connect the wave generator to the ext. trigger of the HP multimeter
   b) set the wave generator to a square wave of magnitude 2.5V and adjust to the desired sampling frequency
   c) open file "C:\HPVee Programs\FastDAQ"
   d) press start button on the left hand side of the window to collect data; the multimeter block is set to sample 7 channels at 40Hz for 500 data points per channel; you may have to adjust the aperture time if you choose another sampling frequency
   e) save the data record under a new name
   f) press the start button on the right hand side of the screen to extract the data; this program will build the 7 arrays and also do a lot of post processing
   g) return to "JulyDAQ" to monitor the system

Running Refrigeration Loop (refer to schematic)

1. Initial Startup
   a) make sure the following valves are OPEN: ball valves at inlet & outlet to test section, manual TXV (should still be set at last run condition)
   b) run DAQ software (see above instructions)
   c) plug water pump into power strip
   d) OPEN both water line ball valves on the wall
   e) OPEN flowmeter bypass ball valve located next to the flowmeter; this is necessary because the solenoid valve sticks at startup so we have to bypass it
   f) turn ON compressor
   g) CLOSE flowmeter bypass once system is stable
2. Operating Procedure
   a) adjust desired flowrate using manual TXV (clockwise increases flowrate)
   b) adjust water temperature using hot condenser water (gate valve very sensitive!)
   c) use heater to keep suction line from frosting
3. Shutdown
   a) turn OFF compressor
   b) CLOSE test section ball valves
   c) unplug water pump
   d) CLOSE water line ball valves on the wall

Appendix C: Summary of Runs 1-25 for Comparing Thermocouple and MEMS Sensor Signals

Run 1
DT_{sup} = 12.0°C; LMF = 0%

Run 2
DT_{sup} = 11.9°C; LMF = 0.28%

(a)

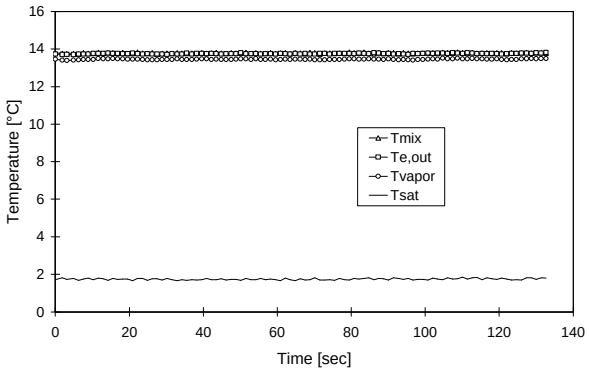

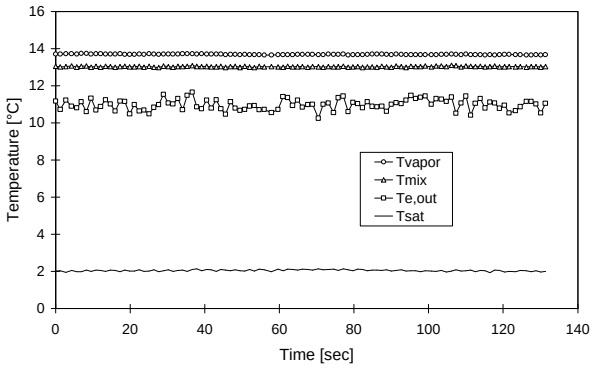

(b)

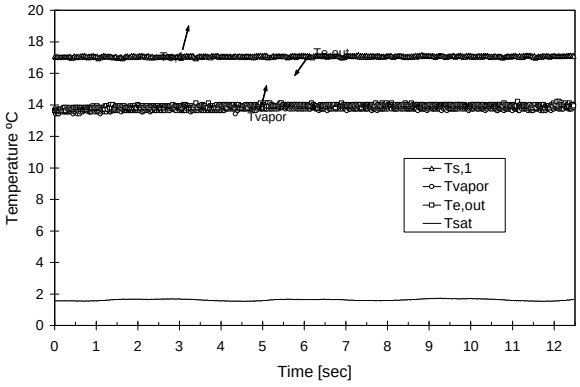

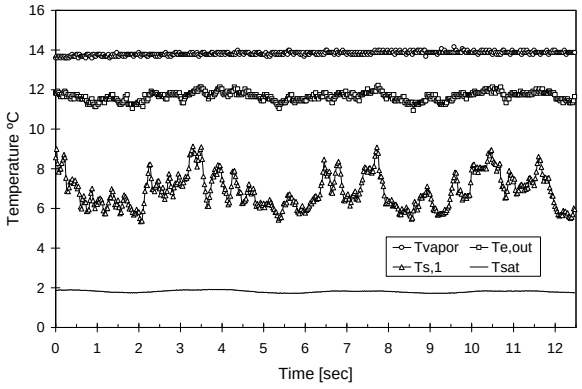

(c)

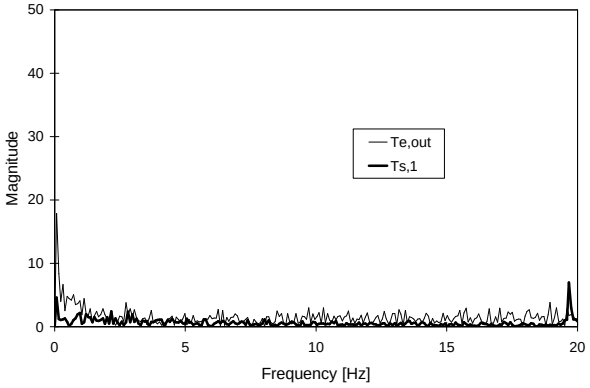

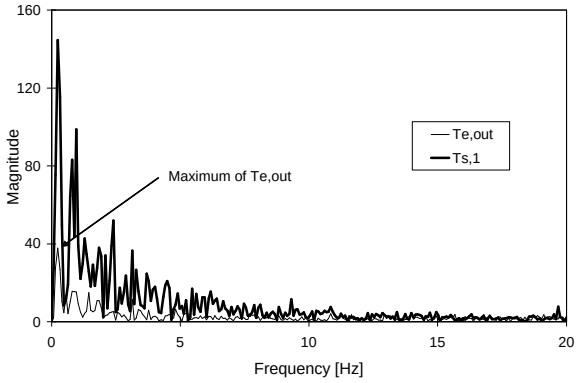

(a) Time trace of evaporator outlet and test section temperatures; **(b)** Thermocouple temperatures ($T_{e,out}$, T_{vapor}), MEMS sensor temperature ($T_{s,1}$), and saturation temperature (T_{sat}) at 40 Hz sampling rate; **(c)** Frequency spectra of $T_{s,1}$ and $T_{e,out}$ signals shown in **(b)**

Run 3
DT_{sup} = 12.1°C; LMF = 0.39%

Run 4
DT_{sup} = 12.0°C; LMF = 0.73%

(a)

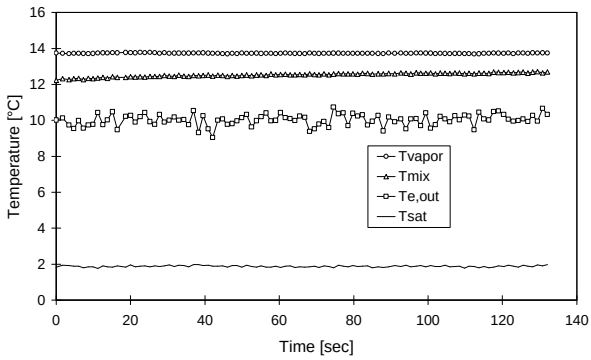

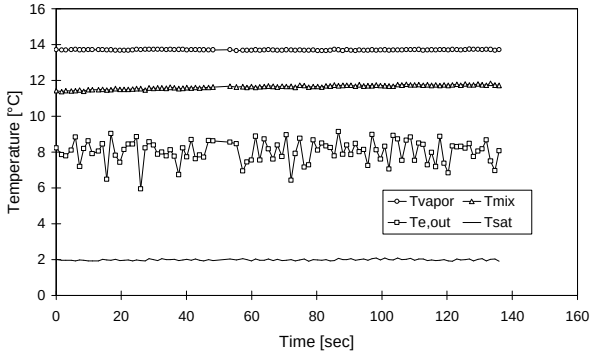

(b)

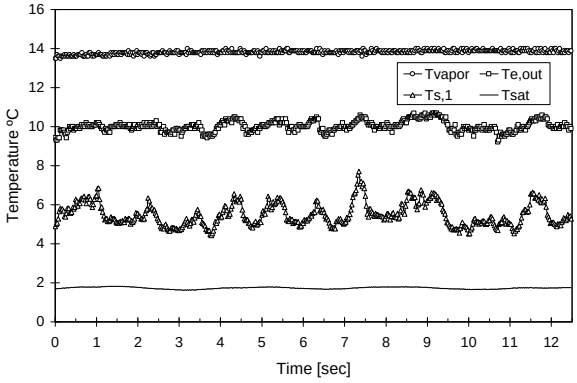

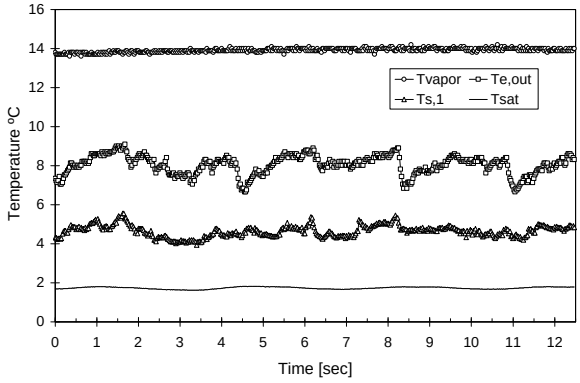

(c)

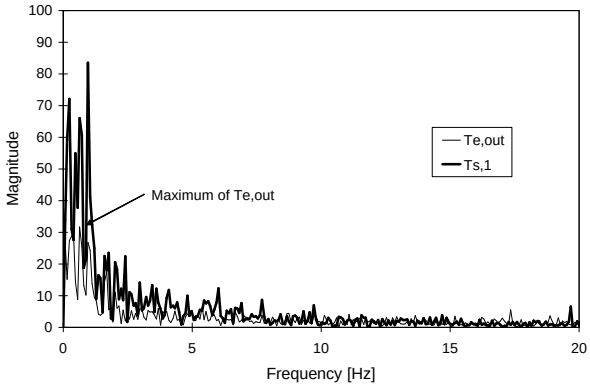

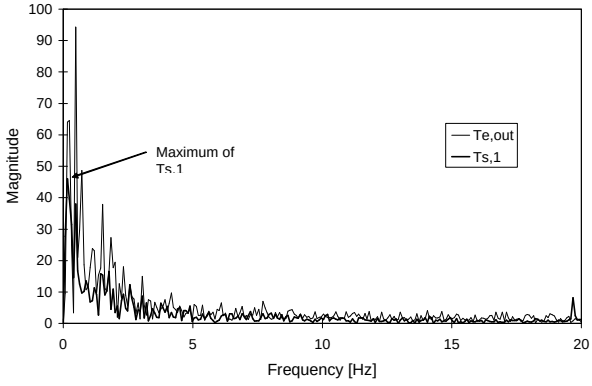

(a) Time trace of evaporator outlet and test section temperatures; **(b)** Thermocouple temperatures ($T_{e,out}$, T_{vapor}), MEMS sensor temperature ($T_{s,1}$), and saturation temperature (T_{sat}) at 40 Hz sampling rate; **(c)** Frequency spectra of $T_{s,1}$ and $T_{e,out}$ signals shown in **(b)**

Run 5
DT_{sup} = 12.0°C; LMF = 1.06%

Run 6
DT_{sup} = 11.9°C; LMF = 1.30%

(a)

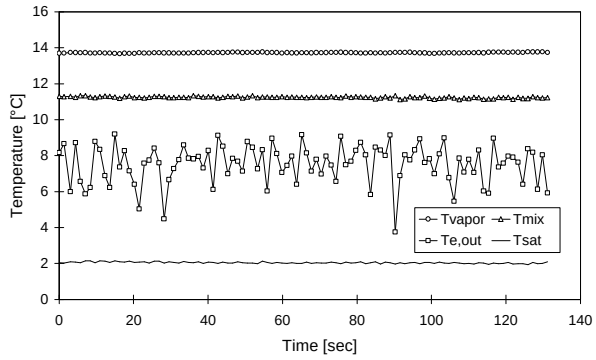

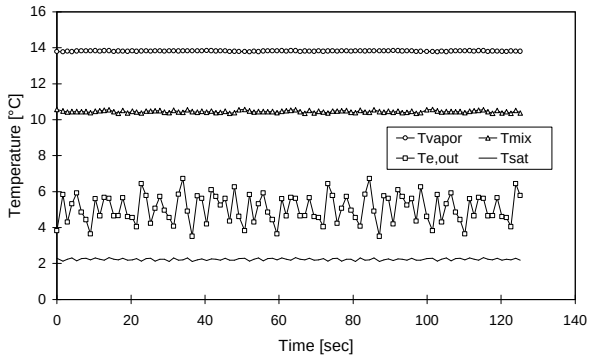

(b)

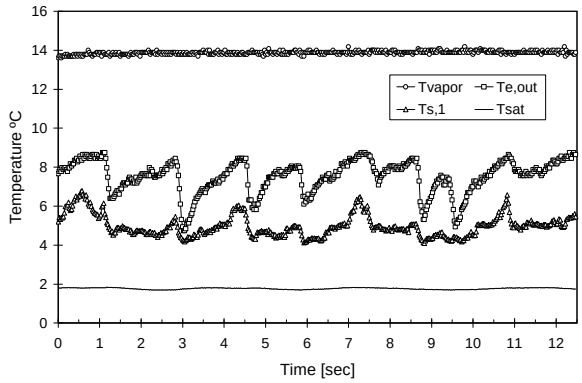

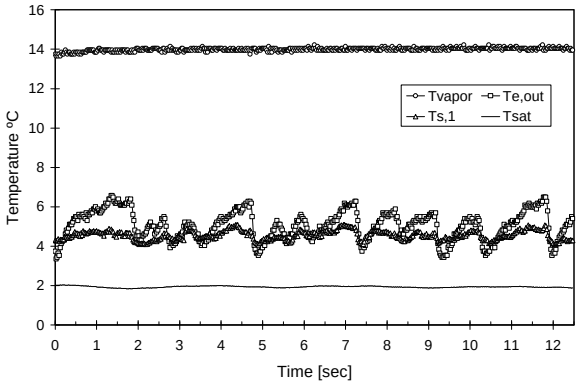

(c)

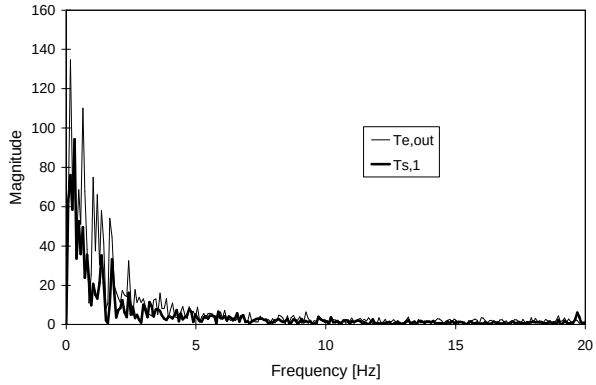

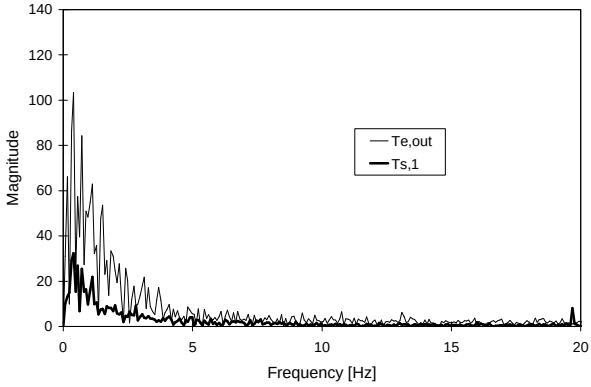

(a) Time trace of evaporator outlet and test section temperatures; **(b)** Thermocouple temperatures ($T_{e,out}$, T_{vapor}), MEMS sensor temperature ($T_{s,1}$), and saturation temperature (T_{sat}) at 40 Hz sampling rate; **(c)** Frequency spectra of $T_{s,1}$ and $T_{e,out}$ signals shown in **(b)**

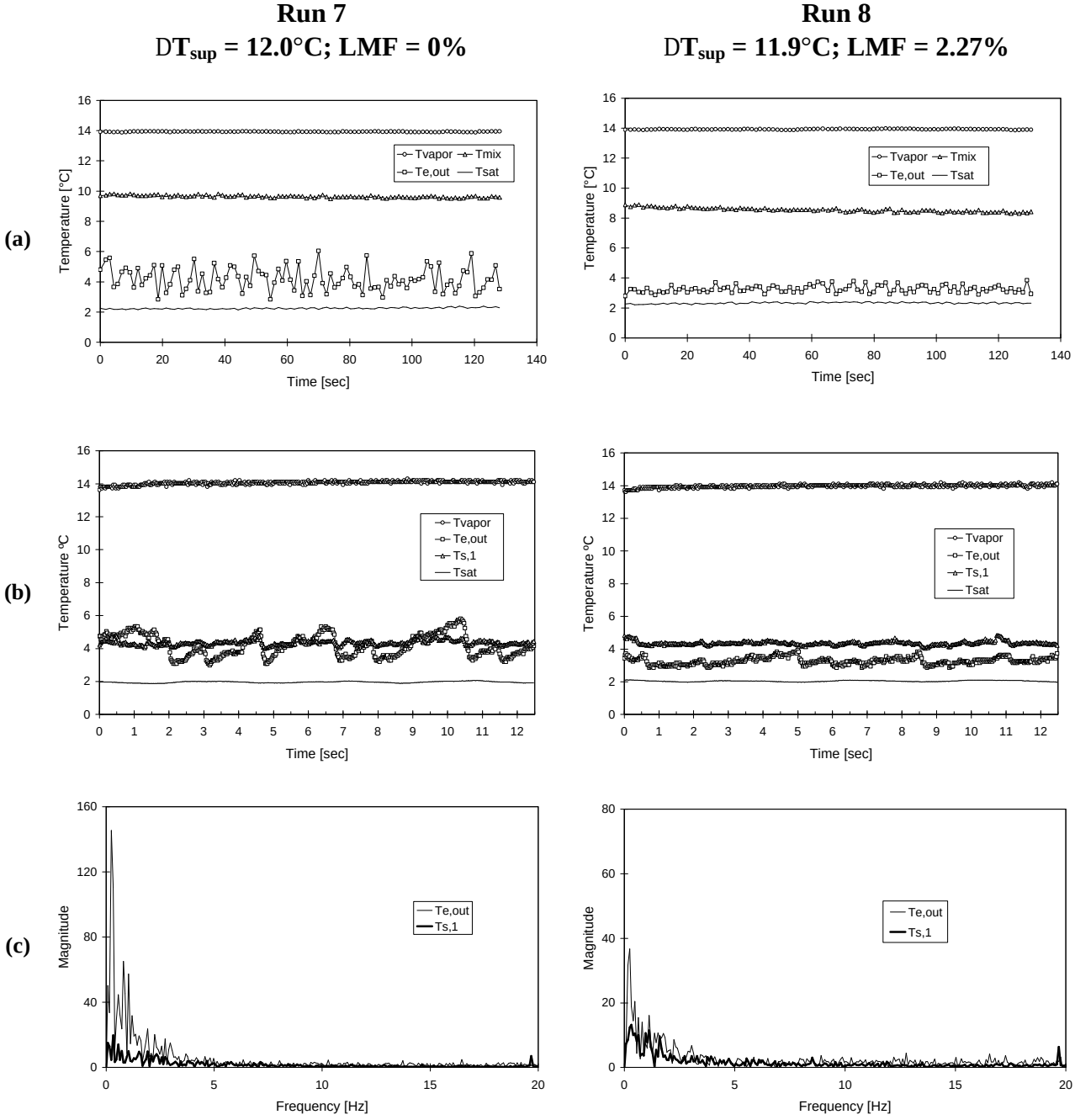

(a) Time trace of evaporator outlet and test section temperatures; **(b)** Thermocouple temperatures ($T_{e,out}$, T_{vapor}), MEMS sensor temperature ($T_{s,1}$), and saturation temperature (T_{sat}) at 40 Hz sampling rate; **(c)** Frequency spectra of $T_{s,1}$ and $T_{e,out}$ signals shown in **(b)**

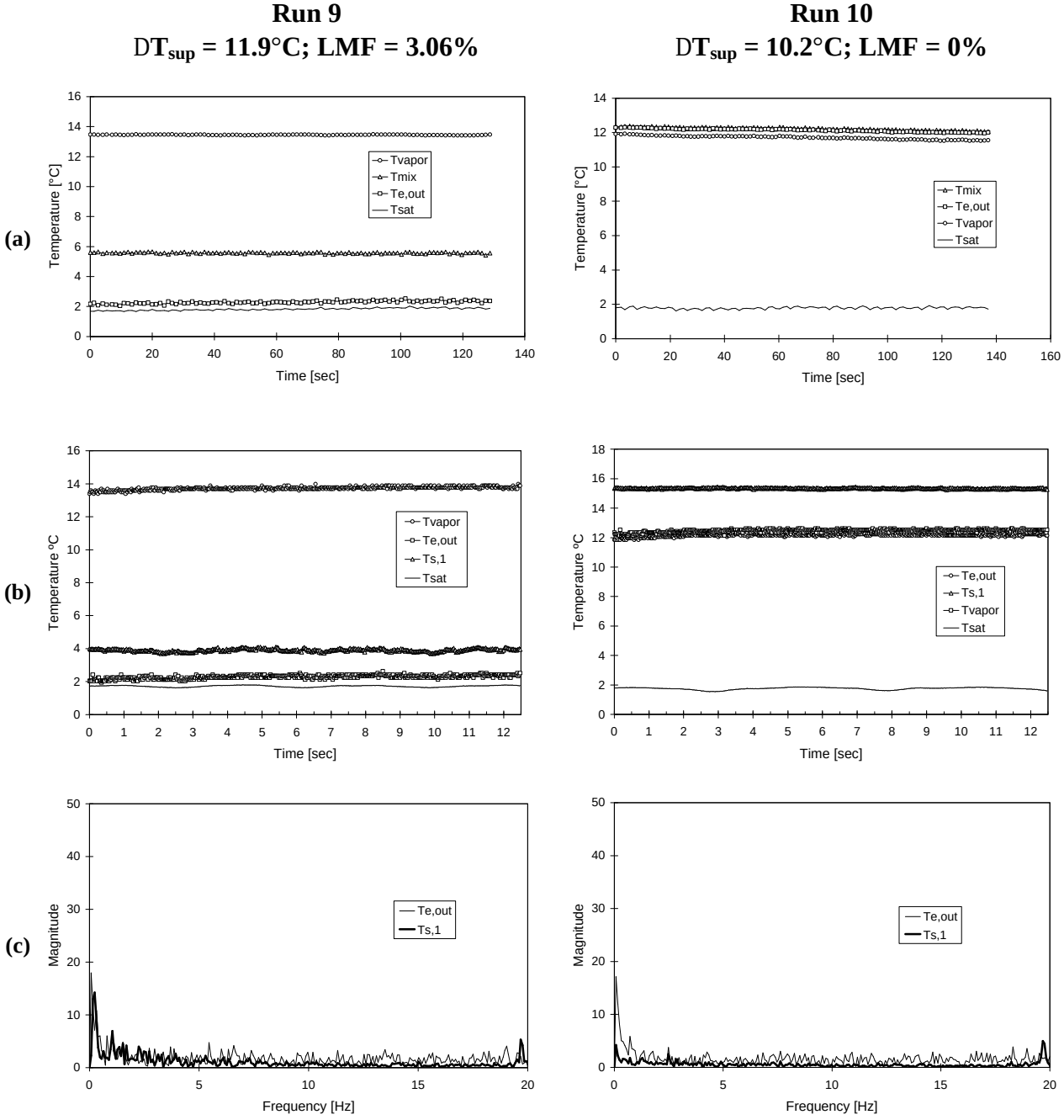

(a) Time trace of evaporator outlet and test section temperatures; **(b)** Thermocouple temperatures ($T_{e,out}$, T_{vapor}), MEMS sensor temperature ($T_{s,1}$), and saturation temperature (T_{sat}) at 40 Hz sampling rate; **(c)** Frequency spectra of $T_{s,1}$ and $T_{e,out}$ signals shown in **(b)**

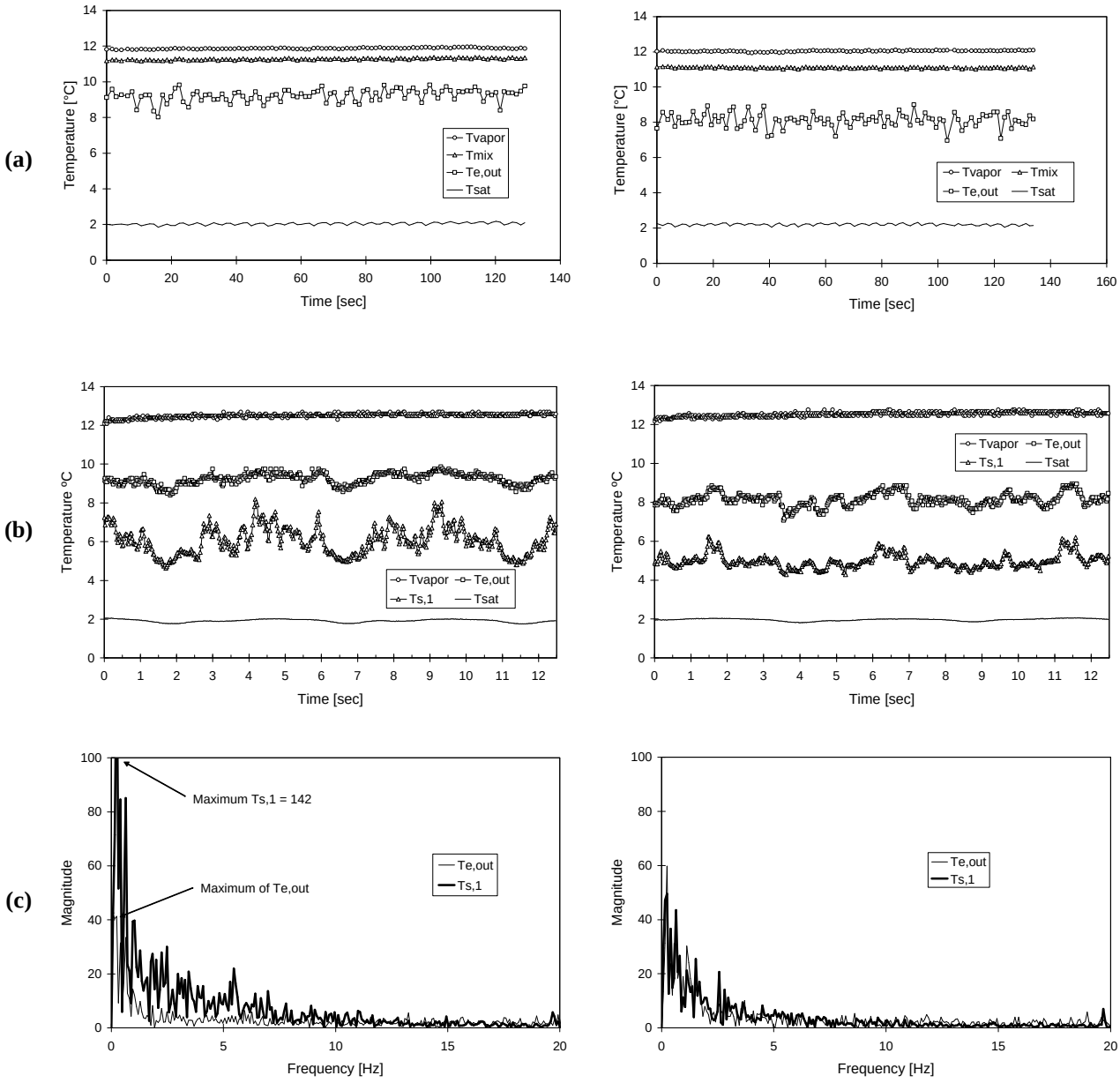

(a) Time trace of evaporator outlet and test section temperatures; **(b)** Thermocouple temperatures ($T_{e,out}$, T_{vapor}), MEMS sensor temperature ($T_{s,1}$), and saturation temperature (T_{sat}) at 40 Hz sampling rate; **(c)** Frequency spectra of $T_{s,1}$ and $T_{e,out}$ signals shown in **(b)**

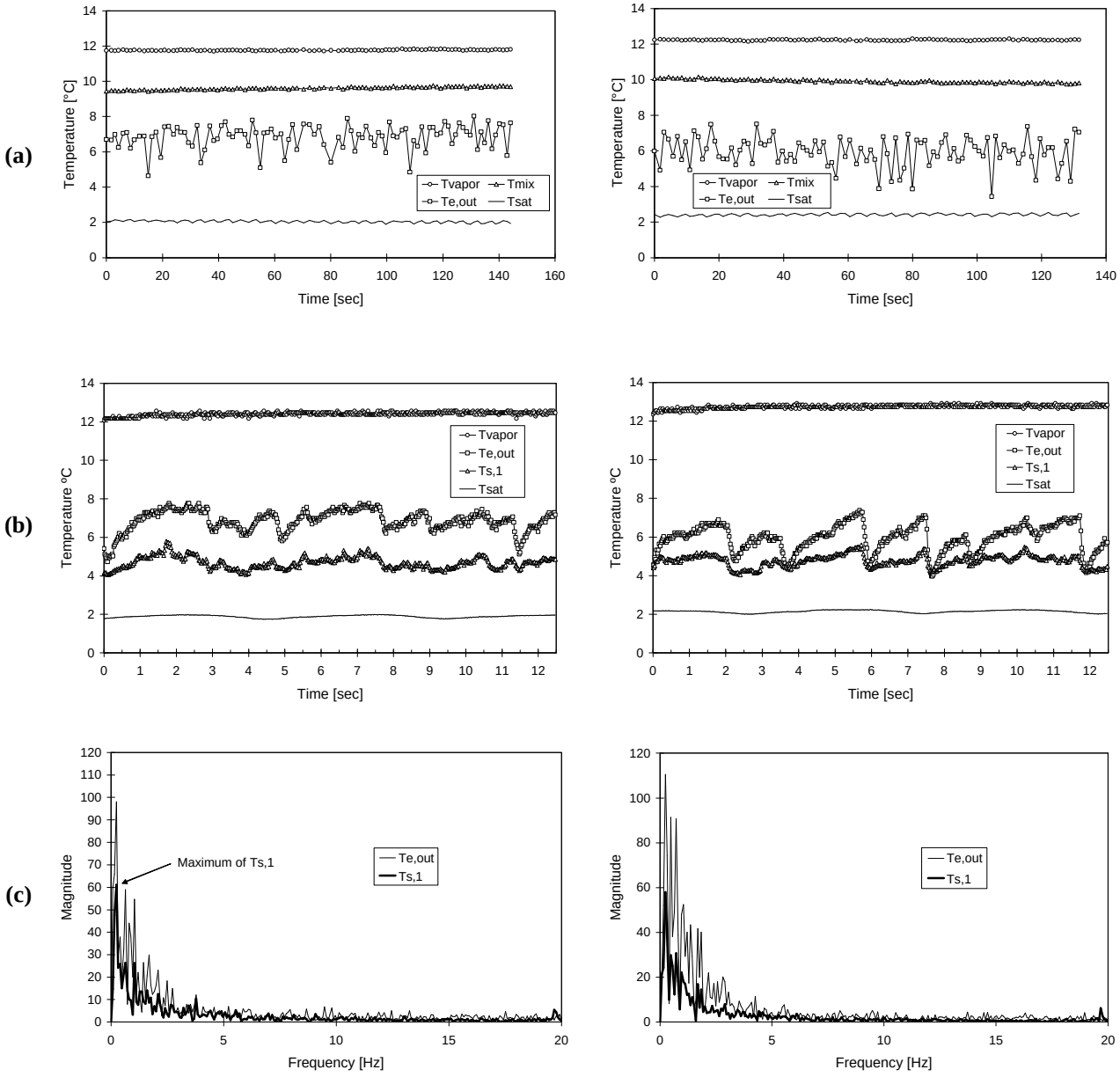

(a) Time trace of evaporator outlet and test section temperatures; **(b)** Thermocouple temperatures ($T_{e,out}$, T_{vapor}), MEMS sensor temperature ($T_{s,1}$), and saturation temperature (T_{sat}) at 40 Hz sampling rate; **(c)** Frequency spectra of $T_{s,1}$ and $T_{e,out}$ signals shown in **(b)**

Run 15
DT_{sup} = 10.2°C; LMF = 1.36%

Run 16
DT_{sup} = 10.2°C; LMF = 1.78%

(a)

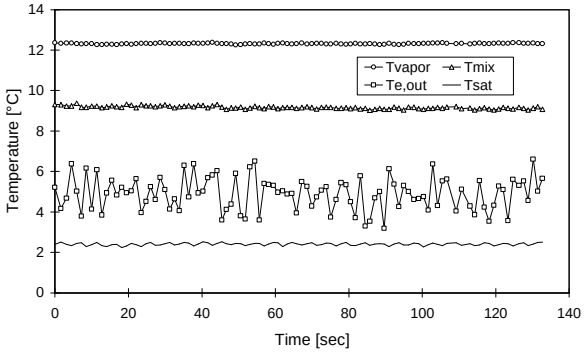

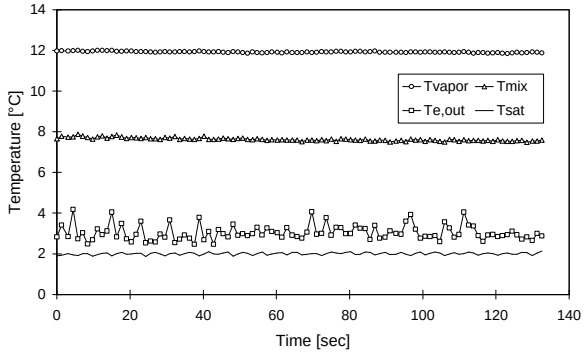

(b)

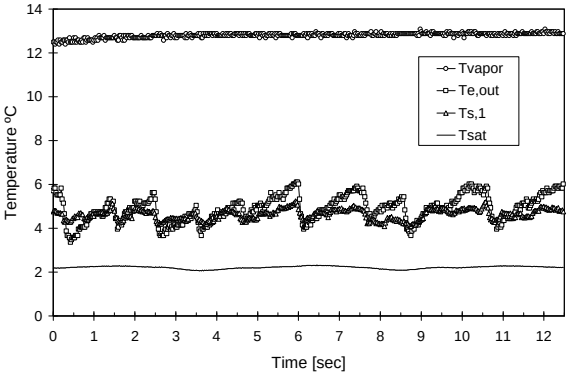

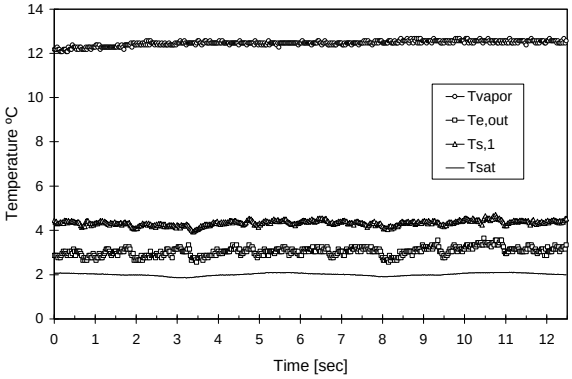

(c)

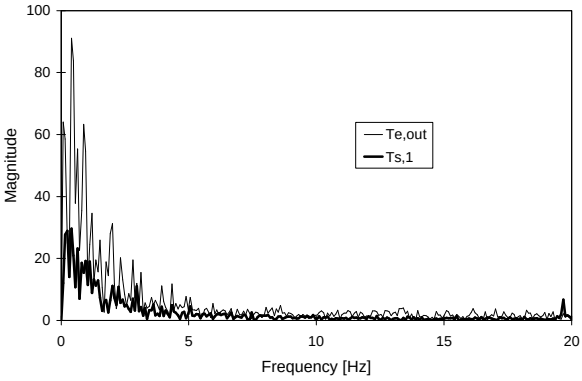

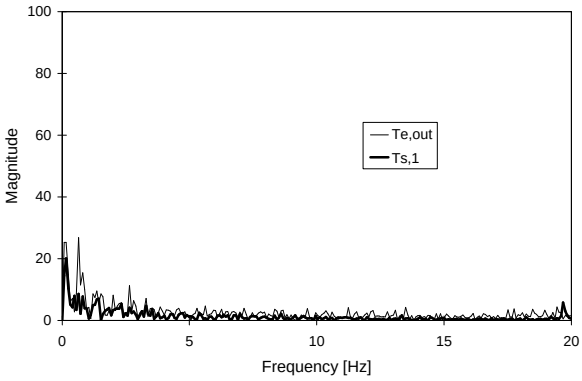

(a) Time trace of evaporator outlet and test section temperatures; **(b)** Thermocouple temperatures ($T_{e,out}$, T_{vapor}), MEMS sensor temperature ($T_{s,1}$), and saturation temperature (T_{sat}) at 40 Hz sampling rate; **(c)** Frequency spectra of $T_{s,1}$ and $T_{e,out}$ signals shown in **(b)**

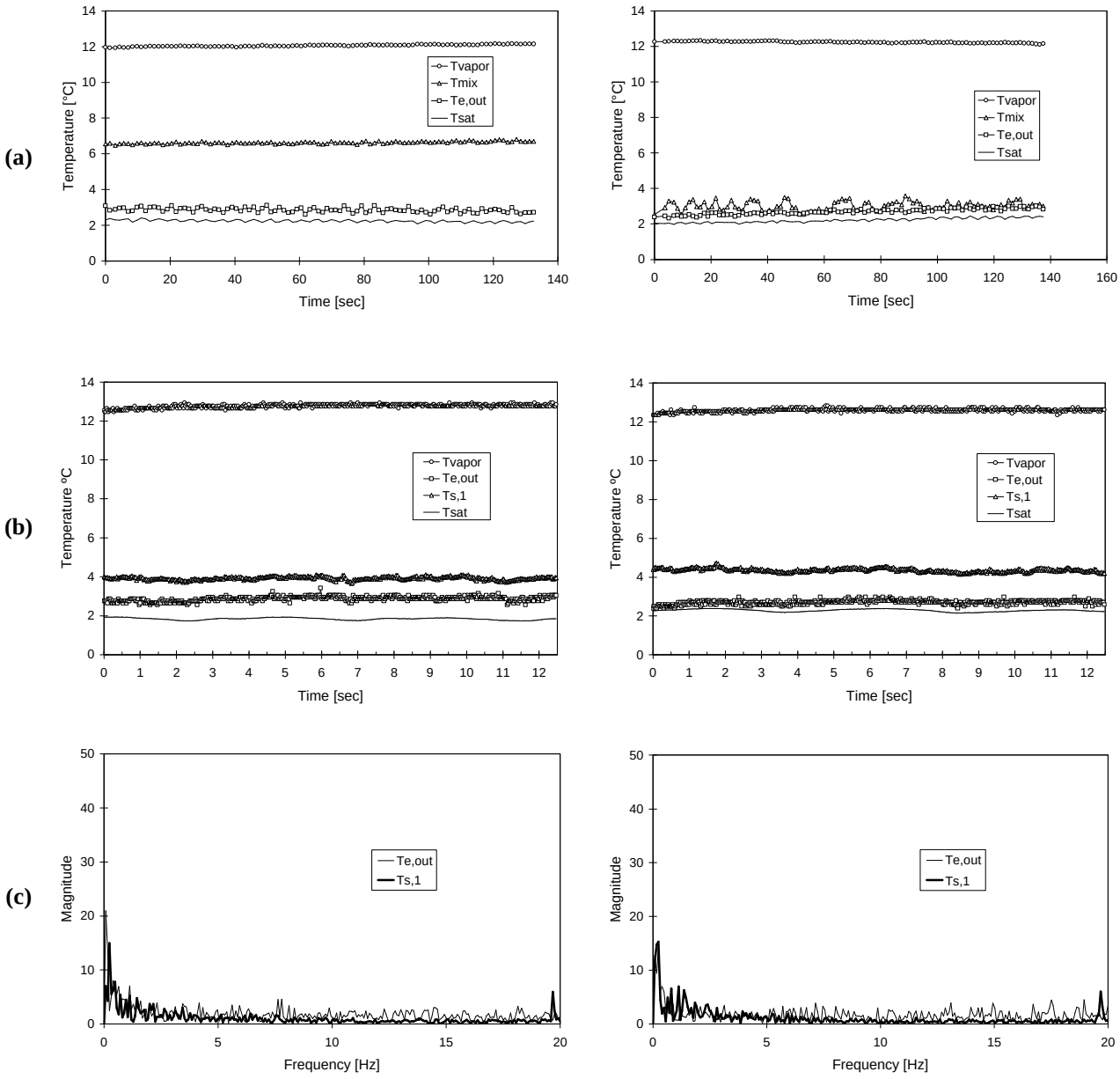

(a) Time trace of evaporator outlet and test section temperatures; **(b)** Thermocouple temperatures ($T_{e,out}$, T_{vapor}), MEMS sensor temperature ($T_{s,1}$), and saturation temperature (T_{sat}) at 40 Hz sampling rate; **(c)** Frequency spectra of $T_{s,1}$ and $T_{e,out}$ signals shown in **(b)**

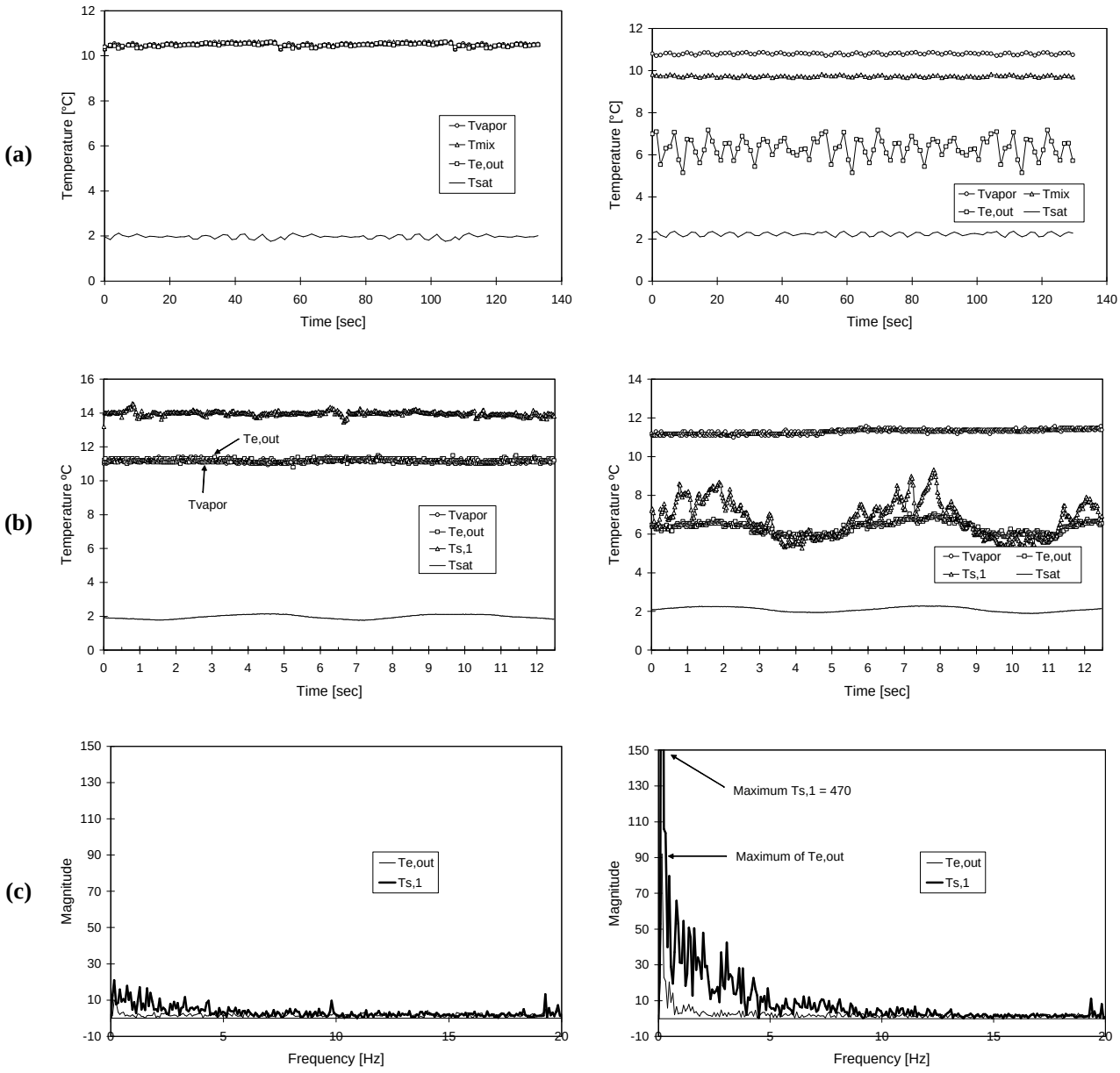

(a) Time trace of evaporator outlet and test section temperatures; **(b)** Thermocouple temperatures ($T_{e,out}$, T_{vapor}), MEMS sensor temperature ($T_{s,1}$), and saturation temperature (T_{sat}) at 40 Hz sampling rate; **(c)** Frequency spectra of $T_{s,1}$ and $T_{e,out}$ signals shown in **(b)**

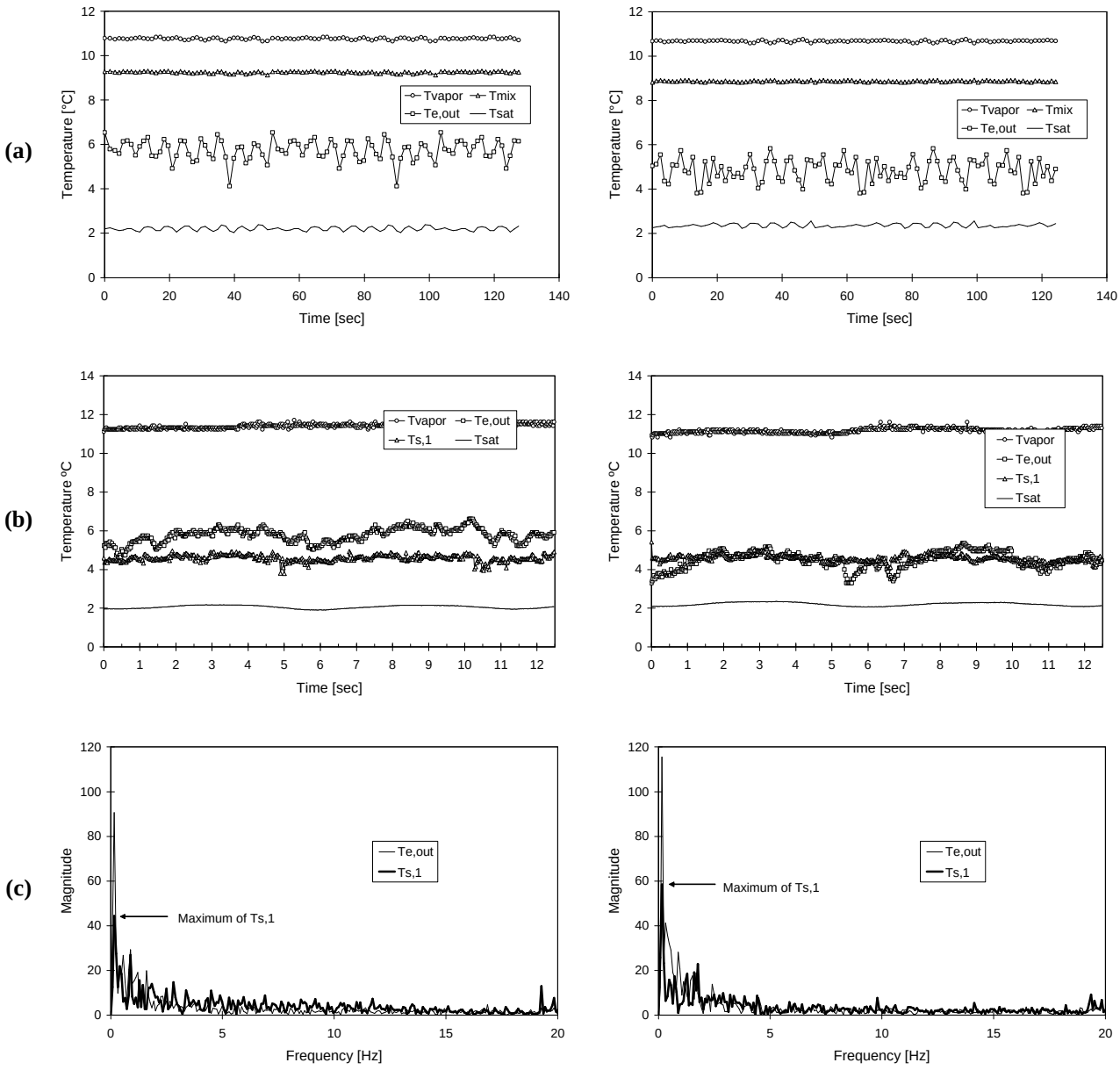

(a) Time trace of evaporator outlet and test section temperatures; **(b)** Thermocouple temperatures ($T_{e,out}$, T_{vapor}), MEMS sensor temperature ($T_{s,1}$), and saturation temperature (T_{sat}) at 40 Hz sampling rate; **(c)** Frequency spectra of $T_{s,1}$ and $T_{e,out}$ signals shown in **(b)**

Run 23
DT_{sup} = 8.2°C; LMF = 1.27%

Run 24
DT_{sup} = 8.4°C; LMF = 1.47%

(a)

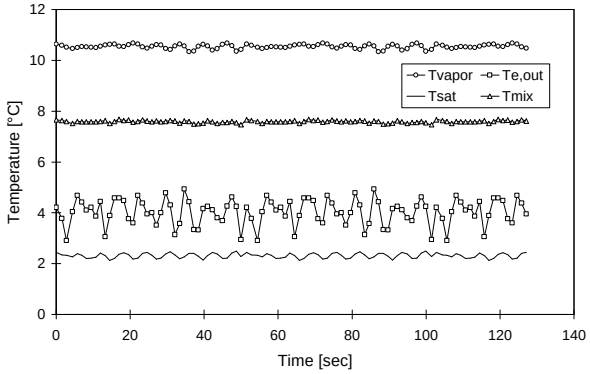

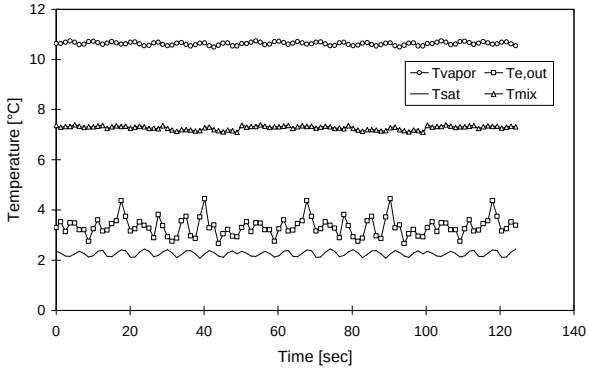

(b)

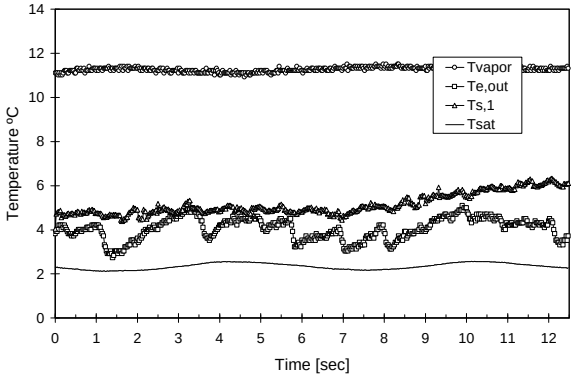

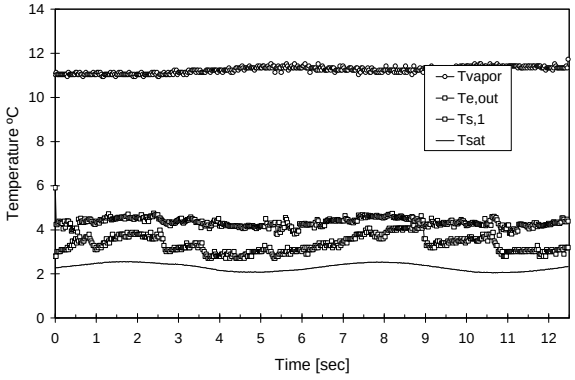

(c)

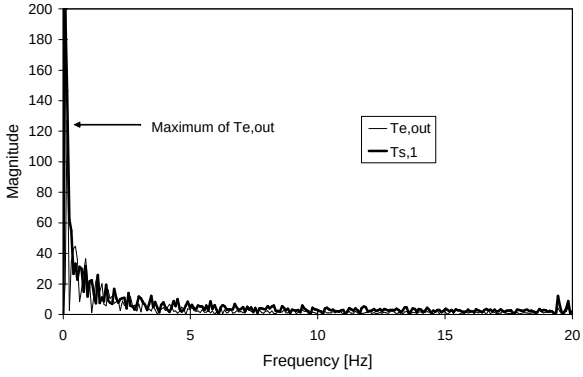

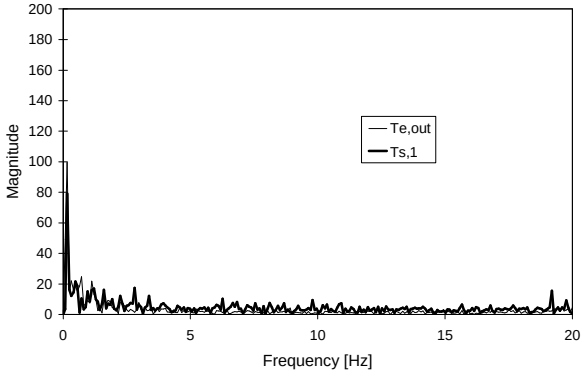

(a) Time trace of evaporator outlet and test section temperatures; **(b)** Thermocouple temperatures ($T_{e,out}$, T_{vapor}), MEMS sensor temperature ($T_{s,1}$), and saturation temperature (T_{sat}) at 40 Hz sampling rate; **(c)** Frequency spectra of $T_{s,1}$ and $T_{e,out}$ signals shown in **(b)**

Run 25
$D T_{sup}$ = 8.4°C; LMF = 2.03%

(a)

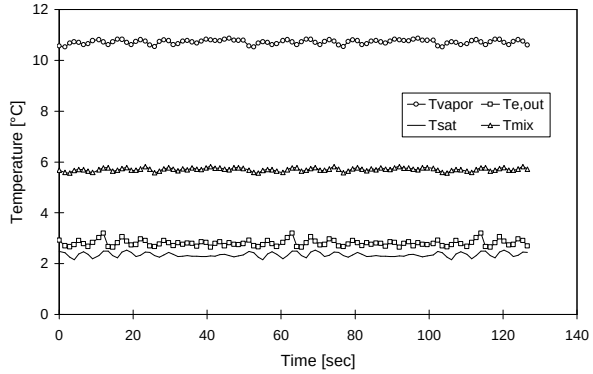

(b)

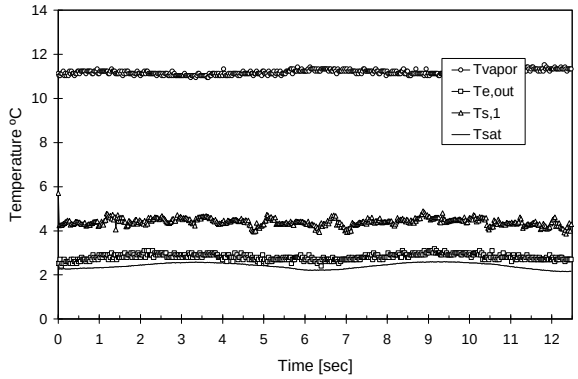

(c)

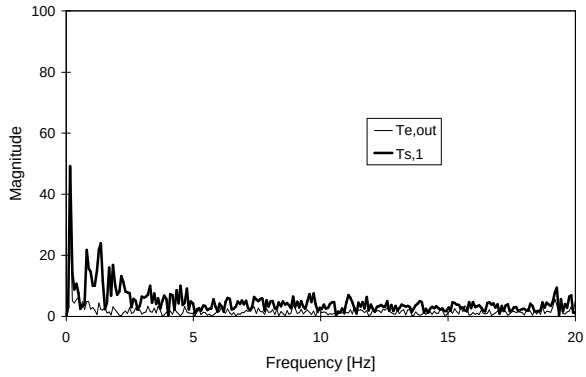

(a) Time trace of evaporator outlet and test section temperatures; **(b)** Thermocouple temperatures ($T_{e,out}$, T_{vapor}), MEMS sensor temperature ($T_{s,1}$), and saturation temperature (T_{sat}) at 40 Hz sampling rate; **(c)** Frequency spectra of $T_{s,1}$ and $T_{e,out}$ signals shown in **(b)**